Contents

Chapter 1

Background and Basic Physics

1.1 Present World Energy Consumption-*crisis*

There is a required and definite practical motivation behind nuclear fusion research, which is outlined in this section. Regardless of the scientific rewards associated with the realisation of an efficient fusion reactor, there are major social and economic benefits associated with terrestrial fusion. The worrying lack of alternatives to rapidly depleting fossil fuels as sources for global primary energy production are described, alternatives presented, and their advantages and disadvantages discussed.

1.1.1 Global trends

Today the majority of primary energy production depends on the burning of fossil fuels. Table1.1 shows an overview of the global energy production which highlights the over dependence on fossil fuels, 80% of the present global energy production.

The combustion of fossil fuels is generally accepted as being harmful to the environment, particularly as it involves the release of CO_2 which contributes to the greenhouse effect, i.e. increased absorption of the infrared radiation emitted from the earth. This excessive release of CO_2 has led to a 25% increase in the amount of atmosphere CO_2 in the last 200 hundred years, from levels which were constant during the previous 1,000 years [1]. The long term effects to our ecosystem are unknown, but one of the more immediate results is an increase in global sea levels, through the increase of the average

FUEL	CONTRIBUTION TO PRIMARY ENERGY PRODUCTION
Petroleum	39.3%
Coal	23.4%
Natural Gas	23.0%
Hydro	7.0%
Nuclear	6.5%
Others*	0.8%

∗ these include Geothermal, Solar, Wind, Wood and Waste electric power.

Table 1.1: *Global primary energy production by fuel in 2002. [3]*

global temperature which leads to a melting of the polar icecaps. For a more detailed discussion on the greenhouse effect and other detrimental results which stem from the use of fossil fuels, see review [2].

Fossil fuel reserves were built up over millions of years and are being consumed in the order of hundreds of years, thus they can be treated as finite resources which are rapidly running out. Oil accounts for almost 40% of the global energy production and more importantly almost 100% of transport needs. As the singularly most important primary energy source, oil reserves have been intensely studied. Over the past few decades the mean value for the estimated ultimately recoverable (EUR) oil (historical total) is about 2000 billion barrels (Bb) of oil [4] and 70% of the estimates fall between 2000 and 2400 Bb [5]. By the end of 2001, 940 Bb had been consumed; with the present rate of consumption at 27 Bb per year. If oil consumption remains constant and the most optimistic estimate of the EUR is assumed, there are only approximately 50 years of oil reserves left, which leaves little time to find a new primary energy resource.

It is also important to note that the rising global population is putting ever increasing strain on global energy resources. The population has risen from 2.5 to 6.1 billion in the past 50 years and is expected to grow to between 7.3 and 10.9 billion by the year 2050 [6]. The finite fossil fuel reserve, the population explosion coupled with the present standard of living to which mankind has become accustomed or is striving to achieve, makes it imperative to find a new primary source of energy.

1.1.2 Possible Solutions

Presently renewable energy sources and nuclear energy are the two main alternatives to fossil fuels; each with their own advantages and disadvantages.

Renewable energy sources such as solar, wind, geothermal, tidal, bio-mass and hydro-electric power stations are possibilities. Although indefinitely available, tapping into these energy resources is problematic. Many suffer from low energy densities and can be very susceptible to climatic fluctuations or geographical position. Photovoltaic panels are more likely to be efficient in countries towards the equator rather that in countries towards polar regions. However similar to wind power, they too are also very susceptible to transient weather patterns. Tidal and hydropower disrupt local ecosystems, while the intensive use of bio-power necessary to reach reasonable energy yields, leads to a serious loss of bio-diversity. These problems mean that renewable energy sources will tend to complement the primary energy sources rather than succeed then.

Another alternative to fossil fuels is nuclear energy. A nucleus consists of neutrons and protons, but the mass of any nucleus is always less than the sum of the individual nucleon masses. Using Einstein's mass equation

$$\Delta E = \Delta m c^2 \tag{1.1}$$

the difference in mass (Δm) is proportional to the binding energy of the nucleus (ΔE) where c is a constant (speed of light in a vacuum).

Fig.1.1 shows the variation of nucleon binding energy for different nuclei which indicates that the splitting of large nuclei or the joining of small nuclei will result in the release of energy.

Nuclear fission is the term given to the splitting of large nuclei by highly energetic neutrons into smaller nuclei. Although large amounts of energy are made available by this process, there are very serious dangers associated with fission power plants. During each exothermic fission reaction extra energetic neutrons are released (≈ 2.5 per reaction) which can lead to a a runaway fission process, 'chain reaction', Chernobyl is such an example.

Fission produces potentially dangerous by-products and large amounts of hazardous waste. One by-product is plutonium which is used in the construction of nuclear arms, which even if not used, has a long lifetime and the threat remains that it might be utilised

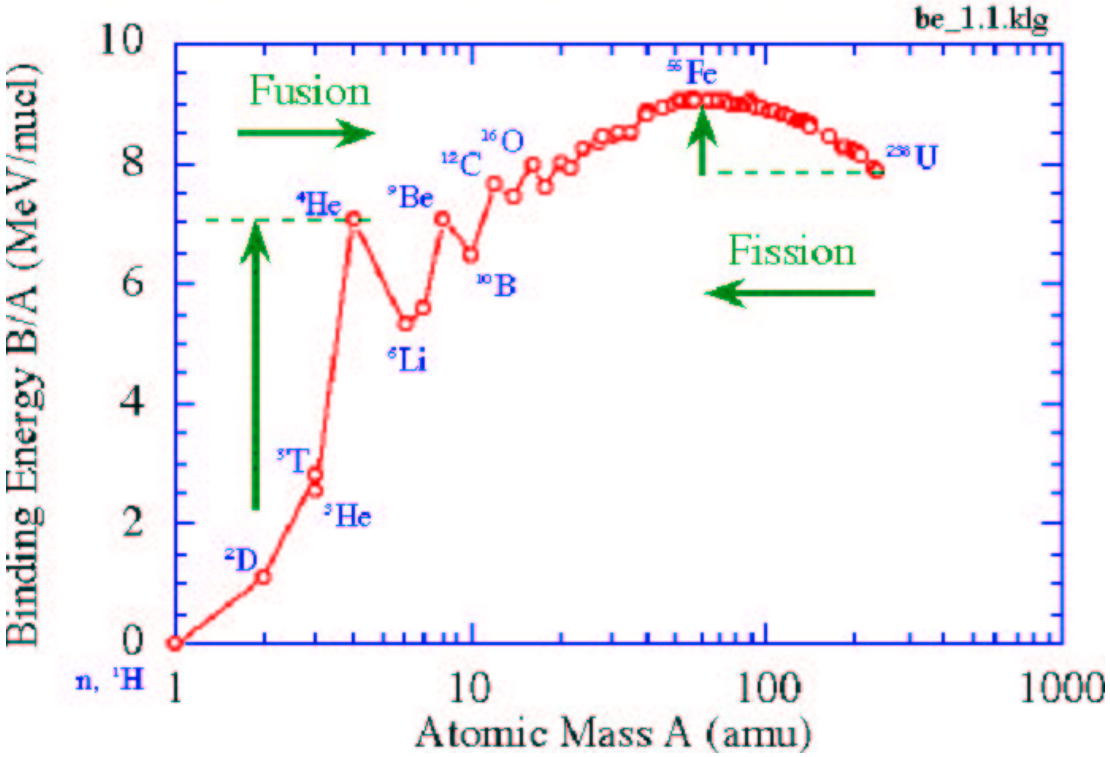

Figure 1.1: *Nucleon binding energy verses atomic mass number.*

in nuclear weapon proliferation in the future. Fission also produces large amount of waste which are also long lived, highly radioactive and difficult to dispose of and therefore will be an environmental worry for thousands of years.

At the moment nuclear fission reactors are the only energy source with a large enough energy density (1kg UO_2 equates to $6 * 10^5$ kg of Oil) to succeed fossil fuels as the world's primary energy source, but the inherent dangers to the environment make this a very unappealing solution to the future energy production problem.

Nuclear fusion is the reaction which combines two smaller nuclei into a larger nucleus. Today's fusion research program is centred on building a fusion reactor which will fuse two hydrogen isotopes (Deuterium and Tritium) into a Helium nucleus. Similar to nuclear fission, fusion reactions are highly exothermic, fusion of Deuterium and Tritium nuclei releases more than 10^6 times more energy than the combustion of an equivalent amount of oil. Unlike fossil fuels there is no foreseeable shortage in obtaining fusion fuels. Deuterium can be extracted from ordinary seawater with a yield of 33mg of Deuterium per litre. Only very small amounts of Tritium occurs naturally but it is easily bred by combining the neutrons produced from fusion reactions with lithium. Neither of the fusion products (Helium nucleus and a neutron) are radioactive therefore no primary radioactive waste is

produced. However there is a radiation problem with fusion products in that after some time, the surrounding vessel will become neutron activated. Research is being carried out to minimise this by utilisation materials with a high resistance to neutron activation such as Vanadium. Due to the the nature of the fusion process a 'chain reaction' is an impossibility and so accidents such as Chernobyl will never happen. For these reasons fusion reactors are the most appealing prospect for future primary energy production.

1.2 Nuclear Fusion: Basics

The following section gives an introduction to nuclear fusion, in particular magnetic confinement fusion and is based on [7] [8] [9] [10] [11].

1.2.1 Reactions

Nuclear fusion research favours the Deuterium-Tritium (D-T) reaction

$$ {}^{2}_{1}D + {}^{3}_{1}T \Longrightarrow {}^{4}_{2}He + n + 17.6MeV, \tag{1.2} $$

where the reactants combine to form an alpha particle and a neutron which carry 17.6 MeV of kinetic energy, 1keV $= 1.16 \times 10^7$ Kelvin.. As momentum is conserved the alpha particle carries away 3.5 MeV whilst the neutron carries 14.1 MeV.

Due to the large mutual coulomb repulsion between the positively charged ions, the fusion cross-section is very small at low energies. Fusion can actually take place at lower energy due to quantum tunnelling of ions in the high energy tail of the Maxwellian distribution of the ion velocities. Significant thermonuclear fusion begins to takes place at energies above 5 keV. These energies are much greater than the ionisation energy for hydrogen (13.6 eV) thus the hydrogen reactants are in the fully ionised plasma state.

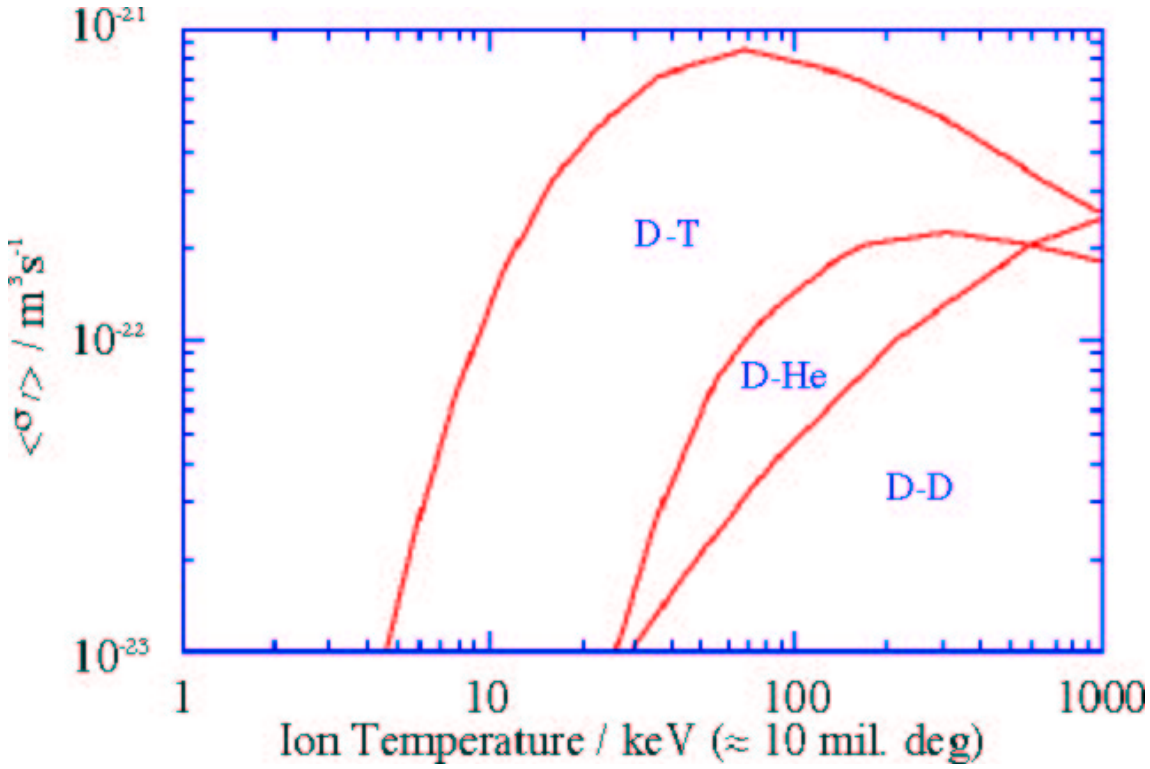

Figure 1.2: *Fusion cross-section for D-T, D-D, D-He reactions versus temperature (KeV).*

A reaction's reactivity $< \sigma v >$ is the product of the relative velocities of the nuclei and the reaction cross section averaged over the Maxwellian distribution for a fixed temperature. Fig. 1.2 shows the fusion reaction rates for D-T, D-D, D-He versus temperature (keV) and it follows that the D-T reaction is the most favourable fusion reaction for initial research. Tritium is radioactive and any D-T fusion reactor will carry an inherent risk. In the future, it might be more desirable to look at other reactions without any radioactive reactants, such as the $D - He^3$ reaction

$$ {}^{2}_{1}D + {}^{3}_{2}He^{3} \Longrightarrow {}^{4}_{2}He + {}^{1}_{1}H + 18.3MeV. \tag{1.3} $$

1.2.2 Power Balance

The following sub-section briefly describes power balance equations specific to fusion research and the criteria necessary for a D-T fusion reactor to reach ignition.

For a self sustained thermonuclear reactor it is necessary that the plasma reaches a state where the plasma power loss P_L is equal to the internal thermonuclear heating power P_{IH}.

Every D-T fusion reaction releases 17.6 MeV of energy. The 14.1 MeV neutron escapes but the 3.5 MeV alpha particle transfers its energy back to the plasma via coulomb interactions. For simplicity constant density n and energy (T) is assumed. The plasma power loss P_L is given by

$$P_L = \frac{3nTV}{\tau_e}, \tag{1.4}$$

where $3nT$ the total energy of the plasma, V is the plasma volume and τ_e is the energy confinement time.

Ignoring bremsstrahlung radiation loss as these losses are small when compared to the heating power of the alpha particles at reactor relevant temperatures. The alpha heating power P_{IH} is described by

$$P_{IH} = \frac{1}{4}n^2 < \sigma v > E_\alpha V, \tag{1.5}$$

where E_α is the energy imparted to each alpha particle The power balance in present day fusion experiments is given by

$$P_{EH} + \frac{1}{4}n^2 < \sigma v > E_\alpha V = \frac{3nTV}{\tau_e}. \tag{1.6}$$

External plasma heating P_{EH} makes up the difference between the internal alpha heating of the plasma and the total plasma power loss. Setting this quantity to zero gives us the criterion

$$n\tau_e > \frac{12T}{< \sigma v > E_\alpha}, \tag{1.7}$$

which has to be satisfied for a self sustained reaction. The right hand side is a function of temperature and gives a minimum value of 1.5×10^{20} at 30keV.

With τ_e being a function of T and the reactivity $\approx 1.1 \times 10^{-24} T^2 m^3 s{-}1$ between 10 and 20 keV, a more convenient ignition criterion is the fusion triple product

$$n\tau_e T > 3 \times 10^{21} m^{-3} keV s. \tag{1.8}$$

Although many experiments have reached the necessary density, energy confinement time or temperature necessary for ignition, none have satisfied all 3 criteria simultaneously.

The Q value for a fusion experiment is the ratio of total plasma power P_T to the external heating P_{EH} and is a measure of how effective is the experiment

$$Q = \frac{P_T}{P_{EH}} = \frac{5 \times P_{IH}}{P_{EH}}. \tag{1.9}$$

A Q value of 5 means that the internal alpha heating is equal to the external heating. This is due to Eqn. 1.2 where the escaping neutron holds 4 times more energy than the alpha particle. For ignition where no external heating is required, the Q value becomes infinite.

1.2.3 Fusion Research

Fusion reactions in present day experiments take place at very high temperatures where conventional containment methods, using materials walls, are inadequate. There are two main approaches to confining the fusion plasma long enough to reach thermonuclear ignition.

- Inertial confinement fusion (ICF), where the plasma is confined by it own inertia.
- Magnetic confinement fusion (MFE), where the plasma is confined by nested toroidal magnetic surfaces.

ICF lasers or high energy ion beams are used to heat D-T target pellets (≈1-3 millimetres in diameter). The pellet shell then ablates causing the frozen D-T fuel to compress (≈1000 times its fluid density). With this increase in both energy and density of the D-T fuel fusion takes place, albeit with a very short confinement time which can be measured in picoseconds [12].

ICF was first proposed during the 1960's and the first registered thermonuclear neutron from laser-produced plasma took place in Lebadev Physics Institute (USSR) in 1968. Today two major ICF experiments are being developed, namely the National Ignition Facility in Lawrence Livermore National Laboratory, USA and the Laser Mega-Joule in CEA, France. Each experiment will be able to deliver 1.8 MJ of 0.35 μm laser light with a peak power of 500TW to the fusion-able fuel. Both experiments under development hope to satisfy thermonuclear ignition conditions by the end of the decade.

The tokamak is the best known MFE device, was first designed in the early '50s by Sakharov and Tamm. The name tokamak is derived from the Russian *'toroidal'naya*

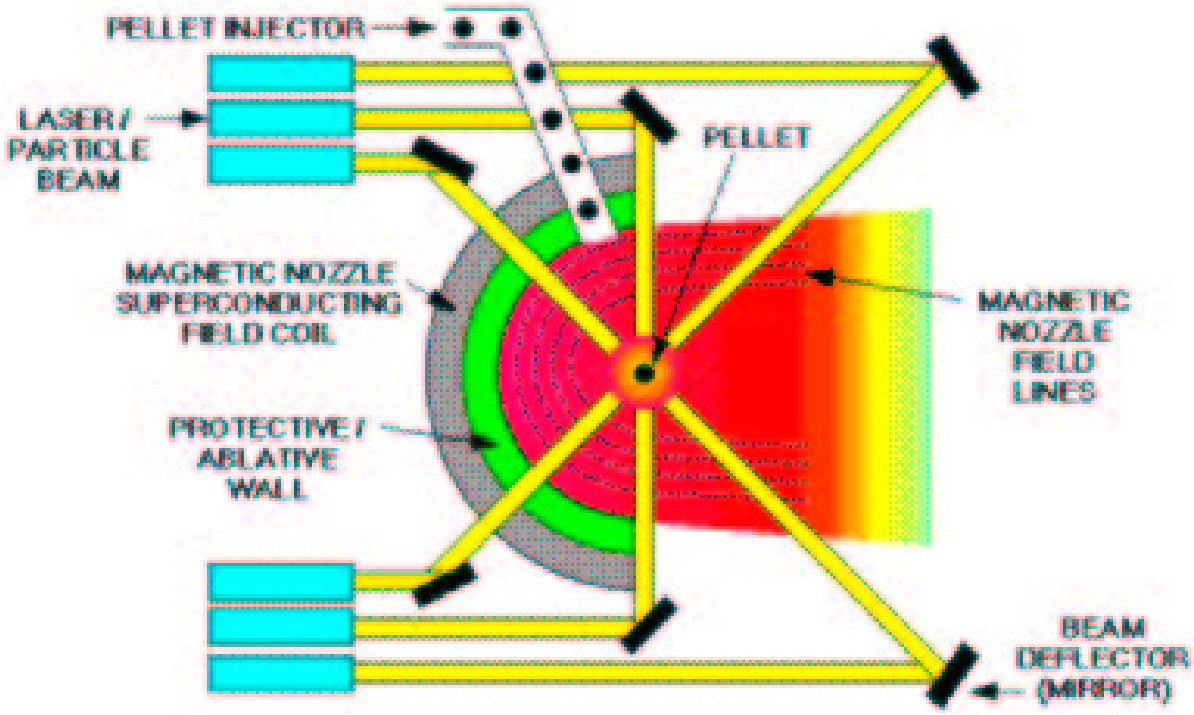

Figure 1.3: *Inertial confinement system schematic, National Ignition Facility, Lawerence Livermore National Laboratory.*

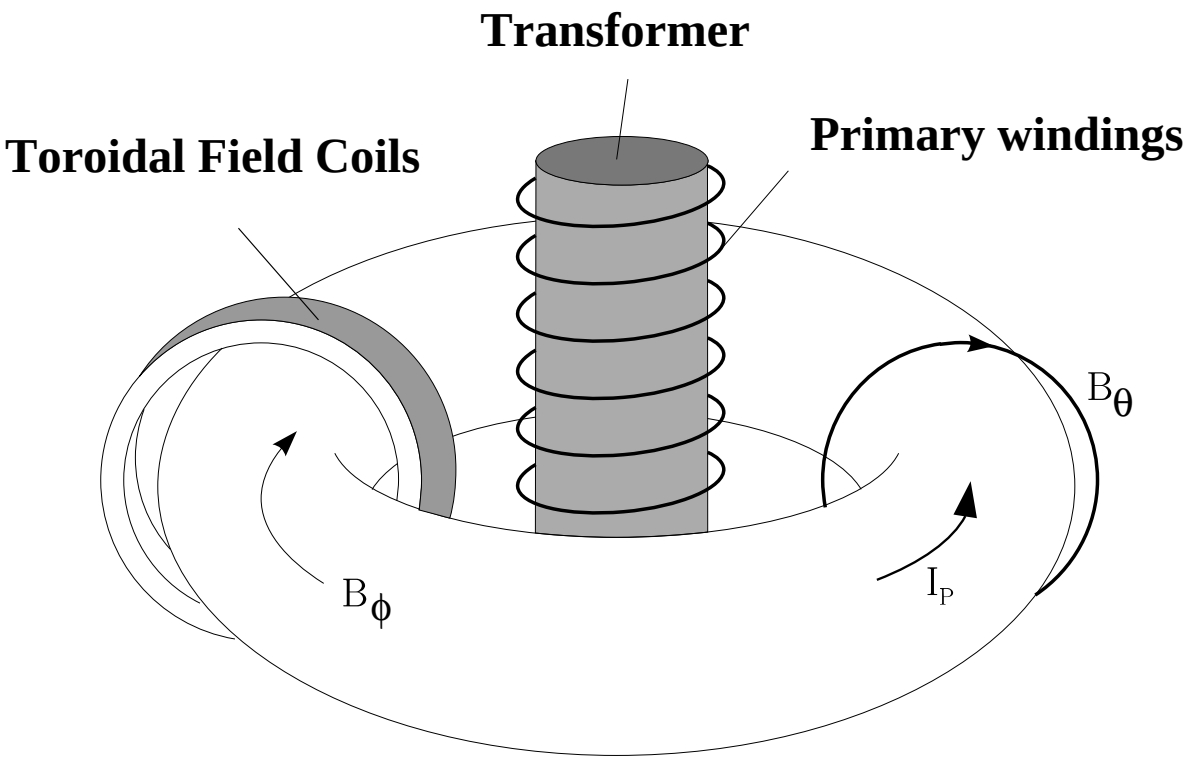

Figure 1.4: *Basic schematic of a tokamak device*

kamera i ee magnitnaya katushka', which translated means torus-shaped magnetic chamber. A tokamak is an axisymmetric device which confines the fusion plasma in a toroidal chamber by a combination of a poloidal $\mathbf{B}_\theta$ and toroidal $\mathbf{B}_\phi$ magnetic fields, see Fig. 1.4.

Current-carrying toroidal field coils surround the toroidal chamber which generates the dominant toroidal containment magnetic field. A toroidal plasma current I_p is setup by using the plasma as the secondary windings of a transformer action. The plasma current creates a poloidal magnetic field. Plasma particles then traverse the torus in helical paths.

Initially the plasma is heated resistively but as the plasma conductivity is proportional to the $T^{3/2}$. At higher temperatures ($> 1keV$) this heating method is ineffective and to reach higher temperatures additional heating methods are used. Ion cyclotron resonance heating (ICRH) and electron cyclotron resonance heating (ECRH) can be used, however the main heating method in today's and future tokamaks is neutral beam injection (NBI).

Present tokamak experiments show a net loss in energy. The next step in the global tokamak fusion initiative is to show a tokamak experiment with net energy gain. Today's research program is centred on the construction of the international thermonuclear fusion experiment - fusion energy advanced tokamak (ITER-FEAT) [13].

The ITER-FEAT experiment has two main aims. First is to operate in a quasi steady-state equilibrium with a Q-value >10 for transformer action induced I_p. A transformer induced I_p restricts tokamak operation to a pulsed regime and is not the most favourable reactor design. The second ITER-FEAT aim is to operate with a Q-value of >5 for a non-inductively driven I_p, to demonstrate the validity of a steady-state tokamak reactor.

Another MFE device is the stellarator. It is similar to the tokamak in that the plasma is confined by helical magnetic fields. With the non-axisymmetric stellarator coils geometry see Fig. 1.5, the helical containment magnetic field can be set up without the need of a plasma current. This gives the stellarator the ability to maintain steady state operation for long periods of time, unlike present day pulsed tokamaks. A major advantage of the stellarator is that it does not suffer from disruptions (instantaneous loss of I_P which results in containment loss in tokamak devices). The interaction between the fusion plasma and containment vessel is damaging to small tokamaks but could be disastrous for a large fusion reactor. The performance of present day stellarator experiments is poor when compared to present day tokamak experiments. Although stable stellarator experiments do not confine the plasma very well and the next generation experiments,

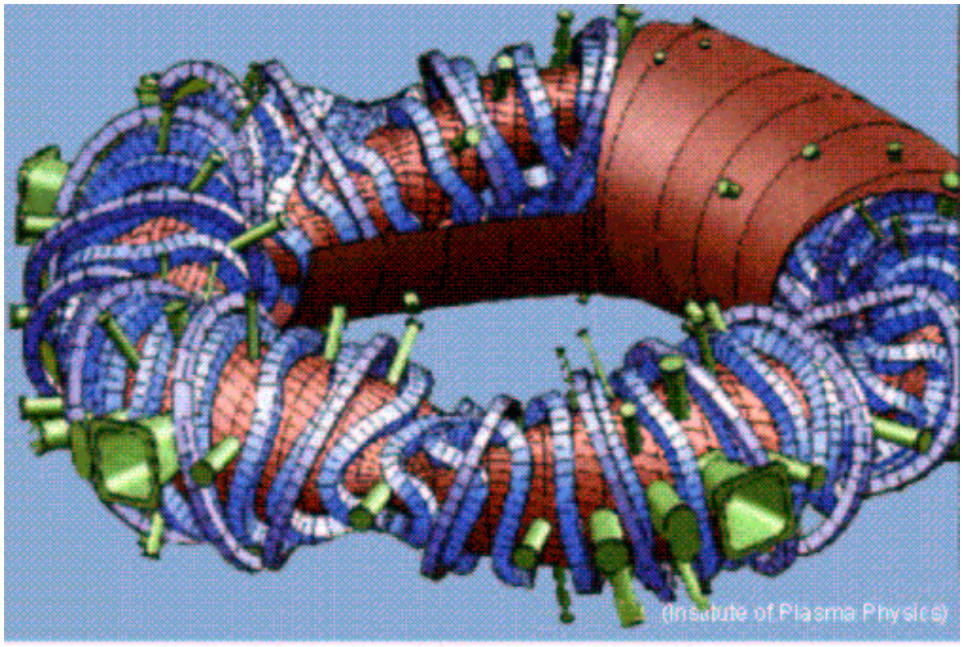

Figure 1.5: *Conceptual design of W7-X stellarator, IPP Greifswald, Germany*

W7-X, are being designed with enhanced plasma confinement in mind.

1.3 ASDEX Upgrade Tokamak

ASDEX Upgrade AUG, see Fig. 1.6 **A**xi**S**ymmetric **D**ivertor **EX**periment, is a middle sized tokamak which started operation in 1991 and is the successor to the ASDEX tokamak. AUG was designed to develop a reactor-compatible open divertor configuration with an elongated plasma. The main experimental interests are energy and particle exhaust physics, plasma control and disruption physics.

In AUG the plasma shape and position is controlled via ten vertical field coils and two passive saddle field coils [14], as shown in Fig.1.7. The toroidal field is usually kept constant during a given discharge, however a variation of up to 10% of the toroidal field during a discharge is possible. A real-time control system is used to maintain or adjust plasma parameters such as the the plasma position and shape. This system relies on experimental data, such as magnetic flux values, to recover these plasma parameters and can adjust the influence that the field coils have on the plasma to control the plasma parameters. A comparison of the poloidal cross sections of ASDEX Upgrade and the next generation tokamak ITER-FEAT is shown in Fig. 1.7, whilst some typical plasma parameters and technical specifications are given in Tables 1.2, 1.3.

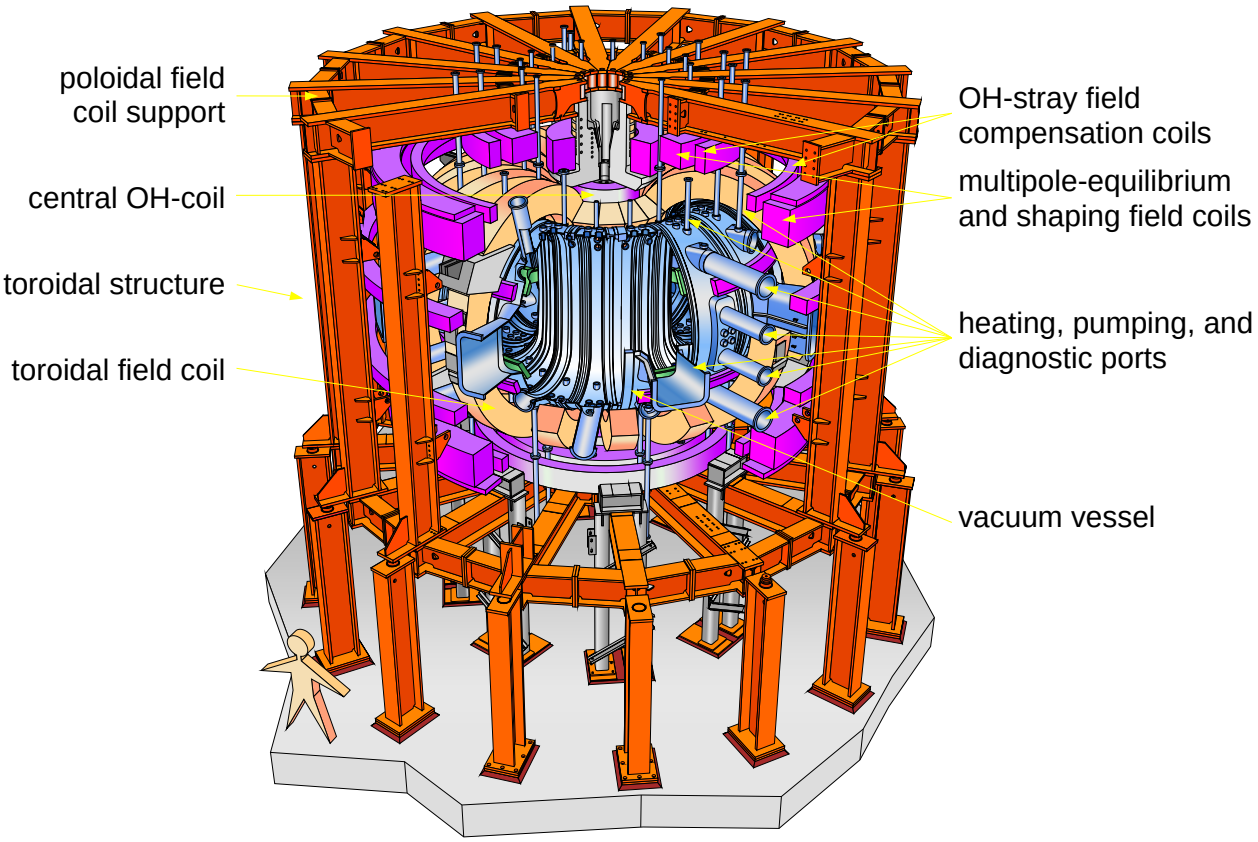

Figure 1.6: *The ASDEX Upgrade tokamak*

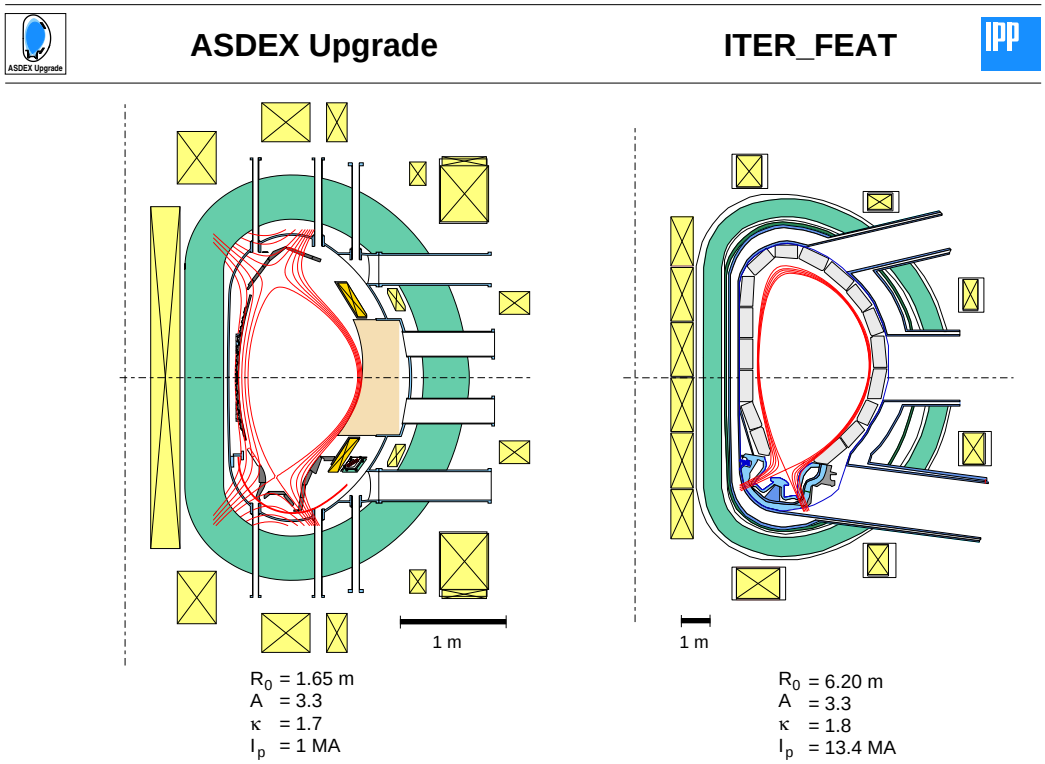

Figure 1.7: *Poloidal cross sections of the ASDEX Upgrade and ITER tokamaks.*

Parameter	**Value**
Major plasma radius	1.65 m
Minor horizontal plasma radius	0.5 m
Minor vertical plasma radius	0.8 m
Ellipticity	1.8
Triangularity (top/bottom)	0.1/0.3 since 1999 0.4/0.4
Plasma types	Deuterium, hydrogen, helium
Plasma volume	14 m^3
Plasma mass	3 mg
Electron density	1×1020 m^{-3}
Plasma temperature	60 - 100 $\times$ 10^6 degree

Table 1.2: *Typical ASDEX Upgrade plasma parameters*

Specification	**Value**
Total height of the experiment	9 m
Total radius overall	5 m
Weight of the experiments	800 t
Material of the first wall	carbon
Number of the toroidal field coils	16
Number of the poloidal field coils	10
Maximum magnetic field	3.1 T
Plasma current	0.4 MA-1.6 MA
Pulse duration	$<$ 10 s
Time between pulses	15-20 min
Amount of data / pulse	approx. 0.5 GByte
Plasma heating:	up to 27MW
Ohmical heating	1MW
Neutral beam heating	20Mw (with ^{2}H = D)
Injection energy	60keV and 100 keV
Ion-Cyclotron heating	6MW (30 MHz-120MHz)
Electron-Cyclotron heating	2 $\times$ 2 MW (120 GHz)

Table 1.3: *ASDEX Upgrade Technical Specifications*

1.3.1 Tokamak: Confinement, Equilibrium and q-Profile

Confinement The spatial evolution of a particle with charge e and mass m travelling in a magnetic field $\mathbf{B}$ is given by

$$m\frac{dv}{dt} = e(v \times \mathbf{B}) \tag{1.10}$$

For a uniform $\mathbf{B}$ charged particles travel at a constant velocity in a direction parallel to $\mathbf{B}$ and rotate in the plane perpendicular to the magnetic field. With a gyroradius r given by

$$r = \frac{mv_{\perp}}{eB}. \tag{1.11}$$

For typical reactor parameter values as follows, a toroidal magnetic field of 5 T and a plasma temperature of 10keV, the Deuteron gyroradius would be ≈3 mm, the electron gyroradius would be ≈0.05 mm while an alpha particle gyroradius would be ≈40 mm. Imagine a toroidal fusion device which consists of a toroidal magnetic field only, the magnetic field has a $1/R$ dependence where R is the major radius of the torus. Thus the charged plasma particles would have unequal gyroradii on the inner and outer half of each poloidal rotation. This would cause the electrons and ions to drift to the bottom and top of the torus and set up an electrostatic field E. The resulting $E \times B$ plasma drift would be catastrophic for plasma confinement. This is the reasoning behind the induced poloidal magnetic field associated with tokamaks.

Independent of how this poloidal field is setup, via an induced plasma current in tokamaks or non-axisymmetric poloidal coil geometry in stellorators, fusion plasma particles travel along magnetic field lines in helical paths around the torus. The degree of this helicity is very important to the stability of the plasma and is measured by the field line's q-value.

For a particular magnetic field line at a toroidal angle ϕ in a certain position in the poloidal plane, which will return to the same position after an angle $\Delta\phi$, the safety factor or q-value of this field line is defined to be

$$q = \frac{\Delta\phi}{2\pi} \tag{1.12}$$

This definition of the q-value is impractical, however the q-value will be discussed in

detail later in this chapter as the recovery of the toroidal q-profile is the main aim of this thesis.

Equilibrium For the purpose of this work the ideal magnetohydrodynamial (MHD) model will be used. The following subsection will outline the MHD model along with its advantages and disadvantages.

MHD is a combination of Euler's fluid equations and Maxwell's equations. It is a model used to describe the macroscopic properties of an electrically conducting fluid which is under the influence of a magnetic field, such as the terrestrial magnetic field and the magma in the earth's core or the influence of the solar magnetic field has on the generation of sunspots or flares. MHD is also the basic model used in tokamak equilibrium and stability studies.

Taking the plasma to be an ideal fluid with an adiabatic index of 5/3, the ideal MHD equations governing tokamak equilibrium are

$$\frac{\delta p}{\delta t} + \nabla \cdot (\rho \mathbf{v}) = 0 \tag{1.13}$$

$$\rho \frac{\delta \mathbf{v}}{\delta t} + \rho \mathbf{v} \cdot \nabla \mathbf{v} + \nabla p - \mathbf{J} \times \mathbf{B} = 0 \tag{1.14}$$

$$\frac{\delta p}{\delta t} + \mathbf{v} \cdot \nabla p + \frac{5}{3} p \nabla \cdot \mathbf{v} = 0 \tag{1.15}$$

$$\mathbf{E} + \mathbf{v} \times \mathbf{B} = 0 \tag{1.16}$$

$$\nabla \times \mathbf{B} - \mu_0 \mathbf{J} = 0 \tag{1.17}$$

$$\nabla \times \mathbf{E} + \frac{\delta \mathbf{B}}{\delta t} = 0 \tag{1.18}$$

$$\nabla \cdot \mathbf{B} = 0 \tag{1.19}$$

where ρ is the mass density, $\mathbf{v}$ the plasma velocity, $\mathbf{J}$ the current density, p is the plasma pressure, $\mathbf{E}$ the electric field and $\mathbf{B}$ the magnetic field. Eqns. 1.13 - 1.16 define

mass continuity, momentum balance, equation of state and Ohm's law, respectively with Ampere's law (Eqn. 1.17), Faraday's law (Eqn. 1.18) and (Eqn. 1.19) holds due to the absence of magnetic monopoles. The displacement current is assumed to be negligible, $v^2/c^2 << 1$.

For axisymmetric equilibria which are independent to the toroidal angle ϕ the magnetic field lines form nested toroidal surfaces. For a stationary incompressible plasma without flows $\delta/\delta t = \rho \mathbf{v} \cdot \nabla \mathbf{v} = 0$ to be in equilibrium the net force on the plasma must be zero hence Eqn. 1.14 becomes

$$\mathbf{J} \times \mathbf{B} = \nabla p. \tag{1.20}$$

It is obvious from this equation that

$$\mathbf{B}.\nabla p = 0, \tag{1.21}$$

$$j.\nabla p = 0. \tag{1.22}$$

This means that pressure is constant on a magnetic surface and the current lines lie along magnetic surfaces. It is now useful to introduce the poloidal magnetic flux function ψ_θ, which satisfies

$$\psi_\theta = \oint_{S_\theta} \mathbf{B}.dS, \tag{1.23}$$

here $\mathbf{B}$ is the total magnetic field and S_θ is a poloidal cross section of the magnetic surface. As ψ_θ is constant along magnetic surfaces

$$\mathbf{B}.\nabla \psi_\theta = 0. \tag{1.24}$$

Defining $\psi = \psi_\theta/2\pi$ to be the poloidal flux per radian in ϕ. From Eqn. 1.21 it follows that pressure is a poloidal flux function

$$p = p(\psi), \tag{1.25}$$

and symmetry demands a current poloidal flux function f where

$$f = f(\psi) \quad and \quad f = RB_\phi/\mu_0, \tag{1.26}$$

R is the major radius of the plasma.

Tokamak equilibrium calculations are based on the Grad-Shafranov equation

$$-\triangle^*\psi = \mu_0 r^2 p'(\psi) + f f'(\psi) \tag{1.27}$$

where $\triangle^*\psi = \left(\frac{\partial^2\psi}{\partial r^2} - \frac{1}{r}\frac{\partial\psi}{\partial r} + \frac{\partial^2\psi}{\partial z^2}\right)$. This is the principle MHD equilibrium equation for axisymmetric systems its derivation can be found in Appendix A and most MHD text-books. Solutions (ψ) of this second order partial differential equation yield the magnetic flux surface geometry for equilibria with specified pressure (p) and poloidal current (f) profiles.

Ideal MHD, while extremely useful, neglects many of the plasma properties such as heat conduction, resistivity, viscosity and particle diffusion.

Approximate analytical solutions of microscopic models are used to calculate the transport coefficients. Initially it was thought that plasma heat and particles would exit the plasma via 'collisional transport'. This process was assumed to have a very low loss rate due to the small gyroradii of the ions and the electrons combined with the low collision frequency of the plasma particle. Initial measurements put the diffusion rates between 10^3-10^4 the estimated value, which led to the term 'anomalous transport'. Attempts were made to explain this discrepancy by refining the initial model to include the effects due to the inherent inhomogeneous magnetic field, 'neoclassical transport', but this attempt is still out by an order of magnitude. All collisional transport studies ignore the microscopic chaotic 'turbulence' fluctuations in the magnetic or electric field which can cause increase in transport coefficients. To understand fusion plasma transport it is necessary to deal with the microscopic plasma particle motion. As it is analytically impossible to deal with each individual particle, models based on statistical distribution functions of each plasma species in phase space are used.

q-profile The definition of q is given in Eqn. 1.12 is impractical, a more useful form of q in terms of the $\mathbf{B}_\phi$ and $\mathbf{B}_\theta$ is

$$q = \frac{1}{2\pi}\oint \frac{B_\phi}{RB_\theta} ds. \tag{1.28}$$

Where the line integral is carried out over a single poloidal circuit. Also useful for large aspect-ratio tokamaks of circular cross-section is the approximation

$$q = \frac{rB_\phi}{RB_\theta}, \tag{1.29}$$

where r in the minor (poloidal) radius and R is the major (toroidal) radius. It is also important to state that q is a flux function.

$$q = q(\psi) \tag{1.30}$$

The q-value is also known as the safety factor due to its importance in determining the stability of the plasma. A basic example which can be used to illustrate this point is the 'Krushal-Shafranov' stability criteria which states that the q-value at the edge of the plasma (q_{edge}) must be greater than 1. However in reality q_{edge} tends to be ≥ 3 to avoid the occurrence of m/n 2/1 mode, and to a lesser extent 3/1 mode close to the edge of the plasma which is detrimental to plasma stability. Knowledge of the q-value is also central to the study of the sawtooth instability, where the q-value at the centre of the plasma (q_0) oscillates about a value of order 1. Research is always looking at the possibility of improving plasma confinement, specifically at advanced operating scenarios such as improved H-modes and internal transport barrier shots. These scenarios will be discussed in more detail in Chapter 4. Knowledge of the q-profile is essential for this work.

1.4 Motional Stark Effect Diagnostic

This section gives a brief introduction to the motional Stark effect (MSE) diagnostic [15], [16], centring on the theory behind the diagnostic and how this is applied to tokamak experiments, specifically the AUG experiment. For a more detailed description of various MSE diagnostics see [15] (PBX-M), [16] (PBX-M), [11] (JET), [17] (AUG).

1.4.1 Stark Effect

The Stark effect consists of the splitting and shifting of atomic energy levels under the influence of an external electric field, first observed by Stark in 1913 [18].

This interaction adds an extra term H' to the Hamiltonian

$$H' = -UD = eU \sum_i r_i, \tag{1.31}$$

where U is a external electric field directed along the z-axis, D is magnetic dipole moment.

The Schrödinger equation for the Stark effect is

$$(-\frac{\hbar}{2m_e}\nabla^2 - \frac{e^2}{(4\pi\epsilon_0)} + eUz)\psi = E\psi, \tag{1.32}$$

which can be solved using perturbation theory.

In this work we will only be dealing with the linear Stark effect, which is relevant for systems with degenerate eigenstates. States of equal energy which have the same principal quantum number n and different azimuthal quantum number l are defined to be degenerate, specifically hydrogenic atoms not in the ground state ($n \geq 2$). In the general case of multi-electron atoms where eigenstates are non-degenerate the first order approximation of the Stark effect is zero and does not lead to any change of energy of the atom. Multi-electron atoms are influenced by the weaker quadratic Stark effect, which is irrelevant to this work.

The eigenvalue solution of Eqn. 1.32 in parabolic co-ordinates is

$$E = E_n + \frac{3}{2}eUa_0n(k_1 - k_2). \tag{1.33}$$

The relationship between the parabolic quantum numbers k_1 and k_2 and n, m is

$$n = k_1 + k_2 + |m| + 1; k_1, k_2 = 0, 1, 2... \tag{1.34}$$

Of particular interest to the MSE diagnostic is the Balmer D_α transition ($n = 3 \rightarrow 2$) where the Stark energy splitting is

$$\Delta E = \frac{3}{2}eUa_0. \tag{1.35}$$

With the $n = 3$ line Stark split into 5 components and the $n = 2$ line Stark split into 3 components the D_α line splits into 15 components (8 π-components and 7 σ-components). The strong D_α transitions are given in Fig. 1.8, the $\pm 5\sigma$, $\pm 6\sigma$, $\pm\pi$ lines are omitted as these lines are of such small intensity as to be of no practical value.

Finally it is should be noted that in present day tokamaks the Zeeman effect on hydrogenic line emission is negligible when compared to the linear Stark effect. This was shown by [19] and [11].

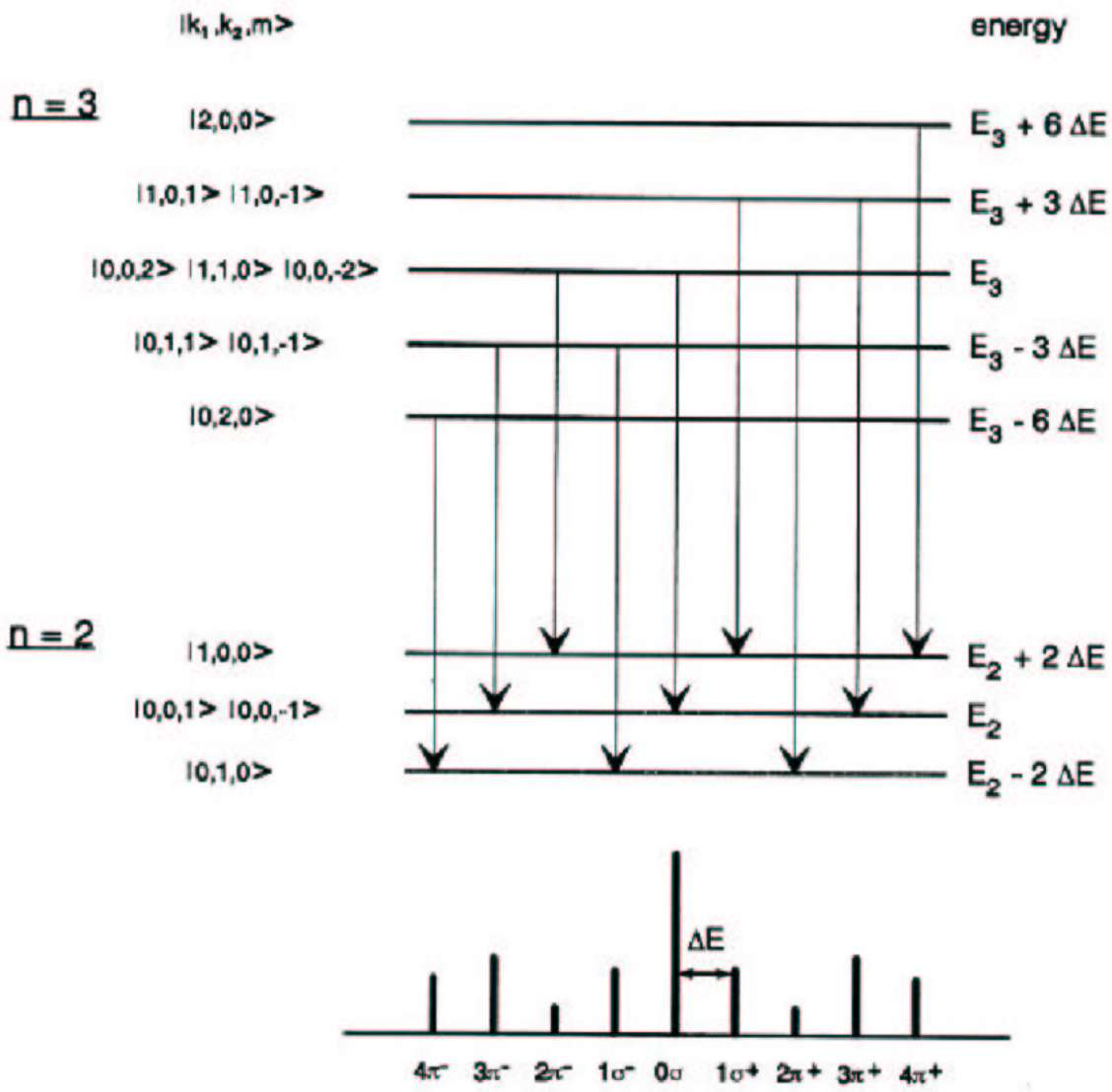

Figure 1.8: *Energy diagram for D_α transition in a strong electric field. The energy splitting along with the related eigenstates are indicated. A schematic spectrum is also given which demonstrates the symmetry and indicates the polarisation(σ, π) of the transition lines.*

1.4.2 MSE Diagnostic and Experimental Setup on AUG

High energy (70-140 keV) neutral hydrogen or Deuterium beams are used to heat the tokamak plasma because they are neutral and as a result the beams can traverse the tokamak's magnetic field and reach the plasma core. These beams experience a large Lorentz electric field ($E_L = V_{beam} \times B$) which leads to significant Stark splitting of the emission lines. This effect is referred to as the motional Stark effect. As the D beam experiences the electric field in its rest frame the motional Stark effect is equivalent to the linear Stark effect and if the lines are viewed at an angle other than 90° they are doppler shifted. The polarisation pattern of the Stark spectrum is a direct measure of the magnetic field direction. From this information the internal magnetic field can be determined from which current density related parameters can be recovered. The advantage of the MSE diagnostic is that it is possible to recover an accurate local measurement of the magnetic pitch angle γ.

$$tan(\gamma) = \frac{B_\theta}{B_\phi}, \tag{1.36}$$

where B_θ, B_ϕ are magnitudes of the poloidal and toroidal magnetic fields respectively.

Alternative methods such as Faraday rotation polarimetry suffer from poor local resolution, due to the necessity for numerical inversion of the line integrated measurements to recover spatial information.

The AUG neutral beam heating system consists of two injectors, each injector contains 4 positive ion neutral injectors (PINI) resulting in 4 different beams. The first injector, SE-injector, is situated in sector 15 of the experiment while the second beam, NW-injector, is situated in sector 7. The NBI beams can consist either of H^0 or D^0 and the maximum total power injected into the plasma is 14 MW if H^0 is used or 20 MW for D^0.

The 10 channel AUG MSE diagnostic observes one of the four highly collimated 2.5 MW, 60 keV 'SE- injector' beams. The MSE diagnostic[1] setup is shown in Fig. 1.9.

The emitted light is focused through a set of lenses via a dielectric mirror onto 2 photoelastic modulators (PEMs) through a sheet polarizor to a fibre optic array. The additional polarisation of the light due to the optical properties of the mirror is taken into

[1] The new data acquisition system indicated was not used during this work as this system was unavailable and has only recently entered an extended testing phase.

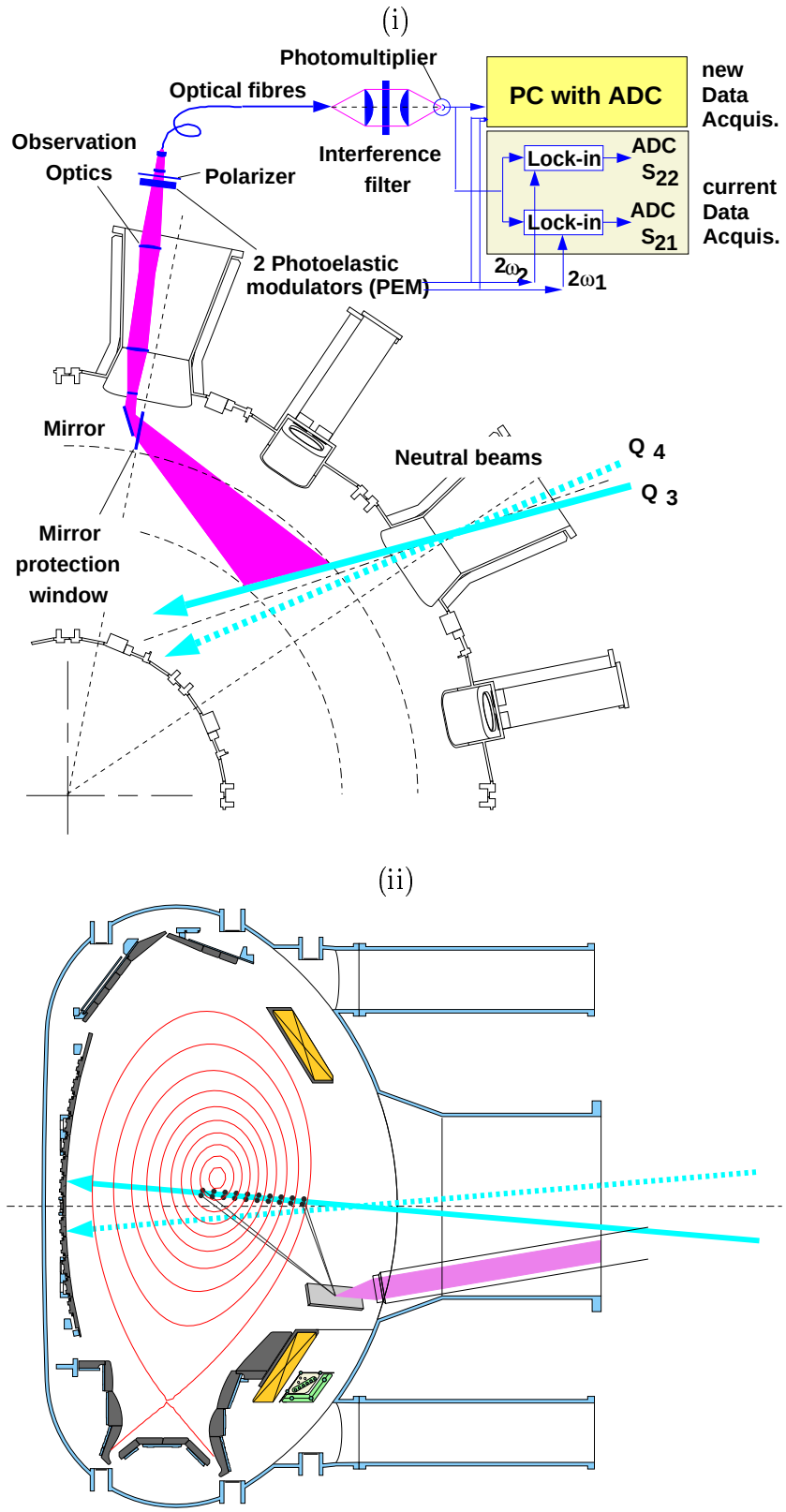

Figure 1.9: *(i) Overview of the MSE diagnostic from the top in ASDEX Upgrade, (ii) Poloidal cross section of ASDEX Upgrade showing the MSE diagnostic*

account in the calculation of the measured pitch angle. Due to the location of the lenses in a strong magnetic field they are constructed out of near-zero Verdet constant glass to avoid Faraday rotation of the light. The PEMs are essentially birefringent materials which causes the rotation of the linearly polarised light. After passing through the sheet polariser this rotation is converted into a amplitude modulation, which is proportional to the sine of the angle of polarisation of the incident light. By adjusting the second PEM it is also possible for the amplitude modulation to be proportional to the cosine of the angle of polarisation.

The light now travels along the optical fibres into a remote diagnostic centre. First the light is filtered through an interference filter system which is tuned to the doppler-shift of the neutral beam D_α σ line of interest, σ lines are used to maximise the polarisation fraction. Next a photomultiplier tube amplifies the signal. Finally, using this signal and 2 lock-in amplifiers, which are are set to the resonant frequencies of the 2 PEMs, the angle of polarisation of the linearly polarised light (γ) is calculated.

Due to the experimental limitations of most tokamaks, optimum MSE viewing geometry is impossible to achieve. In AUG the heating beams are inclined at 4.9° to the torus midplane so it is impossible to obtain horizontal viewing geometry. Thus the measured MSE angle ($\gamma\prime$) is not a direct measure of the magnetic pitch angle as given in Eqn. 1.37. The observation geometry must be taken into account and γ' gives a rational function of the components of $\mathbf{B}_\theta$, $\mathbf{B}_\phi$ and the radial electric field

$$tan(\gamma') = \frac{A_1 B_r + A_2 B_\phi + A_3 B_z + A_4 E_r + A_5 E_z}{A_6 B_r + A_7 B_\phi + A_8 B_z + A_9 E_r}, \tag{1.37}$$

where B_r and B_z are the cylindrical components of $\mathbf{B}_\theta$, A_i are the calibration geometrical constants, E_r and E_z are components of the radial electric field. The fact that the measured angle is not a direct measurement of the magnetic pitch angle but a rational function related to the magnetic pitch angle is important and will be dealt with in later chapters. The spatial resolution of MSE diagnostic, which depends on the angle between the observation lines of sight and the magnetic field at the point of its intersection with the neutral beam, drops from 6cm at the centre of the plasma to 2cm at $\rho_\psi = 0.3$ then rises again to 9 cm at the plasma edge for AUG. The AUG MSE diagnostic has a sampling rate of 1kHz but a 300Hz anti-aliasing filter combined with the fact that the diagnostic signal is averaged over 3 time points reduces the time resolution to 3ms. The combination

of these two facts leads to an experimentally measured error in γ of $\pm 0.2^{\circ}$ for the AUG MSE diagnostic. The $\pm 0.2^{\circ}$ error represents the maximum possible errors associated with the MSE diagnostic, where in reality the MSE diagnostic error can be any value between these bounds.

1.5 Outline of Thesis

The real-time recovery of plasma parameters in AUG is based on function parameterization FP, which is a method of predicting physical parameters of a system by means of statistical analysis of a simulated dataset of the said parameters and diagnostic signals. Presently only a set of external magnetic diagnostic signals are used to recovery AUG plasma parameters. Due to the lack of internal measurements it is not possible for the real-time recovery system to accurately recover the q-profile. The aim of this work is included extra diagnostic signals, specifically internal motional Stark effect diagnostic signal, into the present FP recovery routine to accurately and rapidly recover the AUG q-profile.

Chapter. 1 presented the practical motivation behind the nuclear fusion project. Fundamental fusion relevant physics was also presented, specifically the basic physics associated with the more important aspects of this work. The motional Stark effect diagnostic and q-profile were discussed in detail.

Chapter. 2 deals with the statistical methods associated with FP and describes the FP approach to recovering physical parameters.

Chapter. 3 describes the database analysis which was carried out and led to the FP model. Recoveries of database simulated q-profiles are presented to illustrate the accuracy of the FP model.

In Chapter. 4 data from AUG discharges is used to recovery AUG q-profiles via the AUG interpretive equilibrium code CLISTE and FP methods. A comparison between the two method is done to assess the accuracy of the new FP recovery method.

FP involves finding a dimensionally reduced set of linear combinations of the original diagnostic measurements, which are used to build the FP model. In Chapter. 5 a new approach to finding a more compact FP model of linear combinations of the original diagnostic measurements, using nonlinear methods, is presented and results using AUG

discharges are shown.

Chapter 2

Statistical and Experimental Background

2.1 Statistical Methods

2.1.1 Nomenclature

At this point it is important to outline some basic statistical definitions and terminology which will form the basis of this work.

Consider the matrix $\mathbf{X}$, matrices will be denoted by bold capital letters, vectors are denoted by bold lower case letters and matrix elements are denoted by lower case letters, where $\mathbf{X}$ is a $n \times p$ matrix. The data matrix is constructed from n observations of p measurements of variables. The matrix elements x_{ji} corresponds to the j^{th} measurement of the i^{th} variable.

The sample mean value of the variable $\mathbf{x}_i$ is denoted by $\bar{\mathbf{x}}_i$, and is defined as

$$\bar{\mathbf{x}}_i = \frac{1}{n} \sum_{j=1}^{n} x_{ji}. \tag{2.1}$$

Similarly the sample variance of $\mathbf{x}_i$ is denoted by s_{ii}, and defined as

$$V(\mathbf{x}_i) = s_{ii} = \frac{1}{n-1} \sum_{j=1}^{n} (x_{ji} - \bar{\mathbf{x}}_i)^2. \tag{2.2}$$

The standard deviation, or spread σ of $\mathbf{x}_i$ is equal to the square root of $V(\mathbf{x}_i)$.

The covariance s_{ij} between $\mathbf{x}_i$ and $\mathbf{x}_j$ is

$$s_{ij} = \frac{1}{n-2}\sum_{k=1}^{n}(x_{ki} - \bar{\mathbf{x}}_i)(x_{kj} - \bar{\mathbf{x}}_j), \tag{2.3}$$

s_{ij} forms the $p \times p$ covariance matrix $\mathbf{S}$, the $p \times p$ correlation matrix $\mathbf{R}$ can be obtained from $\mathbf{S}$ by defining the correlation coefficient r_{ij} to be

$$r_{ij} = \frac{s_{ij}}{\sqrt{s_{ii}s_{jj}}}. \tag{2.4}$$

It is obvious from their construction that the correlation and covariance matrices are symmetric. If the correlation matrix is equal to the identity matrix δ_{ij} then the p variables are said to be uncorrelated. The closer the correlation matrix element r_{ij} is to (-)1, the greater the (anti-)correlation.

2.1.2 Principal Component Analysis

Principal component analysis (PCA) was first proposed by Pearson in 1901 [20] and further developed by Harold Hotelling in 1933 [21]. PCA uses the covariance matrix (or a covariance-like matrix) of the $(n \times p)$ data matrix $\mathbf{X}$, to create orthogonal linear combinations of the data with minimal loss of information. These linear combinations can be analysed to look for the smallest subset of linear combinations which best describes the data. This attempt to reduce dimensionality can be described as 'parsimonious summarisation' of the data. PCA is treated in many standard texts, only a brief review is given here and is based mainly on [22], [23] and [8].

Using the spectral decomposition theorem, it is possible to write the Hermitian real covariance matrix $\mathbf{S}$, of $\mathbf{X}$, as

$$\mathbf{S} = \mathbf{GLG'}, \tag{2.5}$$

where $\mathbf{G}$ is the orthogonal matrix of eigenvectors of $\mathbf{S}$ (the i^{th} eigenvector $\gamma_\mathbf{i}$ forms the i^{th} column of $\mathbf{G}$) and $\mathbf{L}$ is a diagonal matrix of the eigenvalues ${\lambda_i}^2$ of $\mathbf{S}$, ${\lambda_1}^2 \geq {\lambda^2}_2 \geq ... \geq \lambda_p^2 \geq 0$. In this work $\mathbf{G'}$ is transpose of $\mathbf{G}$. It will be shown later that the variance of the i^{th} principal component is equal to ${\lambda_i}^2$.

The r^{th} principal component transformation is given by

$$\phi_r = \mathbf{G'}(\mathbf{x_r} - \bar{\mathbf{x}}), \qquad r = 1, ..., n \tag{2.6}$$

where $\mathbf{x_r}$ is the $p \times 1$ vector consisting of the r^{th} row of observations in the data matrix $\mathbf{X}$.

The i^{th} principal component score ϕ_{ri} of the vector of observations $\mathbf{x}_r$ is given by

$$\phi_{ri} = \gamma_{\mathbf{i}}'(\mathbf{x_r} - \bar{\mathbf{x}}) = (\mathbf{x_r} - \bar{\mathbf{x}})'\gamma_{\mathbf{i}} = \sum_{\mathbf{j=1}}^{\mathbf{p}} (\mathbf{x_{rj}} - \bar{\mathbf{x}}_{\mathbf{j}})\gamma_{\mathbf{ji}}. \tag{2.7}$$

Collecting all the values of the i^{th} principal components: $\phi_{ri}, r = 1, ..., n$ we get the i^{th} principal component vector

$$\phi_{\mathbf{i}} = \mathbf{C}\gamma_{\mathbf{i}} \tag{2.8}$$

where $\mathbf{C}$ is the centred data matrix $(\mathbf{X} - \mathbf{I}\bar{\mathbf{x}}')$.

The matrix $\mathbf{G}$ is orthogonal and its columns form an orthonormal basis where $\gamma_i\gamma_j' = \delta_{ij}$. It follows that for the $(n \times p)$ matrix of principal component transformed measurements $\mathbf{\Phi} = \mathbf{CG}$

$$\mathbf{\Phi\Phi}' = \mathbf{CGG}'\mathbf{C}' = \mathbf{CIC}' = \mathbf{CC}'. \tag{2.9}$$

This demonstrates that the principal component transformation is a length-preserving transformation and thus equivalent to a rotation of the coordinate axes in such a way that the new axes coincide with the directions in p-space defined by the covariance matrix's eigenvectors.

The covariance of $\phi_{\mathbf{i}}$ and $\phi_{\mathbf{j}}$ is

$$s_{ij} = \phi_{\mathbf{i}}'\phi_{\mathbf{j}} = \gamma_i'\mathbf{C}'\mathbf{C}\gamma_j = \gamma_i'\mathbf{S}\gamma_j = \lambda_j^2\delta_{ij}. \tag{2.10}$$

Thus the variance of the i^{th} principal component is equal to ${\lambda_i}^2$.

As will be seen in the proceeding chapters, it is useful to have an 'overall spread' of the raw data. Of particular interest is the total variance of the data $\sum_{i=1}^{p} s_{ii}$, also known as the trace of $\mathbf{S}$. For Hermitian matrices the trace of $\mathbf{S}$ is equal to the sum of the eigenvalues of $\mathbf{S}$ so $\sum s_{ii} = \sum \lambda_i^2$. Thus principal component transformations conserve total variance of the data.

To summarise

- Principal component transformations of data conserves length and total variance of data and can be seen as a rotation of the data along the p-space associated with p eigenvectors associated with $\mathbf{S}$.

- The mean of each principal component is zero (obvious from Eqn. 2.8) while the spread of each principal component is given by the square root of its related eigenvalue.

- Each principal component is an uncorrelated linear combination of the original data.

As previously stated, it is possible to carry out PCA on either the covariance or correlation matrix. The advantages and disadvantages of each procedure are as follows.

Covariance based PCA is particularly applicable to variables of compatible units. It has the advantage that the units do not depend on the uncertainties and variability of the secondary transformation. The eigenvalues of the principal components are in the same units as the original variables. Correlation based PCA is used in situations where the units of the variables are incompatible, but it should be noted that as the correlation matrix does not reflect the amount of variation on a physically relevant scale, correlation based PCA should be avoided when investigating multicollinearity.

2.1.3 Multi-linear Regression

This brief overview of ordinary least squares (OLS) multi-linear regression is based primarily on [24], [22] and [8].

Consider the model defined by

$$\mathbf{Y} = \mathbf{X}\alpha + \mathbf{e} \qquad \mathbf{e} \sim N(0, \mathbf{I}\sigma^2), \tag{2.11}$$

where $\mathbf{Y}$ is the $n \times 1$ known dependent variable matrix, α is the $p \times 1$ unknown regression parameter vector, $\mathbf{X}$ is the $n \times p$ known independent variable matrix and $\mathbf{e}$ is the random error matrix. It is more common for the independent measurements to be referred to as the measurements and the dependent variables to be called the parameters when this model is applied to a physical system.

Eqn 2.11 implies that the errors are homoscedastic (have equal random variance) and are normally distributed and that the predictors are known exactly, which are two important criteria for an accurate OLS regression.

The principal objective of regression analysis is to find the optimal estimates for the regression parameters. There are several optimality criteria. One of them states that an optimal estimator should be unbiased, i.e. its expectation value should equal the true parameter value and it should also have the minimal covariance.

Using the method of least squares to find an estimator, $\hat{\alpha}$ of α the residual sum of squares

$$\hat{\mathbf{e}}'\hat{\mathbf{e}} = (\mathbf{Y} - \hat{\mathbf{Y}})'(\mathbf{Y} - \hat{\mathbf{Y}}), \tag{2.12}$$

is minimised, where $\hat{\mathbf{Y}} = \mathbf{X}\hat{\alpha}$ is the matrix of fitted values of $\mathbf{Y}$, and $\hat{\mathbf{e}}$ is the matrix of empirical residuals.

Eqn 2.12 is differentiated w.r.t. $\hat{\alpha}$,

$$\frac{\delta\hat{\mathbf{e}}'\hat{\mathbf{e}}}{\delta\hat{\alpha}} = 0, \tag{2.13}$$

yields the following normal equations (see [8] for a complete description of the intermediate algebraic steps)

$$\mathbf{X}'\mathbf{X}\hat{\alpha} = \mathbf{X}'\mathbf{Y}. \tag{2.14}$$

If $\mathbf{X}'\mathbf{X}$ is invertible, which is not always possible and will be discussed in the following sections, then the unique solution exists:

$$\hat{\alpha} = (\mathbf{X}'\mathbf{X})^{-1}\mathbf{X}'\mathbf{Y}. \tag{2.15}$$

The estimator $\hat{\alpha}$ is unbiased

$$E(\hat{\alpha}) = [(\mathbf{X}'\mathbf{X})^{-\mathbf{1}}\mathbf{X}']E(\mathbf{Y}) = (\mathbf{X}'\mathbf{X})^{-1}\mathbf{X}'\mathbf{X}\alpha = \alpha. \tag{2.16}$$

As $\mathbf{e} \sim N(0, \mathbf{I}\sigma^2)$, the covariance matrix of $\hat{\alpha}$ is

$$V(\hat{\alpha}) = (\mathbf{X}'\mathbf{X})^{-1}\sigma^2. \tag{2.17}$$

And it can be proven using the Gauss-Markov theorem [22] that Eqn. 2.17 is the smallest covariance matrix of any linear estimator. Thus following the outlined optimality criteria $\hat{\alpha}$ is the best linear unbiased estimator (BLUE).

2.1.4 Function Parameterization

Introduction

Function parameterization (FP) is a method of predicting physical parameters of a system by means of statistical analysis of a simulated dataset, which spans the relevant vector space of experiments, to find a simple functional form of the parameters in terms

of the measurements. FP was developed by H. Wind for the purpose of momentum determination from spark chamber data [25], [26]. FP was first introduced to ASDEX by B. Braams as method of recovering certain geometric parameters from a circular plasma using magnetic measurements [10]. A magnetic measurements based FP model was created by P.J. McCarthy for the ASDEX successor Tokamak ASDEX Upgrade [8]. FP techniques have also been applied to fast equilibrium interpretations of the W7-AS stellarator [9]. In this work the FP model will be expanded to include internal MSE measurements which will be used to recover AUG's safety factor profile.

FP can be broken down into three main steps:

- Generation of a simulated database of the physical system.
- Statistical analysis of the database to find dimensionally reduced set of predictors from the measurements to describe the parameters of interest.
- Use of this model to recover parameters from real measurements.

The first two steps in this process can be very time consuming, but the main advantage of FP is that these step can be performed 'offline'. Because of the computational simple functional relationship between the measurements and the parameters the recovery is very fast when compared to standard iterative equilibrium codes. Computational times for plasma parameter recovery using the interpretive equilibrium code CLISTE [27] is orders of magnitude greater than the recovery times using FP.

Mathematical Description

Understanding the principles of FP is central to understanding this work therefore the excellent mathematical description of FP from Chapter 4 [10] is reproduced here.

A physical system is considered, of which S denotes a typical state. The system may have any number of degrees of freedom, but interest will be restricted to a (partial) characterisation by f intrinsic real parameters, represented collectively by a point $\mathbf{y} \in \Re^r$. In the experimental situation $\mathbf{y}$ is to estimated from the readings of p measurements, represented by a point $\mathbf{x} \in \Re^d$. It is assumed that $\mathbf{y}$ is completely specified by S, but that $\mathbf{x}$ may be a stochastic function of S, the stochasticity being due to random errors in the measurement process. We will write $\mathbf{y} = \mathbf{y}(S)$ and $\mathbf{x} = \mathbf{x}(S)$.

The aim of function parameterization is to obtain some reasonably simple function, $\mathbf{F} : \Re^d \rightarrow \Re^r$, such that for any state S the associated $\mathbf{y}(S)$ and $\mathbf{x}(S)$ satisfy $\mathbf{y} = \mathbf{F}(\mathbf{x}) + \mathbf{e}$

for a sufficiently small error term $\mathbf{e}$. The functional form of $\mathbf{F}$ may typically be chosen as a low-order polynomial in only a few linear combinations of the components of $\mathbf{x}$. The unknown coefficients in $\mathbf{F}$ are the determined by the analysis of a database containing the values of the parameters $\mathbf{y}_i$ and of the measurements $\mathbf{x}_i$, corresponding to n simulated states S_i $(1 \leq i \leq n)$. This is a problem of function fitting over scattered data in the high-dimensional space $\Re^d$, for which the use of methods from multivariate statistical analysis is appropriate. To a statistician the $\mathbf{x}_i$ are the 'conditions', the $\mathbf{y}_i$ are the 'responses', $\mathbf{F}$ is a 'regression', and the function fitting is the multi linear regression analysis. The terminology of the condition and the responses is very unnatural in the present context, and instead we will refer to these as the measurements and the physical parameters.

Notes on Database Generation and Predictor Selection

FP techniques can be applied to any system that can be described by a physical model. A computer code based on this physical model is used to generate the database of randomly varied simulated states of the physical system $\Re^d$. It is important to note that the accuracy of FP recovery of the system parameters depends on the accuracy of $\Re^d$. Obviously the accuracy of FP cannot exceed the accuracy of the physical model. It is also important that $\Re^d$ covers all possible values of $\Re^r$ as the FP model is likely to fail if it is used to recover $\mathbf{y}_i$ which is not spanned by $\Re^d$.

From $\Re^d$ a set of predictors is made from a dimensionally reduced set of linear combinations of the original measurements. It is very rare that individual measurements $\mathbf{x}^\mathbf{j}(1 \leq \mathbf{x}^\mathbf{j} \leq p)$, where p is the number of measurements to be used in the FP model, are uncorrelated. The inclusion of redundant measurements is detrimental to the FP model. Including excess measurements into the model increases the model size and thus can lead to over-fitting and an unrealistically accurate FP model. The dimension reduction method used in this work is PCA, although it is possible to use other methods such as latent root regression [28] and canonical correlation [22]. More insidious is that correlated measurements leads to collinearity or near collinearity of the set of predictors and this causes the FP model to become unstable [29], specifically the $(\mathbf{X}'\mathbf{X})^{-1}$ matrix in Eqn. 2.15 can have extremely large eigenvalues. As PCA is been used to eliminate collinearity of the predictors it is important that the covariance matrix is used rather than the correlation matrix for reasons stated earlier in this chapter.

Up to this point it has being assumed that the measurements $\mathbf{x}_\mathbf{i}^\mathbf{j}$ are perfectly accu-

rate, this is of course not realistic as there is a certain inaccuracy associated with all measurements. Although one of the criteria necessary for an ordinary least squares regression to be applicable to a problem is that the measurements be noiseless, it will be shown later in this chapter that this criteria can be 'loosened', if the variation of the noise in the measurements are small relative to the variation of the measurements themselves. The noisy measurements can be used in choosing the optimum number of linear combinations of original measurements $\mathbf{p}_r$ needed to form the best set of predictors. If multicollinearity exists between the measurements then the eigenvalues of the covariance matrix of the noiseless measurements associated with principal components of negligible variance, hence no predictive value, will go towards zero. The noisy measurements covariance matrix eigenvalues tend towards the value of the variance of the noise added to the measurements. The random nature of the noise adds a variance to the measurements which is independent of physical system and as the eigenvalues of a covariance matrix is associated with variance of the component variables, the baseline eigenvalue is shifted from zero associated with noiseless measurements to the variance of the noise when analysing the noisy measurements. Thus any principal components with eigenvalues comparable to or above the variance of the noise will have predictive value. The noise level associated with each measurements is based on the experimental accuracy of the diagnostic and chosen independent of any statistical methods.

Notes on the Regression Model and Practical Application

Errors in Measurements [8] For an ordinary least squares regression it is assumed that measurements $\mathbf{X}$ are known exactly. But in our case there are experimental errors associated with the diagnostic measurements being using as the basis of the FP predictors. Here it will be shown that if the variation of the noise is small compared to the variation of the related measurement then the optimality criteria still holds.

Consider the model defined by

$$\hat{\mathbf{Y}} = (\mathbf{X} + \triangle)\alpha, \tag{2.18}$$

which is analogous to Eqn. 2.11 but has an extra noise $n \times p$ matrix term $\triangle$. $\triangle$ consists of uncorrelated error terms $\triangle_i$, with $\triangle_i = N(0, \sigma)$. Similarly we find $\hat{\alpha}$ to minimise the residual sum of squares

$$RSS = (\mathbf{Y} - (\mathbf{X} + \triangle)\alpha)(\mathbf{Y} - (\mathbf{X} + \triangle)\alpha). \tag{2.19}$$

$\triangle$ is totally random and thus uncorrelated with either $\mathbf{X}$ or $\mathbf{Y}$, the estimator for $\hat{\alpha}$ is given by

$$(\mathbf{X} + \triangle)'(\mathbf{X} + \triangle)\hat{\alpha} = (\mathbf{X} + \triangle)'\mathbf{Y}. \tag{2.20}$$

This treatment is for normal multi-linear regression, in this work principal component regression is used and substituting $\mathbf{\Phi}$ for $\mathbf{X}$ gives

$$\hat{\alpha} = (\mathbf{\Phi'\Phi} + n\sigma^2\mathbf{I})^{-1}\mathbf{\Phi'Y} \tag{2.21}$$

$$\hat{\alpha} = (diag(n{\lambda_i}^2) + n\sigma^2\mathbf{I})^{-1}\mathbf{\Phi'Y}$$

$$\hat{\alpha} = diag(n{\lambda_i}^2 + n\sigma^2)^{-1}\mathbf{\Phi'\Phi}(\mathbf{\Phi'\Phi})^{-\mathbf{1}}\mathbf{\Phi'Y}$$

$$\hat{\alpha} = diag(1/(n{\lambda_i}^2 + n\sigma^2))diag(n{\lambda_i}^2)\hat{\alpha}(\mathbf{0})$$

$$\hat{\alpha} = diag({\lambda_i}^2/({\lambda_i}^2 + \sigma^2))\hat{\alpha}(\mathbf{0}) \tag{2.22}$$

Each noisy regression parameter can be written in terms of it corresponding noiseless regression parameter as

$$\hat{\alpha}_\mathbf{i}(\mathbf{0}). \tag{2.23}$$

It is obvious from this equation that if $\sigma^2 \ll {\lambda_i}^2$ then the noise in the measurements is insignificant and ordinary least squares can be used.

Importance of Using a Testing Dataset For practical application of a regression model to a physical system it is important to split the database into a training and test datasets. The regression model is 'trained' on the training dataset and the accuracy of the model is found by analysing results from the test dataset.

Intuitively, it is better to test the regression model on data which was not used to create the regression model and thus better simulates the practical situation where the experimental data is previously unknown prior to the application of the regression model.

In practice, the use of a testing dataset is a necessary to avoid 'over fitting' of the data. The phenomenon of 'over fitting' leads to an very small error with regards to the training dataset model, but also results in a poor representation of the testing dataset model. The 'over fitting' is due to an overly large regression model which has been trained

to the noise associated with the training dataset. When this 'over fitted' model is used on a different set of data it performs poorly. Choosing the regression model via analysis of a test dataset over comes this problem.

Chapter 3

q-Profile Recovery Using FP Methods

3.1 Introduction

This chapter outlines the FP methods used to recover AUG q-profiles. The simulated database of AUG equilibria which the FP method is based on is described in detail. The construction of the PCA FP model is outlined, and finally FP recoveries of AUG database q-profile are presented.

3.2 Equilibrium Database

3.2.1 Database Generation Method

As stated in Chapter 1, ideal MHD equilibrium models for axisymmetric tokamak systems are based on the G-S equation,

$$-\triangle^*(\psi) = \mu_0 R^2 p'(\psi) + f f'(\psi) = \mu_0 R J_\phi(r,z).$$

For the purposes of generating the AUG FP database, the G-S equation is solved using randomly chosen p', ff' function parameters taking into account the AUG experimental setup.

Initially the toroidal current density $J_\phi(r,z)$ is chosen to be constant J_ϕ^0 on a rectangular block with $I_p = 1MA$.

The G-S equation for the plasma flux ψ^1_{plas}

$$-\triangle^*(\psi^1_{plas}) = \mu_0 R J^0_\phi. \tag{3.1}$$

is solved using the equilibrium flux surface topology from the initial estimate J^0_ϕ.

The equilibrium flux ψ^1_{eq} is given

$$\psi^1_{eq} = \psi^1_{plas} + \psi_{vac} \tag{3.2}$$

where ψ_{vac} is the known fixed vacuum flux.

From the right-hand side of the G-S equation, the toroidal current density is generated using the relationship

$$J^1_\phi(r,z) = Rp'(\psi^1_{eq}) + \frac{ff'(\psi^1_{eq})}{\mu_o R}. \tag{3.3}$$

Solving the G-S equation for $(J^1_\phi(r,z))$ yields ψ^2_{plasma}, from which ψ^2_{equil} is generated. This cycle continues until the difference between ψ^n_{equil} and ψ^{n-1}_{equil} is very small, at which stage the process is said to have converged.

Although the converged equilibrium satisfies the G-S equation; post-processing tests are carried out to check if the equilibrium is within AUG operating limits, specifically

- Coil current limits, individual poloidal field PF current and limits to inter-PF coil forces.
- Vertical stability limits.
- Plasma size, reject tiny plasmas.
- Limits on plasma parameters; i.e. β_p, li, ... ,etc.

It should be noted that between the convergence and operation tests less than 10% of all attempts at generating relevant AUG equilibria are successful. For a complete description of AUG FP database generation see (Chap. 3. [8])

3.2.2 Database Vector Space Expansion

The accuracy of any FP model depends on the FP database spanning the entire vector space of all possible states of the physical system. Previously the AUG FP recovery system was based on magnetic diagnostic measurements, shown in Fig. 3.1

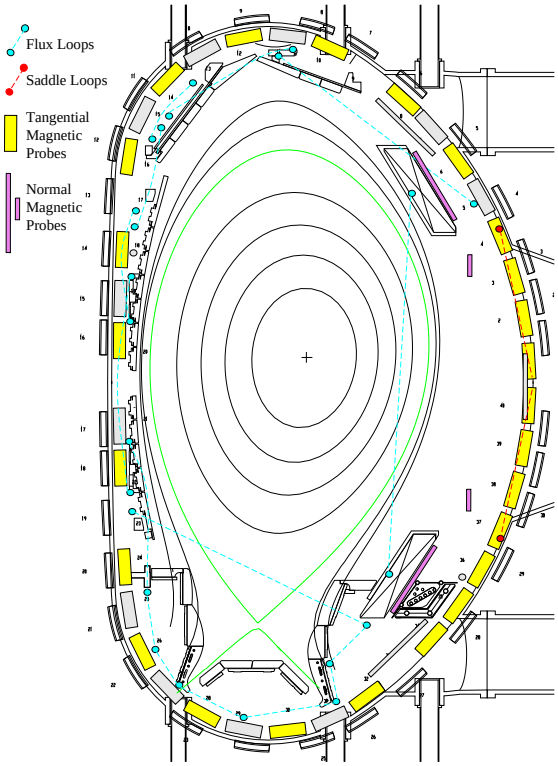

Figure 3.1: *Cross-section of AUG indicating the positions of the magnetic diagnostics.*

which were used to recover AUG parameters. Thus only parameters which could be readily identifiable by magnetic signals could be recovered accurately, such as geometric parameters, q_{95},...,etc. The variation in the G-S equation source profiles ff', p' was, prior to this work, described by

$$J_\phi = R\underbrace{\hat{\psi}^{a_p}(e^{b_p x + c_p x^2 + d_p x^3} + g_p e^{-(h_p\hat{\psi})^2})}_{p'(\hat{\psi})} + \frac{1}{\mu_0 R}\underbrace{\hat{\psi}^{a_f}(e^{b_f x + c_f x^2 + d_f x^3} + g_f e^{-(h_f\hat{\psi})^2})}_{ff'(\hat{\psi})}, \qquad (3.4)$$

where $\hat{\psi}$ is unity at the magnetic axis and zero on the last current carrying surface, which need not coincide with the plasma boundary, and $x = 1 - \hat{\psi}$.

The first terms in the p' and ff' profiles consist of a bulk plasma term comprising of a simple power term $\hat{\psi}^a$ modulated by an exponential cubic polynomial, the second term mainly used to describe the edge bootstrap current, is a Gaussian peak localised towards the plasma edge.

For the magnetic signal based AUG FP where the emphasis was on recovery of flux surface topology the variation in the G-S equation p' and ff' profiles was sufficient to accurately describe the relevant AUG experimental vector space.

When recovering the q-profile by the addition of MSE diagnostic signals to the FP

recovery routine, it was found that the variation in the p' and ff' profiles bulk plasma term's exponential cubic polynomial was inadequate for realistically describing the variation of the current density profile and related parameters, i.e. q-profile. For this reason, a new database was generated with emphasis on increasing the variation of the p' and ff' profiles, which would then span the relevant experimental vector space of the AUG tokamak for the accurate recovery of the q-profile.

The ff' and p' profiles are currently based on a set of N_b linear combination of weighted basis functions.

$$ff', p'(\psi) = S(\psi).\sum_{j=1}^{N_b} \alpha_j \mathbf{b}_j, \tag{3.5}$$

where $N_b \leq 25$ linear combinations.

The discrete cosine transform is used to generate orthogonal basis functions ($\mathbf{b_j}$).

$$\mathbf{b_j} = \sqrt{\frac{\min(j,2)}{m}} \cos\left((2i-1)(j-1)\frac{\pi}{2m}\right) \qquad i = 1, m \tag{3.6}$$

where $m = 1000$ is the number of grid-points for the source profiles.

The linear combinations are weighted by a geometric decay function(α_j) which controls the smoothness of the p' profile.

$$\alpha_j = \tilde{\phi}_j \, r_{\text{decay}}^{j-1}; \qquad r_{\text{decay}} \in [.3, 0.7] \tag{3.7}$$

where $\tilde{\phi}_j$ is randomly chosen from a unit normal distribution and r_{decay} is the decay rate chosen randomly for this profile. With this scheme, the more rapidly the basis function varies spatially, the smaller its amplitude tends to be.

Edge features are introduced by scaling the the G-S variable input current (the poloidal field coil currents together with I_p) by a function which is unity except towards the edge. The functional form chosen is

$$S(\psi) = (1 - e^{\frac{-\hat{\psi}}{\lambda}})^{\delta}. \tag{3.8}$$

The fall-off length λ and the decay power δ are randomly chosen from the ranges $\lambda \in [0.005, 0.055], \delta \in [1, 2]$. The same method for solving the G-S equation is used with the addition of the the newly parameterised $p'(\phi)$ and $ff'(\phi)$ profiles.

3.2.3 Database Diagnostic Signals

The next step in the AUG equilibrium database generation is the post-processing step where the relevant diagnostic signals and plasma parameters are calculated for each stored database equilibrium flux grid.

At this point, it is necessary to outline the importance of the plasma current I_p and toroidal magnetic flux $\mathbf{B}_\phi$ when generating AUG equilibrium database diagnostic signals and plasma parameters. Scaling the G-S variable input currents by a constant factor does not alter the equilibrium flux geometry, thus varying I_p only scales $\mathbf{B}_\theta$ dependent magnetic diagnostic signals and plasma parameters by a constant term. The G-S equation is independent of $\mathbf{B}_\phi$ (Appendix A) and the post-processing parameter generation step for a magnetic-signals-only FP model normalises the plasma parameters and the magnetic diagnostic signals to an arbitrary $\mathbf{B}_\phi$ of 2.5T and I_p of 1MA. It is important to note that for the magnetic-signals-only FP model it is possible to scale this system of fixed I_p and $\mathbf{B}_\phi$ parameters and diagnostic signals by the corresponding I_p and $\mathbf{B}_\phi$ to span the entire variable I_p and $\mathbf{B}_\phi$ operational space of AUG.

An I_p and $\mathbf{B}_\phi$ constant database is inadequate when AUG MSE diagnostic signals $tan(\gamma_{exp})$

$$tan(\gamma_{exp}) = \frac{A_1 B_r + A_2 B_\phi + A_3 B_z + A_4 E_r + A_5 E_z}{A_6 B_r + A_7 B_\phi + A_8 B_z + A_9 E_r}, \tag{3.9}$$

are added to the equilibrium database. The $tan(\gamma_{exp})$ signals are rational functions of B_ϕ and components of $\mathbf{B}_\theta$ ($\sqrt{B_z^2 + B_r^2} = B_\theta$). Thus to span the operational space of the AUG MSE diagnostic it is necessary to vary I_p and B_ϕ in the post-processing calculation of the MSE signals following the generation of the equilibrium fluxes. Note the E_r, E_z corrections are set to zero as the expansion of the AUG MSE diagnostic setup [30], to include the measurements of the radial electric field, is not yet completed.

3.2.4 Database Scaling

The crux of this work is the inclusion of MSE diagnostic measurements into an FP model with a view of recovering the q-profile. In the previous section, it was shown that the magnetic signals are dependent on I_p and are independent of $\mathbf{B}_\phi$ while the MSE signals are dependent on both I_p and $\mathbf{B}_\phi$. It must be decided how to best treat each diagnostic

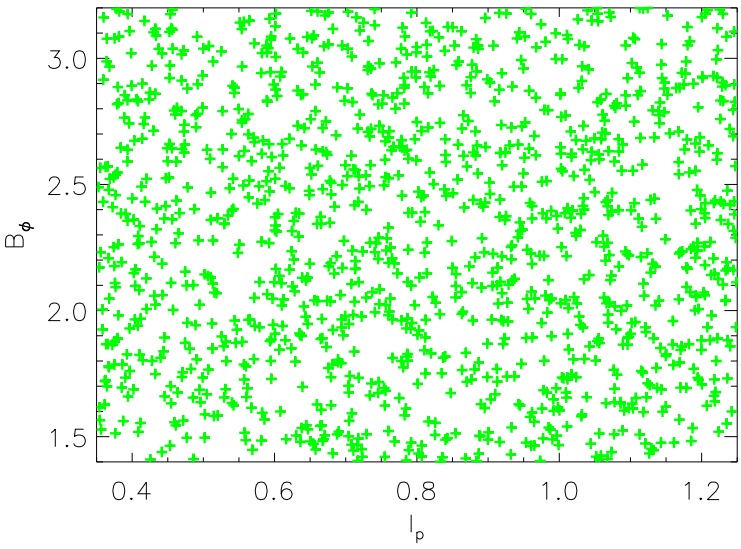

Figure 3.2: *Scatter plots of I_p versus $\mathbf{B}_\phi$ used in the database generation of the MSE signals, illustrating the population of all possible AUG operational configurations.*

signal's dependence on I_p and $\mathbf{B}_\phi$ in order to create an equilibrium database which can be used as the basis of an FP model.

The first of two possible solutions would be to create a database where both sets of diagnostic signals were generated using a variable I_p and $\mathbf{B}_\phi$. A plot of I_p against $\mathbf{B}_\phi$ is given in Fig. 3.2 to demonstrate the random variation of these quantities.

The extra variation in the q-profile due to the variable $\mathbf{B}_\phi$ would be unrecoverable by the magnetic signals as these are independent of $\mathbf{B}_\phi$. This would be detrimental to the accuracy of the final FP model, particularly in the region towards the edge of the plasma where it is possible to accurately recover the edge q-profile with magnetic measurements only, while the range of the MSE signals is limited and tends not to include the region towards the edge of the plasma.

The second option would be to 'unscale' the variable I_p and $\mathbf{B}_\phi$ MSE diagnostic measurements so that the final 'unscaled' MSE diagnostic measurements $tan(\gamma\prime)$ can be used in a fixed I_p and $\mathbf{B}_\phi$ FP database, the chosen values of I_p and $\mathbf{B}_\phi$ are 1MA and 2.5T respectively.

Before carrying out the unscaling of the MSE signals, it is important to note that there is a constant geometric offset angle, due to the vacuum toroidal magnetic field, associated with each of AUG's MSE diagnostic signals $tan(\gamma_{exp})$.

For 'ideal' MSE signals

$$tan(\gamma_{ideal}) = \frac{B_\theta}{B_\phi} \propto \frac{I_p}{B_\phi}, \tag{3.10}$$

in a toroidal magnetic field ($\mathbf{B}_\theta = I_p = 0$) the MSE signal is zero. For a toroidal magnetic field the rational functional form of $tan(\gamma_{exp})$ simplifies to the constant term

$$tan(\gamma_{offset}) = \frac{A_2}{A_7}. \tag{3.11}$$

It is necessary that this offset term be subtracted from the $tan(\gamma_{exp})$ prior to the unscaling of the database angle. If it was not subtracted, the constant term would be dependent on the variation of I_p and $\mathbf{B}_\phi$ and so cause added variance to the 'unscaled' angle $tan(\gamma\prime)$. This added variance would hinder the recovery of plasma parameters as this variance is independent of the plasma and would act as noise.

The relationship between $tan(\gamma_{ideal})$ and I_p , $\mathbf{B}_\phi$ is assumed to hold for $tan(\gamma_{meas})$ where $tan(\gamma_{meas})$ is defined as

$$tan(\gamma_{meas}) = tan(\gamma_{exp}) - tan(\gamma_{offset}). \tag{3.12}$$

Unscaling becomes the simple matter of multiplying $tan(\gamma_{meas})$ by the reciprocal of its relationship with I_p and $\mathbf{B}_\phi$, followed by normalising the angle to a constant I_p of 1MA and $\mathbf{B}_\phi$ of 2.5T. The 'unscaling' of the MSE diagnostic is summarised

$$tan(\gamma\prime) = \left(tan\left(\gamma_{exp}\right) - \frac{\mathbf{A_2}}{\mathbf{A_7}} \right) \times \frac{\mathbf{B}_\phi}{2.5} \times \frac{1}{I_p}, \tag{3.13}$$

and the final angle $tan(\gamma\prime)$ is included in the constant I_p and $\mathbf{B}_\phi$ database.

Fig. 3.3 illustrates the variation and mean values of the 10 AUG MSE channel for the four different scaling scenarios; constant I_p and $\mathbf{B}_\phi$ of 1MA and 2.5T, variable I_p and $\mathbf{B}_\phi$ (.35MA-1.25MA, 1.4T-3.2T), unscaled variable MSE angle minus the baseline and finally unscaled variable MSE angle including the baseline.

The MSE channels are labelled so that channel 1 is the outermost channel and channel 10 is towards the centre of the plasma. Channel 10 is not always the central channel due to the geometric variation of the plasma centre in the database. From the mean values of $tan(\gamma\prime)$, it is obvious that the mean value of the centre of the plasma is actually between channel 8 and channel 9. A trend seen in each scenario is that the variance of the angles decreases towards channel 10 and the variance of the final three MSE angles are the lowest and almost constant for each scenario. This is due to the MSE dependence on the $\mathbf{B}_\theta$.

The MSE angle is proportional to $\mathbf{B}_\theta$ and towards the centre of the plasma $\mathbf{B}_\theta$ goes to zero, therefore the variation of the measured MSE angle close to centre of the plasma is small. This fact will be shown to be of great important when calculating the error bars associated with the inner q-profile using MSE measurements as the primary diagnostic.

Central to the 'unscaling' of the MSE angles is the assumption that relationship between $tan(\gamma_{ideal})$ and I_p , $\mathbf{B}_\phi$, holds for $tan(\gamma_{meas})$. While this is not totally correct, due to the rational dependence of the $tan(\gamma_{meas})$ on I_p and $\mathbf{B}_\phi$, it can be seen that the spread of the $tan(\gamma\prime)$ and $tan(\gamma)_{\mathbf{I}_p,\mathbf{B}_\phi const.}$ is almost identical, thus this assumption is valid for this purpose.

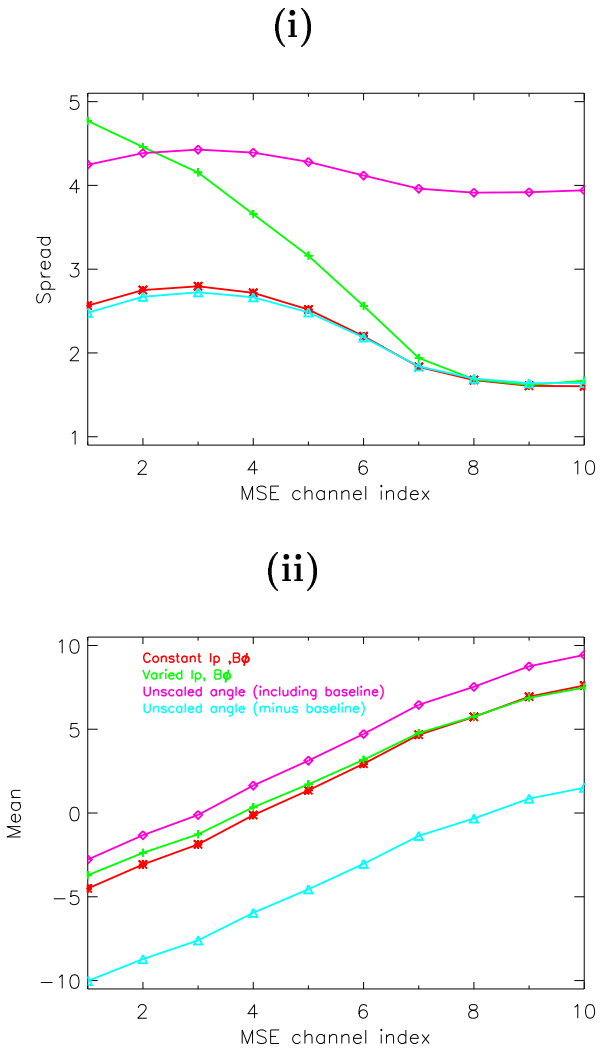

Figure 3.3: *(i) Spread of AUG MSE signals for various I_p and $\mathbf{B}_\phi$ scalings. (ii) Mean values of the same signals for the different I_p and $\mathbf{B}_\phi$ scalings. Note the spread in 'unscaled' (minus baseline) signals is very similar to that of the constant I_p and $\mathbf{B}_\phi$ signals.*

3.2.5 AUG FP Database Summary

Following the testing of randomly generated AUG equilibria the FP database consists of 3443 observations. The database contains single null lower divertor and single null upper divertor AUG equilibria. These are plasmas where the separatrix (last closed flux surface) X-point is adjacent to the lower or upper divertor respectively, as in Fig. 3.4. AUG is configured for divertor plasmas which leads of the greater control of the influx of impurities over physical limiter plasmas. Plasma impurities lead to energy loss from radiation and also to fuel dilution. An important source of impurities is sputtering from material surfaces, so it is important to distance the plasma from the vacuum vessel. Two techniques are currently used, the first is to define the outer boundary by a material limiter, while the second is modify the magnetic field to produce a remote magnetic divertor. In a limiter configuration the last closed flux surface is defined by the material limiter itself and thus neutral impurity atoms released from the surface are able to directly enter the confined plasma. In a divertor plasma the last closed flux surface is remote from the divertor itself and so does not suffer from this problem. Also as the outgoing particles target surface is separated from the plasma, impurity back-flow is restricted, which is an advantage when purging the plasma of intrinsic impurities, such as α-particles. Many divertor configurations are possible, but AUG works with a toroidally symmetric poloidal field divertor.

While all AUG shots start and end with transient limiter phases, the vast majority of shot have a flat top divertor configuration. Divertor configuration plasmas are associated with improved confinement of the plasma, specifically H-mode, improved H-mode and internal transport barrier ITB shots[1]. Limiter plasmas are associated with low confinement of the plasma, L-mode shots, although it also is important to note that ITB shots are possible in limiter plasmas. Also AUG was designed to be an (ITER) reactor-compatible experiment, which itself is designed for a divertor configuration operation. For these reasons, only single null upper and lower divertor plasmas are considered for this work.

[1] A description of AUG shot scenarios is given in chapter 4

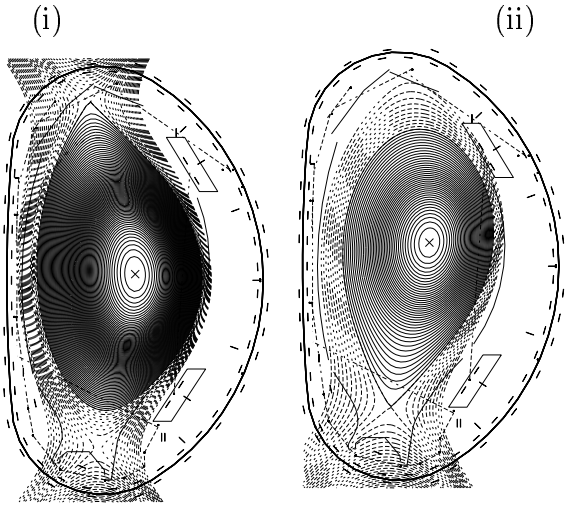

Figure 3.4: *AUG toroidal cross-section showing the magnetic flux surfaces for an (i) upper divertor and a (ii) lower divertor shot.*

χ^2 classification of database equilibria To best describe the variation of the safety factor profile in the FP database a χ^2 based statistic of the distribution of the diagnostic measurements will be used. For each equilibrium, the p measurements span p dimensional space. For our purposes, the set of PCA eigenvectors of these measurements form an orthogonal set of basis vectors which span this space, with each principal component vector $\phi_\mathbf{i}$ a projection along these basis vectors. Each of the p individual $\phi_\mathbf{i}$ are standardised by the root eigenvalue of the vector basis function (λ_i^2). These values are mutually independent standard normal variables and thus the variable $\sum_{i=1}^{p}\left(\frac{\phi_\mathbf{i}}{\lambda_i}\right)^2$ has a χ^2 distribution with a mean of p and variance of $2p$ [31]. As a reduced set of $\phi_\mathbf{i}$ cover almost all of the variance ($> 99\%$) of the measurements in the database a reduced χ^2 distribution is used.

$$d^2_{red} = \frac{1}{red}\sum_{i=1}^{red}\left(\frac{\phi_\mathbf{i}}{\lambda_i}\right)^2, \tag{3.14}$$

where red is the number of ${\phi_\mathbf{i}}^2$ needed to explain the majority of the variance of the measurements; 5 out of 10 (99.92% of the variance) in the case of the MSE diagnostic measurements. The value of the reduced χ^2 distribution is 1 at the centre of the equilibrium database.

The database includes plasmas with wide range of physical size and current den-

[2]For the remainder of this work the principal components $\phi_\mathbf{i}$ will be referred to as PCs, this is to avoid confusion with toroidal cylindrical co-ordinated ϕ

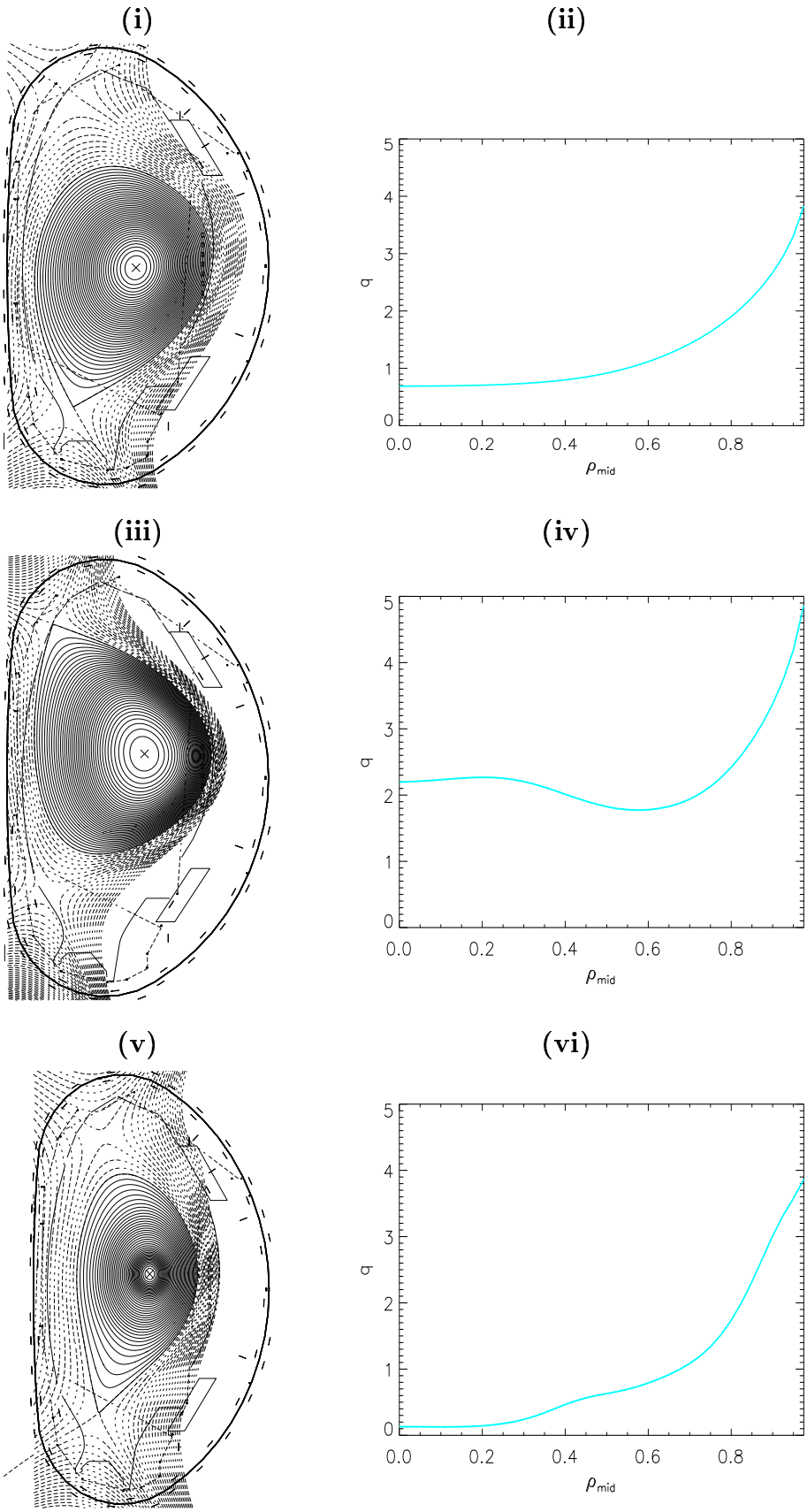

Figure 3.5: *illustrates the variation in database q-profiles. (i) shows the magnetic flux surfaces for the equilibrium with the minimum χ^2 value (0.016) in the database, (ii) show the q-profile for the same equilibrium; (iii),(iv) show the flux surfaces and the q-profile for the database equilibrium with a χ^2 value closest to 1; (v),(vi) show the flux surfaces and the q-profile for the database equilibrium with the maximum χ^2 value (34.434).*

sity dependent parameters. The database variation of several important AUG parameters is given in Table 3.1 , including the position of the magnetic axis(R_{mag}, Z_{mag}), the innermost(R_{in}) and outermost(R_{out}) position of the plasma boundary along the radial direction, the plasma volume(V), the plasma stored energy(W_{mhd}), β_θ, the safety factor value at axis and towards the edge of the plasma(q_0, q_{95}).

Parameter	Unit	Mean	Spread	Min.	Max.
R_{mag}	m	1.740	0.048	1.584	1.890
Z_{mag}	m	0.062	0.093	-0.191	0.291
R_{in}	m	1.205	0.074	1.047	1.415
R_{out}	m	2.129	0.040	2.050	2.205
V	m^3	10.038	1.417	6.793	15.652
β_θ		2.080	0.856	0.408	4.054
W_{mhd}	MJ	0.983	0.546	0.038	2.112
q_0		1.039	0.732	0.122	5.810
q_{95}		3.149	0.720	1.694	6.336

Table 3.1: *AUG FP database parameters*

3.3 FP Model

3.3.1 Preliminary Analysis

The first step in constructing the FP model is to decide how to best recover the q-profile. It will be shown that recovering the ι profile, which is the local inverse of the q-profile,

$$q = \frac{1}{\iota}, \tag{3.15}$$

is preferable to a direct q-profile recovery. This is due to the highly heterscedastic nature of error propagation in a direct q-profile FPJ regression.

Assuming a circular plasma cross-section, q can be approximated to be

$$q(r) = \frac{1}{2\pi} \oint \frac{B_\phi}{RB_\theta} ds \approx \frac{rB_\phi}{RB_\theta} = q(r).$$

This relationship can be re-expressed

$$q(r) = \frac{\epsilon(r)}{\gamma(r)}, \tag{3.16}$$

where $\gamma(r)$ is the local magnetic pitch angle $\mathbf{B}_\theta/\mathbf{B}_\phi$, and $\epsilon(r)$ is the local inverse aspect ratio $\epsilon = r/R$. Similarly

$$\iota = \frac{\gamma}{\epsilon}. \tag{3.17}$$

The errors associated with ϵ and γ are $\delta\epsilon$ and $\delta\gamma$ respectively. Basic differential error analysis of Eqns. 3.16 and 3.17 yields the following results (forcing all terms to be positive)

$$\delta q = \frac{1}{\epsilon}\left(q^2\delta\gamma + q\delta\epsilon\right) \tag{3.18}$$

$$\delta\,\iota = \frac{1}{\epsilon}\left(\delta\gamma + \iota\,\delta\epsilon\right). \tag{3.19}$$

Most insidious to an OLS q regression is the first term in Eqn. 3.18 $q^2\delta\gamma/\epsilon$ where the error in q is proportional to q^2. This shows that the errors associated with recovering the q profile directly are heteroscedastic, i.e. the q error variance scales as q^4. As stated in chapter 2, it is important that the errors are homoscedastic for an accurate OLS regression.

Eqn. 3.19 shows that an ι regression doesn't suffer from the same problem as $\delta\,\iota \propto \delta\gamma/\epsilon$. If the regression is carried out at fixed, or approximately fixed, ϵ intervals, then the second term of Eqns. 3.18 and 3.19 can be neglected and the errors associated with an ι regression would be homoscedastic.

At this point it is necessary to determine what is the best co ordinate over which to recover ι. Although ρ_ψ tends to be the co-ordinates of choice when working with the ι profile, it is not the proper co-ordinate with which to recover the ι profile using MSE based FP methods.

The ι regressions are carried out at fixed values of a geometric flux surface ρ_{mid} defined as the normalised mid-plane diameter of the flux surface

$$\rho_{\mathrm{mid}} = \frac{R_{\mathrm{out}}(\psi) - R_{\mathrm{in}}(\psi)}{\text{midplane plasma diameter}}. \tag{3.20}$$

ρ_{mid} is determined by by the flux surface topology, which is already reasonably determined by the magnetic measurements and thus the geometric position of each local ι value is known. This is necessary to optimised the recovery of ι profile using the MSE diagnostic as the primary diagnostic, as the MSE diagnostic channels are fixed in space.

By contrast ρ_ψ depends on the current density and hence $|\bigtriangledown \Psi|$, thus the absolute position of the ι profile is unknown over these co ordinates when recovering the profile using the MSE diagnostic and thus is detrimental to its recovery.

It should also be noted that ρ_{mid} varies little for fixed ϵ and thus when using this co ordinate system it is possible to ignore the second terms in Eqns. 3.18, 3.19 which is assumed in the previous analysis.

3.3.2 FP Model Construction

Diagnostic Signals The FPJ model is based on 10 MSE diagnostics measurements signals and 46 magnetic measurements signals. The MSE diagnostic measures the local magnetic pitch angle γ, thus is the primary diagnostic used for the recovery of the q-profile. The MSE diagnostic channels are fixed in space, so it is necessary to know the position and shape of the plasma relative to the MSE channels for an accurate recovery of the q-profile. For this reason, the magnetic signals are necessary. Previous work, [8] and [10], has shown that with magnetic diagnostic based function parameterisation models, it is possible to accurately recovery the shape and position of the plasma. Also with magnetic diagnostic signals it is possible to recover the q-profile towards the edge of the plasma, it is rare that the MSE channels span the outer edge of the plasma, thus the MSE channels are unable to accurately recover this part of the profile.

Measurement Noise The simulated diagnostic measurement signals in the FPJ database are the exact values associated with the database equilibria. For use in an FP model it is important to add simulated noise to these measurements. For a database model to reflect accurately experimental scenarios, it is necessary for the simulated measurements to have a similar uncertainty associated with the experimental signals. As the FPJ database is a subset of all possible experimental scenarios, it is also important to overcome the possibility of any small random correlation between the measurements in the database which does not reflect reality [29]. This effect would artificially improve the regression results but is drowned out by the addition of noise to the ideal measurements. For the MSE signals this noise is $\leq .2^o$, while for the magnetic signals this experimental uncertainty is 1mT.

Independent Plasma category Regression Models The FPJ database consists of single null upper divertor and single null lower divertor plasmas. For convenience these plasmas will be referred to, in local jargon, as category 3 and category 4 plasmas respectively[3]. To optimise the recovery of the separate plasma category q-profiles the database was split into two. Separate category 3 and category 4 PCA was carried out and the corresponding regression models were built. The reasoning behind this was that global category regressions were found to produce poor q-profile recoveries and separate category PCA optimises the PCs to yield the best regression model for each independent q-profile category recovery. The final results for each regression are presented in the results section of this chapter. Analysis from the category 3 plasma database subset is used to illustrate to intermediate steps leading to the final regression model.

Principal Component Analysis PCA of the Measurements The covariance based PCA results for the category 3 plasma subset are presented in Table. 3.2 in the form of the eigenvalues of the noiseless measurements [4]. Also shown is the culumative variance of the entire set of measurements and the highly collinear nature of each set of measurements is demonstrated. Only 4/10 PCs are needed to explain $> 99\%$ of the total variance for the MSE diagnostic signals and only 13/46 PCs are needed for the magnetic signals, indicating the high correlation and thus high collinearity between individual measurement signals. As stated in Chapter 2, for a regression with collinear measurements, $\mathbf{X'X}$ is of less than full rank, the inverse matrix in Eqn. 2.15 will not exist and therefore the regression coefficients will be undetermined. Even in the case of near collinearity where the eigenvalues can approach zero, the large eigenvalues of the inverse matrix will render the regression coefficients unstable [29]. Thus for the purpose of generating a robust FPJ regression model it is necessary to carry out PCA of the measurements to form PCs prior to regression analysis.

FP Regression Model In previous work [8] [9] [10] , low order polynomials have been sufficient for accurate recovery of fusion plasma parameters. It has also been shown to be possible to recover some global parameters using a linear model, with reasonable

[3]Category 1 and 2 plasmas refer to limiter plasmas and are beyond the scope of this work

[4]The noisy measurements will be scored with the eigenvectors associated with the noiseless PCA when constructing the PCs

MSE measurements eigenanalysis

PC index	Eigenvalue degrees^2	Cumulative Variance %
1	31.6317940	68.68
2	11.8077780	94.31
3	2.0009544	98.66
4	0.4592399	99.65
5	0.1241849	99.92
6	0.0258699	99.98
7	0.0063499	99.99
8	0.0025268	100
9	0.0007310	100
10	0.0002235	100

Magnetic measurements eigenanalysis

PC index	Eigenvalue T^2	Cumulative Variance %
1	0.07758863	36.36
2	0.04042881	55.31
3	0.03828662	73.25
4	0.01927910	82.29
5	0.01208639	87.95
6	0.00898383	92.16
7	0.00466397	94.35
8	0.00376906	96.12
9	0.00253715	97.30
10	0.00170566	98.10
11	0.00098224	98.56
12	0.00082576	98.95
13	0.00079043	99.32
14	0.00048821	99.55
15	0.00041957	99.75

Magnetic measurements eigenanalysis

PC index	Eigenvalue T^2	Cumulative Variance %
16	0.00030101	99.89
17	0.00009121	99.93
18	0.00007997	99.97
19	0.00003476	99.98
20	0.00001854	99.99
21	0.00000822	100
22	0.00000300	100
23	0.00000265	100
24	0.00000053	100
25	0.00000024	100
26	0.00000007	100
27	0.00000004	100
28	0.00000002	100
29	0.00000001	100
30	0.00000001	100

Table 3.2: *Eigenanalysis for MSE and magnetic measurements*

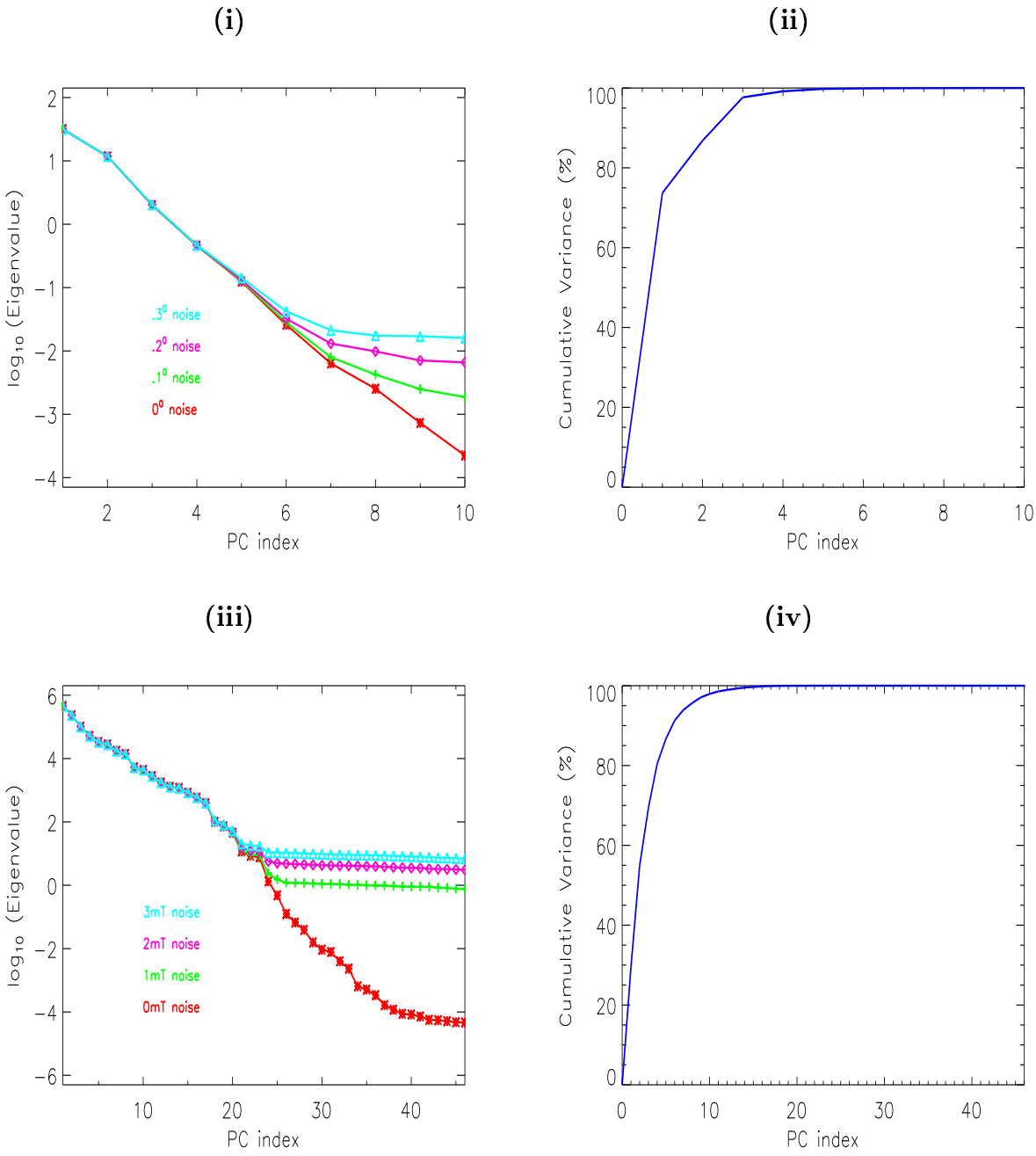

Figure 3.6: *Plots illustrating the PCA of the MSE and magnetic diagnostics. Fig.(i) shows the trend of log_{10} of the MSE PC eigenvalues for various noise levels while Fig.(ii) shows the culumative variance for the MSE PCs. Fig.(iii) and Fig.(iv) are the same illustrations but for the magnetic PCs*

accuracy, however there is a marked improvement with a full quadratic model:

$$y = a_0 + \underbrace{\sum_{i=1}^{N} a_i PC_i}_{Linear} + \underbrace{\sum_{i=1}^{N} b_i PC_i^2}_{Quadratic} + \underbrace{\sum_{i=1, j>i}^{N} c_{ij} PC_i PC_j}_{Bilinear}, \tag{3.21}$$

where y is the physical parameter of interest, a_0, a_i, b_j, c_{ij} are the regression coefficients, N is the number of PCs used in the model (as of yet undetermined) and PC are the principal components of the measurements. The small improvement associated with a cubic fit is offset by the increase in model size. For a quadratic model there are $(N+1)(N+2)/2!$ fitted parameters but this increases to $(N+1)(N+2)(N+3)/3!$ for a cubic model. This dramatic increase in fitted parameters decreases the number of degrees of freedom associated with the regression model based on a database with a limited number of degrees of freedom. For the optimum balance between accuracy and compactness a full quadratic model is chosen. The full quadratic model can be written more succinctly, if PC_0 is defined to be unity, as

$$y = \sum_{i=0}^{N} \sum_{j=i}^{N} a_{ij} PC_i PC_j, \tag{3.22}$$

For a more detailed discussion about model size see [8].

Selecting the Optimum Number of PCs Next the optimum number of PCs for the the FP regression model must be chosen. The PCA is a very useful tool in deciding the number of PCs needed to create the full quadratic set of predictors. Figure 3.6 **(i)** and **(iii)** shows the trend of log_{10} of each PC eigenvalue with increasing amount of noise added to the measurements for MSE and magnetics signals. It is obvious from the 'flattening' of the log_{10} eigenvalue plots, that as the eigenvalues become small the PCs become 'drowned out' by the random noise added to the measurements. In the MSE plot, for a noise level of $.2^o$ a distinct deviation of the PCs is seen after the 5^{th} PC and flattening occurs after the 7^{th} PC for the larger noise levels. Similarly in the magnetics plot with noise of 1mT a deviation in PCs occurs after the 20^{th} PC and a flattening occurs after 23^{rd} PC. This analysis whilst not definitive, shows that there is a definite cutoff point for the addition of PCs. The addition of PC below the 'noise cutoff level' would add no new predictive information to the model and would be detrimental to the stability of the model.

It is now necessary to present FP regression results and therefore it is necessary to introduce additional statistical 'jargon' which will be used to quantify the regression

results. For a given variable with spread σ, the sum of square error (SSE) for a model fitted over n observations with p fitted parameters is defined to be the sum of squared differences between the actual and recovered values. Then the adjusted root mean square error $RMSE = \sqrt{SSE/(n-p)}$ and the adjusted coefficient of multiple correlation $R^2 = 1 - RMSE^2/\sigma^2$. It is necessary to adjust the RMSE and R^2 values to take into account the degrees of freedom lost p in calculating the regression model The percentage error % error is defined as $100 \times (RMSE/\sigma)$ or equivalently $100 \times \sqrt{1-R^2}$. The physically relevant quantity is the RMSE but for statistical purposes the % error is important as the goodness of fit of the model is based on the amount of spread of the recovery parameter explained by the model.

The SSE of the model is a good measure of accuracy of the model to the fitted data, but suffers from the danger that the tested data is the same data that is used to fit the model in the first place, thus the result will be biased.

Test and Training Datasets As stated in Chapter 2, to gain an accurate representation of model fit, it is necessary to break the database into a test and training set and use the RMSE of the test dataset as the basis for determining model accuracy. There are many different methods of doing this, but for the purpose of FPJ it was decided to use the method of cross-validation [32]. The database was partitioned in 6 equal sized sections[5]. The FP model was regressed against 5 of the sections (training set) of the database and the regression results were tested against the remaining section of the database. This procedure was repeated for all the possible choices of the test dataset. The RMSE for each iteration was calculated. Note as the number of degrees of freedom in the test dataset is equal to the number of observation n_{test}; i.e. there is no need to adjust the RMSE, thus the $RMSE = \sqrt{SSE/(n_{test})}$ and corresponding quantities follow suit.

Determination of the Number of Magnetic PCs Initially only regressions with magnetic based PCs were performed, with an experimentally relevant added noise level of $1mT$. It is possible to accurately recover the outer ι profile with magnetics only, although it is difficult to determine exactly how far into the plasma the magnetic measurements can accurately determine the ι profile. The region $(0.80\rho_{mid} \rightarrow 0.95\rho_{mod})$ was used to

[5]The partitioning into 6 sections was an quasi-arbitrary decision based on the size of the model and size of the database.

test different regression model sizes with the aim of choosing the optimum number of magnetic PCs. The results are shown Fig. 3.7, where the % error in recovering ι at 4 fixed ρ_{mid} positions towards the edge of the plasma is plotted against increasing numbers of PCs. Both the % error from test and training cases are given along with the standard deviation of the % error of the test case. In each case there is a general trend that adding magnetic PCs to the regression model decreases the % error for the biased training case, but there is a definite local minimum associated with the test case's % error. For both Figs. 3.7**(iii),(iv)** the local minimum is centred at the 20^{th} PC while in Figs. 3.7**(i),(ii)** the local minimum appears closer to the 25^{th} PC. It was decided to take only 20 magnetic PCs for the final FPJ model as the improvement in recovering ι at the positions ρ_{mid}(0.80 and 0.85) with more than 20 PCs is offset by the increase in % error in the ι recovery at the outer positions ρ_{mid}(0.90 and 0.95). A 3D representation of the variation of test dataset % error of ι along ρ_{mid} due to increasing number of magnetic PCs added to the FP model is given in Fig. 3.8 , which highlights the global minimum in the recovery of the ι profile along the 20^{th} PC axis. The ι recoveries in Fig. 3.8 are presented over the co ordinates $1 - \rho_{mid}$ to better illustrate the global minimum.

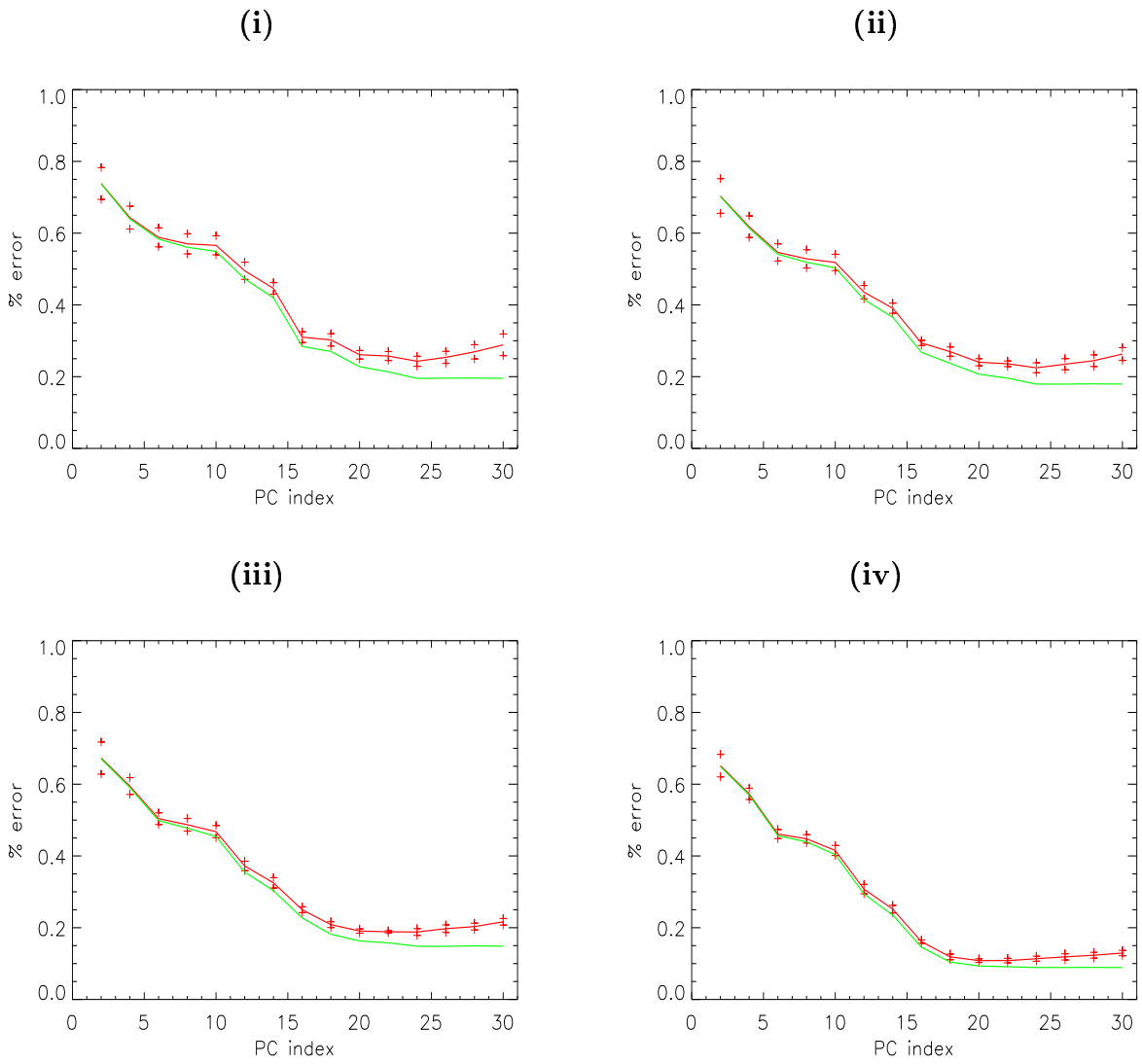

Figure 3.7: *Variation of the training and test % error (including the standard deviation of the test % error +) in the recovery of the outer ι profile with increasing number of magnetic signal PCs:* **(i)** *0.80 ρ_{mid},* **(ii)** *0.85 ρ_{mid},* **(iii)** *0.90 ρ_{mid},* **(iv)** *0.95 ρ_{mid}*

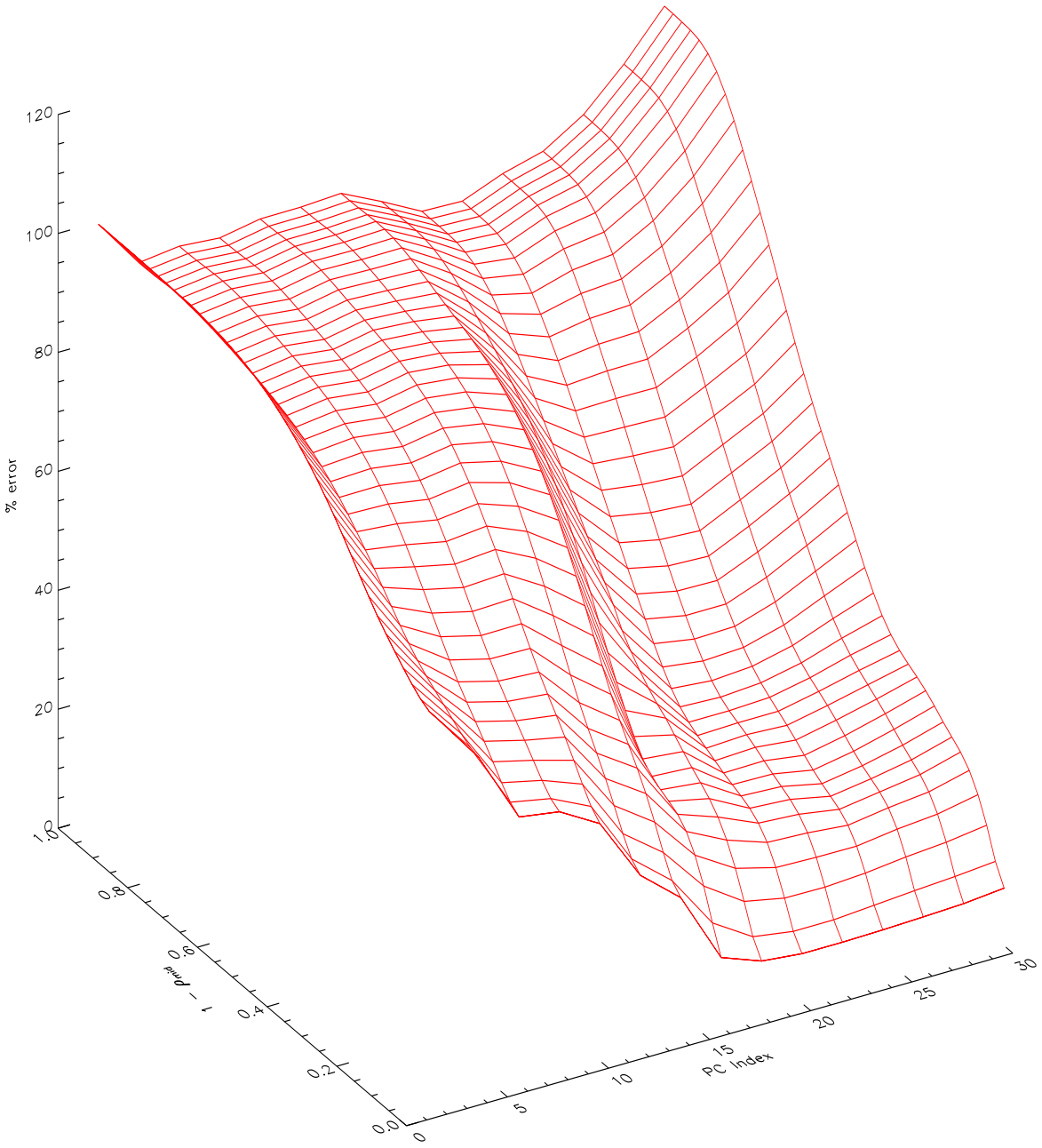

Figure 3.8: *3-D illustration of the variation of the test dataset % error of ι regression along ρ_{mid} due to increasing number of magnetic PCs added to the FP model. Grid lines are plotted for even PC indices from 2 to 30.*

Determination of the Number of MSE PCs Initially the MSE PCs were then added into the original regressions model (20 magnetic PCs) in a stepwise manner. It should be noted that with the inclusion of the MSE PCs valid regressions results now encompass the entire profile and not just the outer region. The results for the joint magnetic and MSE regressions are shown in Fig. 3.9, which is an identical representation to Fig. 3.7 differing only in that the regressions are for the regions $\rho_{mid}(0, .25, .50, .75, .95)$. From Fig. 3.9**(i),(ii),(iii)**,$\rho_{mid}(0.0 \rightarrow 0.5)$, the local minimum appears closer to the 25^{th} PC, which is equivalent to having 5 out of a possible 10 MSE PCs in the FPJ model. This region spans $\rho_{mid}(0 \rightarrow .5)$ which is the region of associated most with the MSE channels. For Figs. 3.9**(iv),(v)**,$\rho_{mid}(0.75 \rightarrow 0.95)$, the local minimum appears with smaller numbers of PCs. This is due to the limited range of the MSE channels along the ρ_{mid} axis where the addition of MSE PCs does not add any more useful information for the recovery of the t profile in this region. The t recovery in this outer region does not suffer much from the addition of 5 MSE PC so for the FPJ model it was decided to use 5 MSE PCs. A 3D representation of the variation of test dataset % error of t along ρ_{mid} due to increasing number of MSE PCs added to the FP model is given in Fig. 3.10, which highlights the local minimum in the recovery of the t profile along the 25^{th} PC axis. The t recoveries in Fig. 3.10 are presented over the co ordinates $1 - \rho_{mid}$ to better illustrate the global minimum.

To summarise, 20 magnetic PCs and 5 MSE PCs were chosen to form the basis of the quadratic set of predictors in Eqn. 3.22.

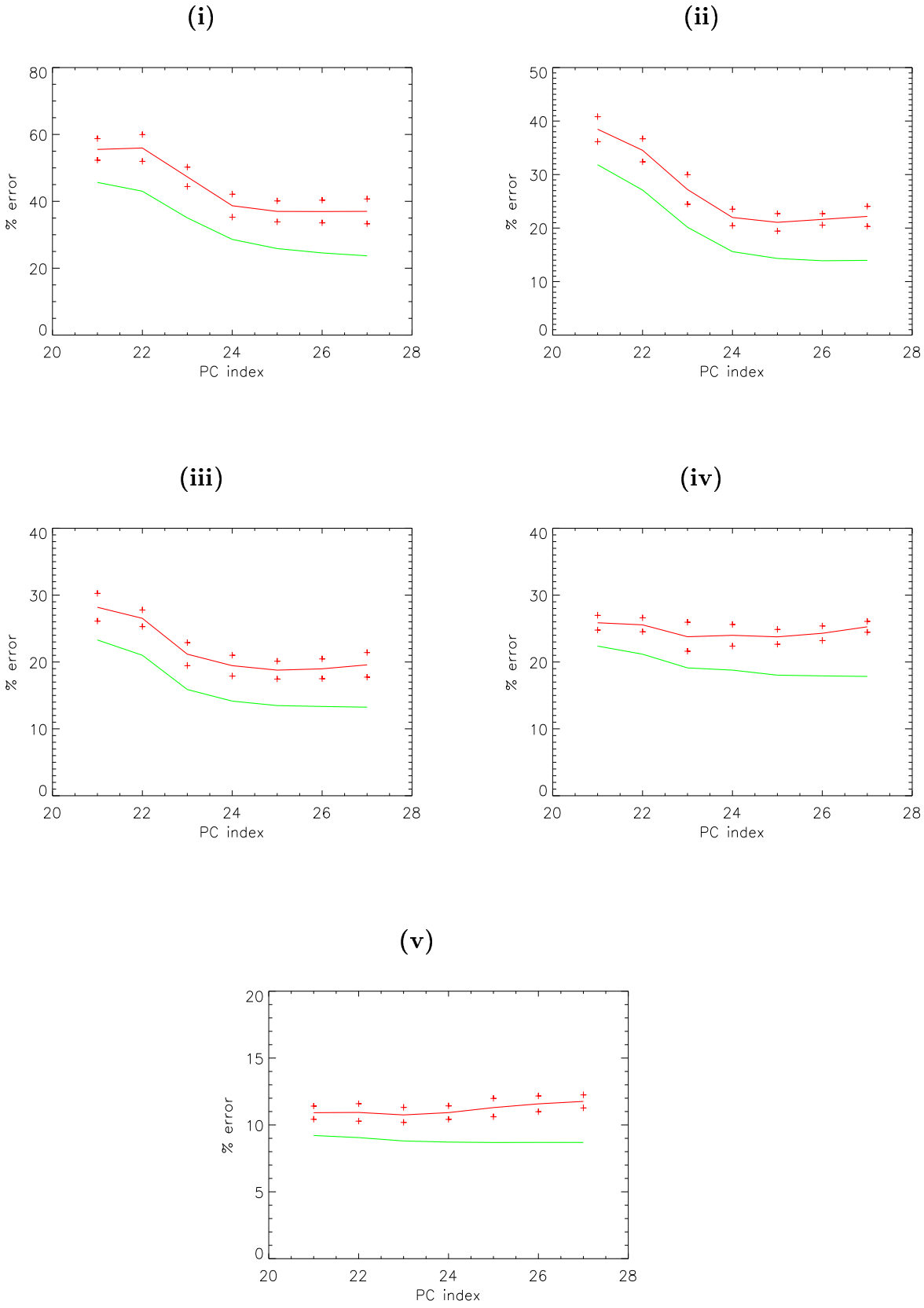

Figure 3.9: *Variation of the training and test % error (including the standard deviation of the test % error +) of the recovery of the τ profile with increasing number of MSE signal PCs:* **(i)** *0.0 ρ_{mid},* **(ii)** *0.25 ρ_{mid},* **(iii)** *0.50 ρ_{mid},* **(iv)** *0.75 ρ_{mid} ,* **(iv)** *0.95 ρ_{mid}.*

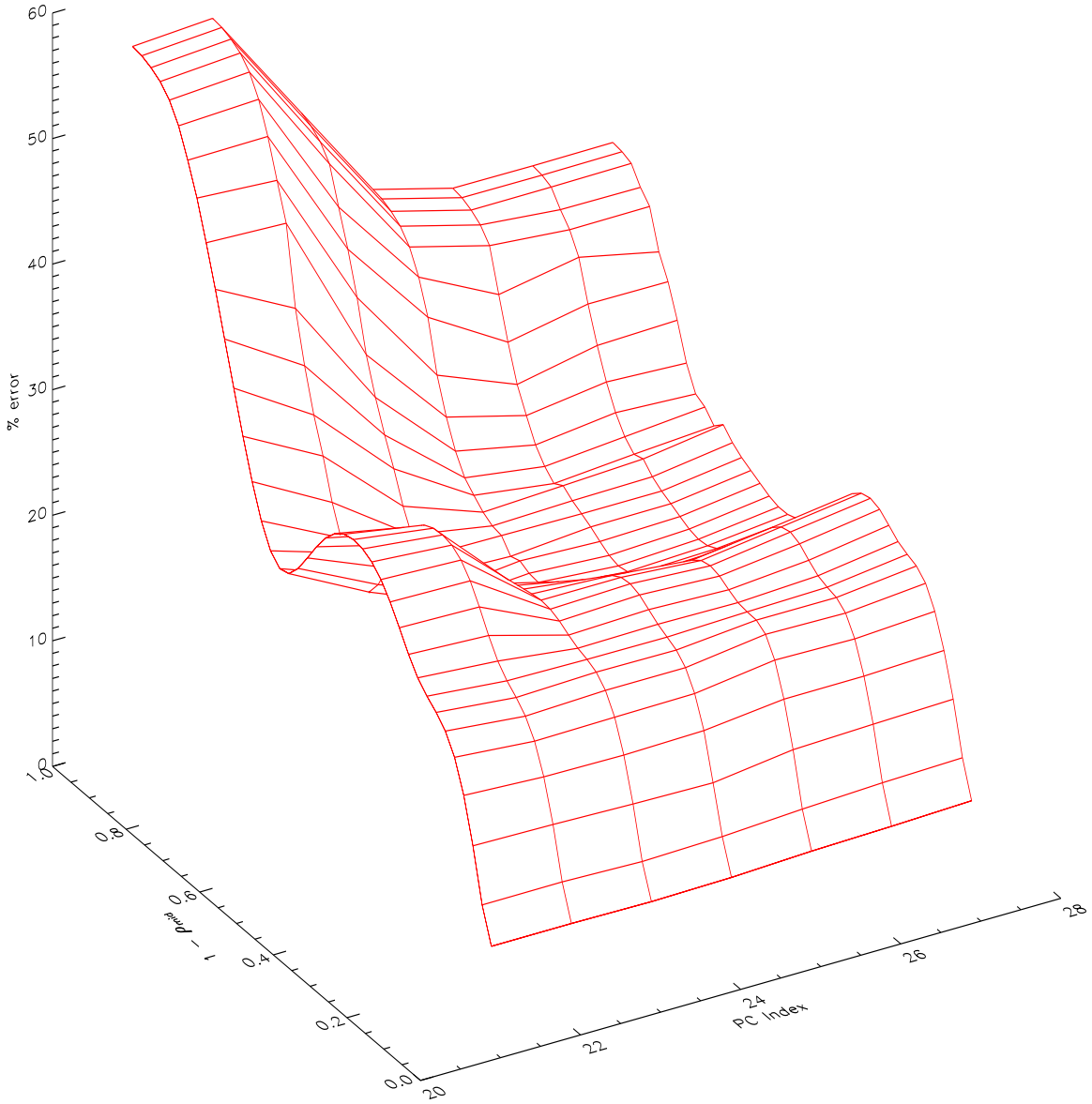

Figure 3.10: *3-D illustration of the variation of test dataset % error of* t *regression along* ρ_{mid} *due to increasing number of MSE PCs added to the FP model. Grid lines are plotted for PC indices from 21 to 27, indicating the incrementation of MSE PCs to the FP model.*

Preliminary Analysis Reviewed: Prior to the construction of the FPJ model certain assumptions were made, specifically the following:

- It is more correct to recover the q-profile via an ι regression and inverting the answer rather than a direct q-profile regression.

- It is better to recover the ι profile on ρ_{mid} co-ordinates rather than on ρ_ψ co-ordinates.

- The dependence of the ι recovery accuracy on ϵ is negligible when it is recovered over ρ_{mid} co-ordinates.

Now that the FPJ regression model is decided, it is possible to test these assumptions.

In Fig. 3.11**(i)**, **(iii)** the % error of the test and training cases for an ι-profile and a q-profile regression over ρ_{mid} co-ordinates are respectively plotted. From inspection it is obvious that the ι profile is the correct choice as for every single point plotted the ι profile is better recovered than the q-profile. In Fig. 3.11**(i)**, **(ii)** the % error of the test and training cases for ι-profile regressions over ρ_{mid} and ρ_ψ co-ordinates respectively are plotted. Also shown is the spread of the test case's % errors. These graphs illustrate the advantage of recovering the ι-profile on ρ_{mid} co-ordinates rather than on ρ_ψ co-ordinates.

It is not possible to compare both profiles directly as ρ_{mid} and ρ_ψ are different co-ordinate systems however they are both defined along the magnetic axis so it is possible compare the trend of each graph if not the positions. Both graphs exhibits the same general trend in that the maximum % error is at the centre of the plasma, where towards the centre of the plasma the error associated with the MSE signal approaches or can be greater than the MSE signal itself. The % error then decreases monotonically to a local minimum (due to the MSE channels information) then rises (due to the limited radial coverage of the MSE channels) and finally the % error decreases to a global minimum at the very edge of the plasma, as ι at the plasma edge ($\rho_{mid} = .95$) is essentially determined by the total plasma current. It is possible to compare the local minimums of the % error profiles where the local minimum of ρ_{mid} % error profile situated at $\rho_{mid} = .45$ and is 20% less than the equivalent local minimum of the ρ_ψ % error profile which is situated at $\rho_\psi = .7$. If the general shape of each profile is taken in account, the ρ_{mid} profile has a broad local minimum while the ρ_ψ has a very localised minimum. Although this is not

$\epsilon\rho_{mid}$	ϵ_{Mean}	ϵ_{Spread}	ϵ_{Min}	ϵ_{Max}	$\delta\epsilon$	$Spread/Mean$
0.00	0.000	0.000	0.000	0.000	0.00	0.00
0.25	0.088	0.011	0.065	0.146	0.003	12.5
0.50	0.179	0.020	0.133	0.291	0.004	11.2
0.75	0.279	0.028	0.209	0.414	0.003	10.0
0.95	0.384	0.035	0.291	0.528	0.004	11.0

Table 3.3: *Database summary statistics of ϵ variation for category 3 plasmas along ρ_{mid} co ordinates*

the only or even the most important reason to recover t on ρ_{mid} co ordinates rather than ρ_ϕ, it is more accurate to recover t over ρ_{mid}.

Finally the effect ϵ has on recovering t can be seen to be negligible in Fig. 3.11**(iv)** where the ϵ weighted and unweighted t regressions are plotted on ρ_{mid} co-ordinates. There are no major discrepancies between both profiles, except in the region where $< .15\rho_{mid}$. Thus weighting the regression w.r.t ϵ is not necessary. This can be explained that although the t recovery depends on ϵ the spread is small compared to the actual values of ϵ, shown in Table 3.3, ϵ can be treated as quasi-constant at least when it comes to recovering the t profile along ρ_{mid}.

3.4 Database Results

This section presents the results from the PCA based FPJ model.. The FPJ model consists of 25 PCs, 20 magnetic PCs and 5 MSE PCs, which form the basis for a full quadratic FPJ model, used to recover the t profile along ρ_{mid} co ordinates. The results from category 3 and category 4 plasmas are presented individually. First the basic regression results are shown, followed by an interpretation of the t errors associated with the FPJ regression and the intrinsic t errors associated with the MSE diagnostic. Finally a random sampling of t database profiles with the corresponding q-profile recoveries.

3.4.1 PCA Based FPJ Regression Results

Category 3 plasma database summary statistics, including mean, spread max and min values, for t profile along ρ_{mid} co ordinates are given in Tables 3.4, 3.5. Also presented are

(i) t Vs. ρ_{mid}

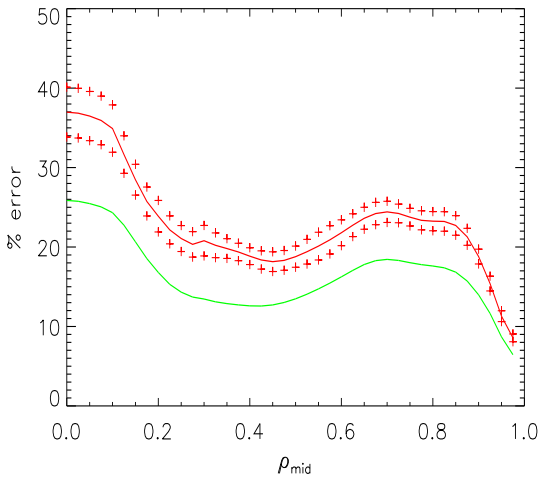

(ii) t Vs. ρ_{ψ}

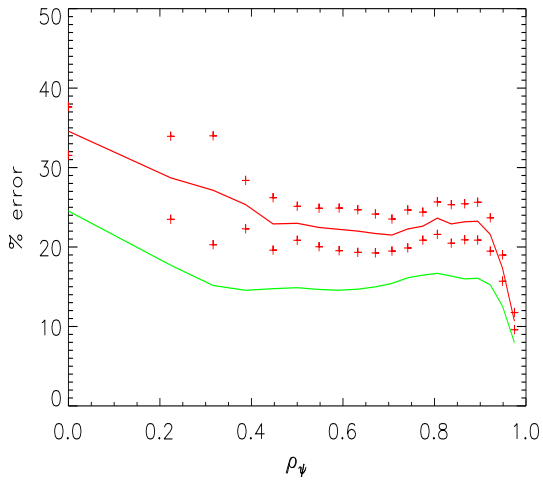

(iii) q Vs. ρ_{mid}

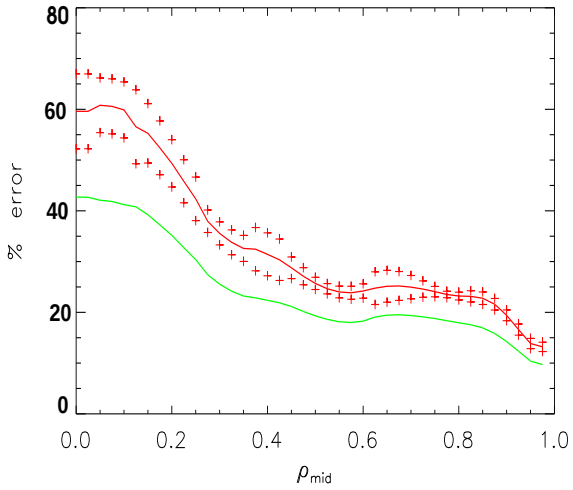

(iv) t Vs. ρ_{mid}(weighted w.r.t. ϵ)

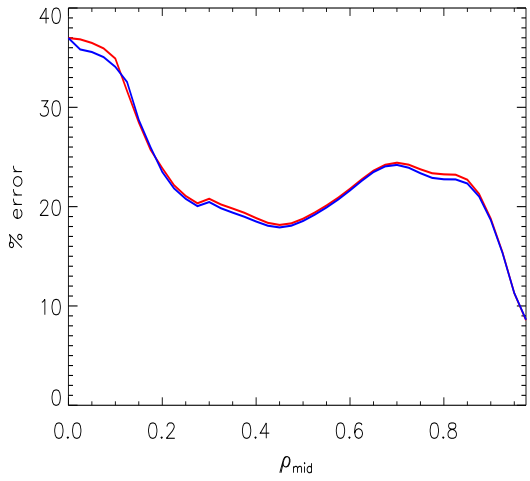

Figure 3.11: *(i) shows % error (test and training) associated with an t regression along ρ_{mid}, (ii) shows % error (test and training) associated with an t regression along ρ_{ψ}, (iii) shows % error (test and training) associated direct q regression along ρ_{ψ}, (iv) shows the test % error associated with a weighted and unweighted (w.r.t. ϵ) t regression along ρ_{mid},*

the results from the category 3 FPJ regression including the RMSE and the % recovery error. While the tables present an numerical representation of the FPJ recovery of ι, it was decided that a graphical representation of the data better illustrates the accuracy and the ι profile recovery trends and category 3 and 4 FPJ regression results are presented in Fig 3.12.

Fig. 3.12(i),(ii) illustrate the recovery of ι profile along ρ_{mod} for category 3 and 4 plasma, respectively. The database mean of the ι profile flanked by the RMSE of the FPJ recovery and the spread of the database demonstrates the accuracy of the recovery relative to spread of the database.

Fig. 3.12(iii),(iv) illustrates the trend of the % ι error recovery over the ρ_{mid} co ordinates for category 3 and 4 plasmas, respectively. It should be noted that Fig. 3.12(iii) is identical to the test % error presented in Fig. 3.11(i).

Fig. 3.12(v),(vi) presents the corresponding errors associated q-profile recoveries using the ι regressions. The q-value errors are the local maximum and minimum value of q $q_{\pm}$ associated with the recovered local ι. The q value errors are calculated using the formula

$$q_{\pm} = \frac{1}{\iota \mp \iota_{RMSE}}. \tag{3.23}$$

From Eqn. 3.23 it follows that the q errors are asymmetric around the database mean value of q, in particular q_{+} tends towards the maximum spread band of the database in the central region of the plasma.

Finally it is noteworthy that in all 3 plots, the trends in category 3 and 4 plasmas are identical.

ρ_{mid}	${}^{t}Mean$	${}^{t}Spread$	${}^{t}Min$	${}^{t}Max$	${}^{t}RMSE$	${}^{t}\%error$
0.00	1.463	1.051	0.187	8.188	0.362	34.4
0.025	1.463	1.050	0.186	8.182	0.361	34.4
0.050	1.460	1.048	0.183	8.162	0.356	34.0
0.075	1.453	1.042	0.183	8.121	0.349	33.5
0.100	1.446	1.033	0.182	8.047	0.336	32.5
0.125	1.438	1.020	0.181	7.926	0.298	29.2
0.150	1.429	0.999	0.180	7.733	0.262	26.2
0.175	1.418	0.972	0.181	7.450	0.231	23.8
0.200	1.404	0.938	0.187	7.059	0.208	22.2
0.225	1.388	0.897	0.199	6.575	0.186	20.7
0.250	1.367	0.850	0.214	6.068	0.168	19.8
0.275	1.341	0.798	0.230	5.650	0.154	19.3
0.300	1.310	0.743	0.235	5.152	0.148	19.9
0.325	1.276	0.688	0.234	4.615	0.134	19.5
0.350	1.238	0.634	0.233	4.071	0.122	19.2
0.375	1.198	0.583	0.234	3.576	0.110	18.9
0.400	1.157	0.534	0.236	3.351	0.099	18.5
0.425	1.115	0.490	0.239	3.160	0.089	18.2
0.450	1.073	0.448	0.245	3.036	0.081	18.1
0.475	1.032	0.410	0.252	2.898	0.074	18.0

Table 3.4: *Category 3 plasma database summary statistics and PCA FPJ recovery errors for the* t *profile along* ρ_{mid}

ρ_{mid}	t $Mean$	t $Spread$	t Min	t Max	t $RMSE$	t $\%error$
0.500	0.990	0.373	0.261	2.747	0.070	18.8
0.525	0.949	0.340	0.271	2.586	0.066	19.4
0.550	0.908	0.309	0.282	2.416	0.062	20.1
0.575	0.868	0.280	0.292	2.241	0.058	20.7
0.600	0.827	0.253	0.301	2.065	0.055	21.7
0.625	0.787	0.229	0.308	1.890	0.051	22.3
0.650	0.748	0.206	0.313	1.717	0.049	23.8
0.675	0.709	0.186	0.316	1.550	0.045	24.2
0.700	0.670	0.168	0.315	1.390	0.041	24.4
0.725	0.632	0.152	0.298	1.266	0.037	24.3
0.750	0.594	0.138	0.276	1.178	0.033	23.9
0.775	0.558	0.125	0.260	1.090	0.029	23.2
0.800	0.521	0.114	0.247	1.002	0.027	23.7
0.825	0.486	0.104	0.239	0.914	0.024	23.1
0.850	0.451	0.095	0.232	0.826	0.022	23.1
0.875	0.417	0.086	0.226	0.739	0.018	20.9
0.900	0.383	0.078	0.210	0.654	0.015	19.2
0.925	0.349	0.071	0.191	0.576	0.011	15.5
0.950	0.313	0.063	0.171	0.521	0.007	11.1

Table 3.5: *category 3 plasma database summary statistics and PCA FPJ recovery errors for the ι profile along ρ_{mid} (contd.)*

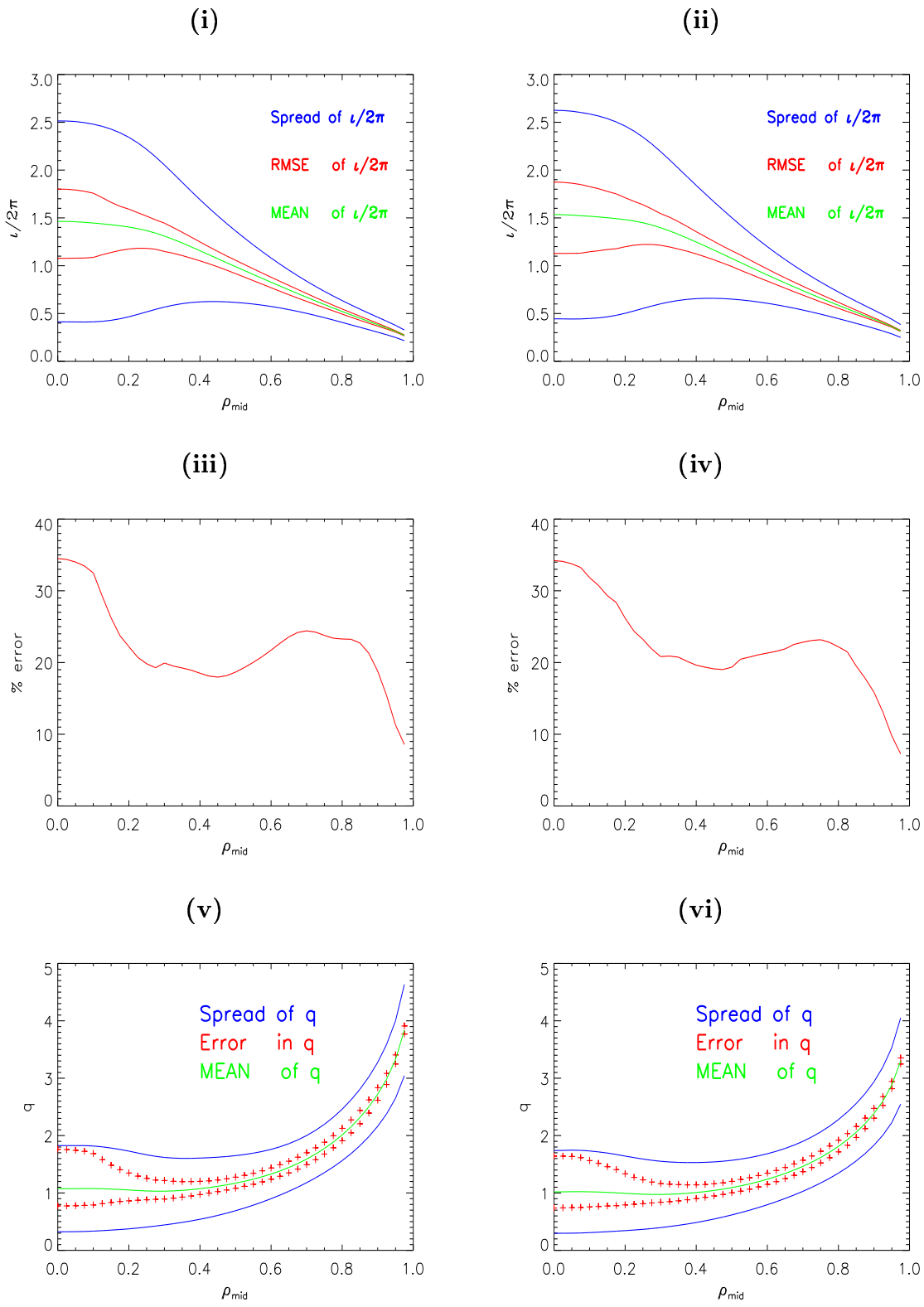

Figure 3.12: *(i) Illustrates the accuracy of the FPJ recovery of category 3 plasma's ι profile by comparing the RMSE and the spread of ι around its database mean value; (ii) illustrates the same for the category 4 plasmas; (iii) presents the ι recovery % error along ρ_{mid} for category 3 plasmas, (iv) presents the same for category 4 plasmas; (v) illustrates the accuracy of category 3 plasma's corresponding q-profile recovery; (vi) illustrates the q-profile recovery for category 4 plasmas and the asymmetry of the errors is noteworthy.*

3.4.2 Error Analysis

Intrinsic Database Errors There is a finite accuracy associated with any measurement of a physical quantity. The accuracy of the MSE diagnostic measurement of the magnetic pitch angle γ will be discussed and the limitations of recovering the ι,q-profile presented.

To date for demonstration purposes, the circular plasma approximation for q has been used. At this point we generalise for shaped flux contours. For the range of MSE channels ($0 < \rho_{mid} < 0.7$) flux contours will be assumed to be elliptical, which is a reasonable approximation.

The q profile can be expressed as the rate of change of the toroidal flux with the poloidal flux

$$q = \frac{d\Phi}{d\Psi}, \tag{3.24}$$

Locally this can be expressed as

$$q = \frac{|\nabla\phi|}{|\nabla\psi|}, \tag{3.25}$$

Similarly ι can be expressed as

$$\iota = \frac{|\nabla\psi|}{|\nabla\phi|} = \frac{2\pi R B_\theta}{\nabla\phi}. \tag{3.26}$$

At the position of the an MSE diagnostic channel in the FPJ database from Eqn. 3.26

$$\iota_{dbase} \propto |B_\theta| \propto \tan(\gamma_{dbase}), \tag{3.27}$$

where ι_{dbase} is the ι value of the plasma associated with the MSE angle γ_{meas}. If γ is a small angle, the approximation $tan(\gamma) \approx \gamma$ can be made.

From this it follows that

$$\iota_{dbase} \propto \gamma_{dbase}, \tag{3.28}$$

There is an experimental uncertainty associated with γ_{dbase} where γ_{dbase} can be described as $|\gamma_{true}|$ plus or minus the error associated with the MSE measurement $\delta\gamma$

$$\gamma_{dbase} = |\gamma_{true}| \pm \delta\gamma, \tag{3.29}$$

For the FPJ database $\delta\gamma$ is $\pm 0.2^o$. It is not possible to calculate γ_{true} but it is possible to calculate the maximum and minimum γ_{dbase} where

$$\gamma_{max,min} = \gamma_{dbase} \pm 0.2^o. \tag{3.30}$$

Assuming that the small change in poloidal field results in a negligible change in topology of the plasma flux surfaces and using Eqn. 3.28 it follows that

$$\frac{t_{\,dbase}}{t_{\,max,min}} = \frac{\gamma_{dbase}}{\gamma_{dbase} \pm 0.2^o}. \tag{3.31}$$

Thus the maximum and minimum t associated with the noisy MSE measurements are given by

$$t_{\,max} = t_{\,dbase}.\frac{|\gamma_{dbase}| + \delta\gamma}{|\gamma_{dbase}|} \quad , \quad t_{\,min} = t_{\,dbase}.\frac{|\gamma_{dbase}| - \delta\gamma}{|\gamma_{dbase}|} \tag{3.32}$$

As $q = 1/t$ the maximum and minimum values of q associated with the noisy MSE measurements are given by

$$q_{max} = q_{dbase}.\frac{|\gamma_{dbase}|}{|\gamma_{dbase}| - \delta\gamma}. \quad , \quad q_{min} = q_{dbase}.\frac{|\gamma_{dbase}|}{|\gamma_{dbase}| + \delta\gamma} \tag{3.33}$$

In the following random sampling of database FPJ recoveries the maximum and minimum local t, q values at each MSE channel is given as a reference for the accuracy of the FPJ t recoveries.

FPJ Model confidence Intervals The FPJ model is based on an OLS regression of the t values at fixed ρ_{mid} positions. The 95% confidence interval is $\pm$ twice the root mean square error $\triangle t$ associated with the regression. The test dataset $\triangle t$ is taken to form the confidence interval as this value is calculated independently of the dataset used to build the FPJ model.

Thus at each fixed ρ_{mid} position the 95% confidence interval is given by

$$t_{\,\pm} = t \pm 2\triangle t\,. \tag{3.34}$$

For an t regression, the corresponding $q_\pm$ is

$$q_\pm = \frac{1}{t \mp 2\triangle t}. \tag{3.35}$$

3.4.3 PCA FPJ database ι,q Profile Recoveries

A sample selection of database ι,q profile recoveries for category 3 and 4 plasmas are presented in Figs. 3.13- 3.16. These plots are identical in structure, a black line illustrates the database profile, with dark blue crosses indicating the position and value of the intrinsic database profile error associated with the MSE measurements. The FPJ profile recovery is indicated by 3 light blue profiles, signifying the recovery and the 95% confidence bands.

The eight sample database equilibria illustrate the dependence of the FPJ recovery on the position of the MSE channels relative to the plasma. The ρ_{mid} range of the MSE channels for the 8 equilibria is from $0 \rightarrow .5$ to $0 \rightarrow .75$, which is quite a significant difference. The narrowing of the MSE channel ρ_{mid} range tends to be due to the position of the centre of the plasma varying relative to the MSE channel resulting in channels to the low and high field sides of the plasma. As previously stated this is detrimental to the recovery of the ι, q profile towards the edge of the plasma, but not yet in the vicinity of the magnetic diagnostic signals. It has been shown previously that the % error in recovering ι increases in the region between the MSE channels and the edge of the plasma.

From both the intrinsic database errors and the FPJ confidence bands, sampling clearly shows that towards the centre of the plasma the errors in recovering ι, q profiles increase due to lack of information.

The bottom lefthand plots in Figs. 3.15, 3.16 show that it is not possible to recover the profile features that occur between channels. There is a non central q_{min} associated with these plots but the reversed shear only occurs between channels 7 and 8 and thus cannot be recovered by the FPJ routine.

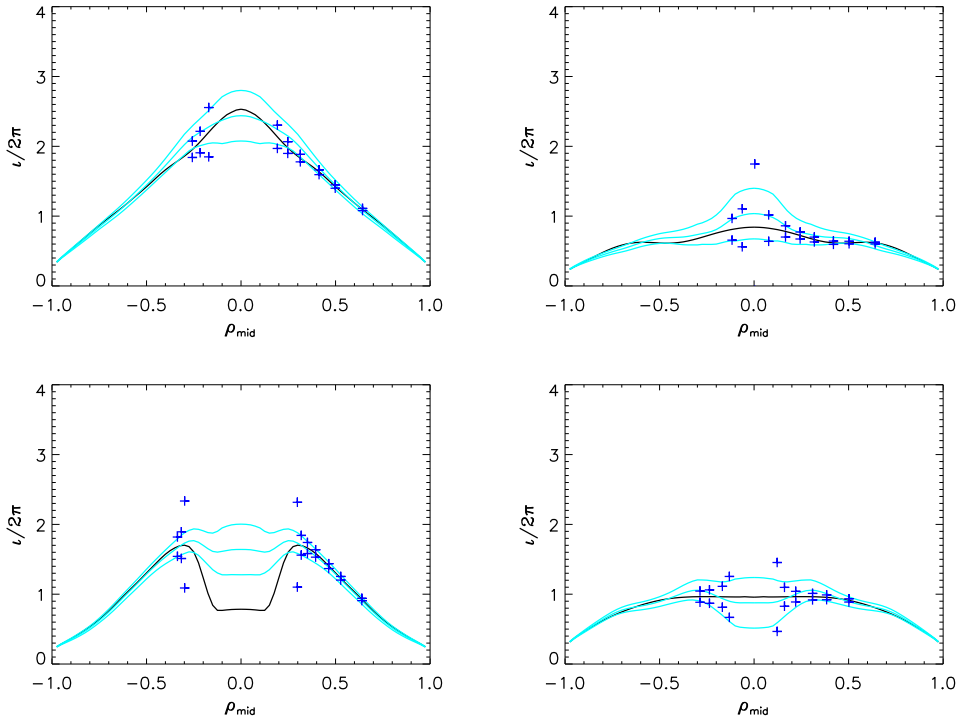

Figure 3.13: *Random sample of results for single null upper divertor plasma (category 3) database ι recoveries*

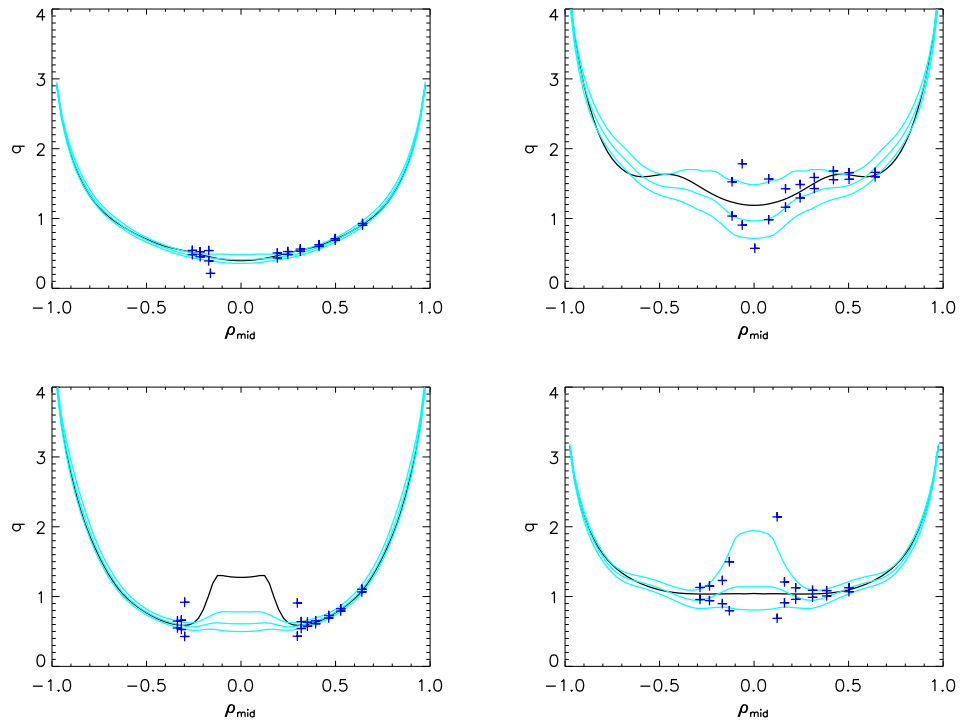

Figure 3.14: *Random sample of results for corresponding single null upper divertor plasma (category 3) database q recoveries*

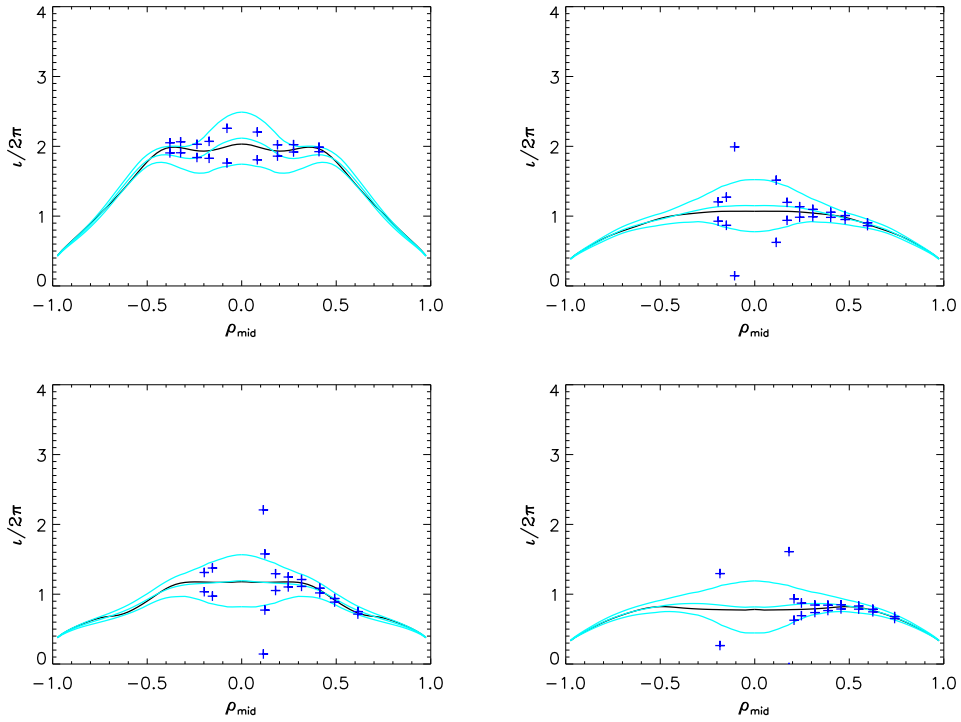

Figure 3.15: *Random sample of results for single null lower divertor (category 4) database ι recoveries*

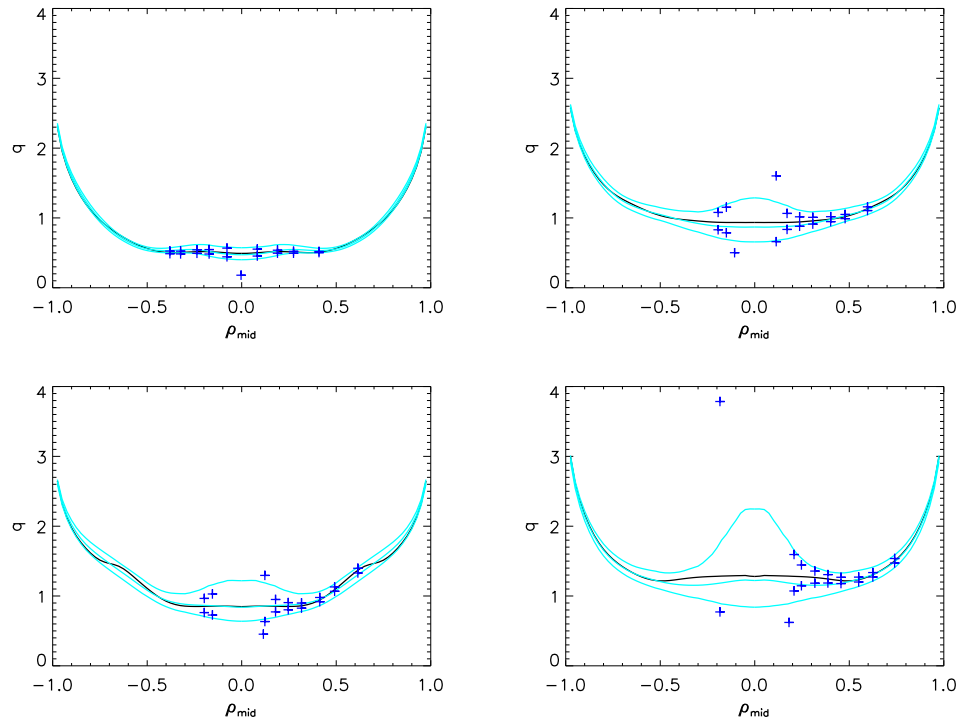

Figure 3.16: *Random sample of results for corresponding single null lower divertor (category 4) database q recoveries*

Chapter 4

AUG FPJ Experimental Results

4.1 Introduction

In this chapter, the experimental recovery of AUG q-profiles by CLISTE and FPJ methods is discussed and the relevant error analysis is presented. Different AUG experimental scenarios are discussed and finally experimental data from various AUG discharge scenarios is used to compare the recoverability of the q-profile using both methods.

4.2 CLISTE Recovery of Experimental ι, q Profiles

The CLISTE interpretive equilibrium code iteratively solves the Grad-Shafranov equation and is regularised by source profiles under the constraint of a least squares fit from a set of experimental data. A detailed description is given in Appendix C.

4.2.1 CLISTE Error Analysis

Using the same starting point, the CLISTE error bars [33] can be described as an extension to the intrinsic MSE error analysis associated with the database analysis in section 3.4.2

At the position of the MSE diagnostic channel, from Eqn. 3.26 it follows that

$$\iota_{exp} \propto B_\theta, \tag{4.1}$$

and Eqn. 3.9 stated that

$$tan(\gamma_{exp}) = \frac{A_1 B_r + A_2 B_\phi + A_3 B_z + A_4 E_r + A_5 E_z}{A_6 B_r + A_7 B_\phi + A_8 B_z + A_9 E_r},$$

where ι_{exp} is the ι value of the plasma associated with the small MSE angle γ_{exp}.

Using the interpretive equilibrium code CLISTE ι_{fit} is found with the corresponding $tan(\gamma_{fit})$ and $B_{\theta,fit}$ at each channel location. It is assumed that that the flux topology is consistent between the model and the experiment, i.e. $|\nabla\phi|$ is constant. The local values of B_θ at the MSE channel locations are varied linearly until it reaches a value $B_{\theta,exp}$ where $tan(\gamma_{fit})$ is equal to $tan(\gamma_{exp})$. It follows that the experimental value of q q_{exp} is given by

$$q_{exp} = q_{fit}.\frac{B_{\theta,fit}}{B_{\theta,exp}}. \tag{4.2}$$

Analogous to eqn 3.30, the errors associated with γ_{meas} can be described as

$$\gamma_{max,min} = |\gamma_{meas}| \pm \delta\gamma \tag{4.3}$$

Following the reasoning in section 3.4.2 the experimental uncertainty associated with ι_{exp} can be expressed as

$$\iota_{max} = \iota_{exp}.\frac{|\gamma_{meas}| + \delta\gamma}{|\gamma_{meas}|} \quad , \quad \iota_{min} = \iota_{exp}.\frac{|\gamma_{meas}| - \delta\gamma}{|\gamma_{meas}|}. \tag{4.4}$$

Up to this point it was assumed that the change in flux topology due to the change in poloidal flux was negligible. For database equilibria the flux surfaces were known exactly, but for the CLISTE recovered equilibria the flux surfaces are 'fitted' surfaces and thus have an associated geometric uncertainty. For this reason the geometric error associated with $|\nabla\phi|$ was estimated and the resulting error associated with the recovery of ι at each MSE channel location was calculated.

The typical uncertainties associated with FPG (FP using only magnetic diagnostic signals) recovery of flux surface topology were errors of 5mm at boundary to 10mm at centre in the R co ordinate and 5mm in the Z co ordinate of the centroid of the flux surface passing through the MSE channel location, also the error in κ was given by a function which varies from 0.015 at the boundary to 0.1 at the magnetic axis.

Recalling equation 3.26

$$\iota = \frac{|\nabla\psi|}{|\nabla\phi|} = \frac{2\pi R B_\theta}{\nabla\phi}$$

The toroidal flux ϕ enclosed by the surface passing through an MSE channel location is given by

$$\phi = < B_\phi > .\pi.a(\psi).b(\psi), \tag{4.5}$$

where

$$< B_\phi >= B_0 R_0 . < 1/R >, \tag{4.6}$$

is the area averaged toroidal field in the ellipse with minor flux-dependent radii $a(\psi), b(\psi)$. The expression for $< 1/R >$ over the flux dependent ellipse centroid $(R_c(\psi), Z_c(\psi))$ is

$$< 1/R >= \left(\frac{2.R_c}{a^2}\right)\left(1 - \sqrt{1 - \frac{a^2}{{R_c}^2}}\right). \tag{4.7}$$

The flux dependent minor radius $a(\psi)$ can be given in Cartesian co ordinates position of the MSE channel (R_{mse}, Z_{mse})

$$a(\psi) = \sqrt{(R_{mse} - R_c)^2 + \frac{(Z_{mse} - Z_c)^2}{\kappa^2}} \tag{4.8}$$

where κ is the elongation of the ellipse.

Using the ellipse relationship $\kappa = b/a$ Eqn. 4.5 can be rewritten as

$$\phi =< B_\phi > .\pi.\kappa.a(\psi)^2. \tag{4.9}$$

Combining Eqns. 4.6 - 4.9 ϕ can be expressed as

$$\phi = 2.\pi.F_o.\kappa\left(R_c - \sqrt{R_c^2 - (R_{mse} - R_c)^2 - \frac{(Z_{mse} - Z_c)^2}{\kappa^2}}\right), \tag{4.10}$$

where $F_0 = B_0.R_0$ is a constant quantity, the vacuum magnetic magnetic field times the radial position of the plasma centre.

Using Mathematica[34] $|\nabla\phi|$ can be expressed as

$$|\nabla\phi| = \frac{2.\pi.F_o.\kappa}{R_c}\sqrt{\frac{(R_{mse}(1 - D') + R_c(D'.\sqrt{1 - \epsilon^2} - 1))^2 + \frac{(Z_{mse\epsilon} - Z_c)^2}{\kappa^4}}{1 - \epsilon^2}}, \tag{4.11}$$

where $D' = dD/dR$, D is the flux dependent Shafranov shift $(R_c - R_o)$ and $\epsilon = a/R_c$ is the inverse aspect of the ellipse through (R_{mse}, Z_{mse}). Initial tests showed that $|\nabla\phi|$ as calculated here differs by an average of $< 10\%$ over the 10 MSE channels when compared to $|\nabla\phi| = q \times |\nabla\psi|$

The perturbation in $|\nabla\phi|$ is calculated using finite differencing

$$\begin{aligned} d|\nabla\phi_R| &= |\nabla\phi(R + dR)| - |\nabla\phi(R)| \\ d|\nabla\phi_Z| &= |\nabla\phi(Z + dZ)| - |\nabla\phi(Z)| \end{aligned} \tag{4.12}$$

$$d|\nabla\phi_\kappa| = |\nabla\phi(\kappa + d\kappa)| - |\nabla\phi(\kappa)|$$

Using the relationship

$$\frac{d(q_{R,Z,\kappa})}{q_{fit}} = \frac{d|\nabla\phi_{R,Z,\kappa}|}{|\nabla\phi_{fit}|} \tag{4.13}$$

the error in CLISTE q fit q_{fit} due to uncertainties in R, Z, κ $d(q_{R,Z,\kappa})$ can be found Assuming the individual geometric errors are uncorrelated the error can be added in quadrature and the total error due to geometric uncertainties is given by

$$d(q_{geo}) = \sqrt{d(q_R)^2 + d(q_Z)^2 + d(q_\kappa)^2}. \tag{4.14}$$

Thus the total experimental error in ι due to CLISTE fit is given by combining eqn 4.4 with the geometric error, where it is assumed that they are perfectly correlated.

Finally the total CLISTE experimental error in q is given by

$$q_{min}(MSE + geo) = \frac{1}{\iota_{\,max,mse}} - d(q_{geo}) \tag{4.15}$$

$$q_{max}(MSE + geo) = \frac{1}{\iota_{\,min,mse}} + d(\iota_{\,geo}) \tag{4.16}$$

4.3 FPJ Recovery of Experimental ι, q Profiles

In this section the recovery of AUG q-profiles using FPJ is outlined. The FPJ database is restricted to a constant I_p of 1MA and $\mathbf{B}_\phi$ of 2.5T, while experimental discharge have variable I_p and $\mathbf{B}_\phi$. It is important to scale the experimental diagnostic signals (magnetics and $tan(\gamma')$) to correspond with equivalent database signals of constant I_p and $\mathbf{B}_\phi$.

The magnetic diagnostic signals (mag_{exp}) scale with I_p only. Thus to scale the experimental diagnostic signals to an I_p of 1MA, the signals must be multiplied by the reciprocal of the $I_p(exp)$

$$mag_{exp} \times \frac{1}{\mathbf{I_p}(exp)} = mag_{dbase} \tag{4.17}$$

The scaling of I_p and $\mathbf{B}_\phi$ variable MSE signals to create constant I_p and $\mathbf{B}_\phi$ MSE signals $tan(\gamma\prime)$ was discussed in section 3.2.4 and is given by Eqn.3.13

$$tan(\gamma\prime) = \left[tan(\gamma_{exp}) - \frac{\mathbf{A_2}}{\mathbf{A_7}}\right] \times \frac{\mathbf{B}_\phi}{2.5} \times \frac{1}{I_p}.$$

Using Eqn. 3.22 the database equivalent experimental t_{dbase} is recovered. To recover AUG t_{fpj}, t_{dbase} must be unscaled using

$$t_{fpj} = t_{dbase} \times \frac{2.5}{\mathbf{B}_\phi} \times \frac{I_p}{1}. \tag{4.18}$$

Finally the AUG q value q_{fpj} is given by

$$q_{fpj} = \frac{1}{t_{fpj}} \tag{4.19}$$

4.3.1 FPJ Error Analysis

The FPJ error $\triangle t_{fpj}$ is given by scaling the FPJ database error $\triangle t_{dbase}$ identical to how t_{dbase} was scaled in Eqn. 4.18 and is given by

$$\triangle t_{fpj} = \triangle t_{dbase} \times \frac{2.5}{\mathbf{B}_\phi} \times \frac{I_p}{1} \tag{4.20}$$

From 3.35 for an t_{fpj} recovery, the corresponding $\triangle q_{fpj}(\pm)$ is given by

$$\triangle q_{fpj}(\pm) = \frac{1}{t \mp 2.\triangle t_{fpj}}. \tag{4.21}$$

4.4 AUG Operating Scenarios

It is possible for the AUG experiment to operate in different experimental scenarios. In this section the various mode of operation will be described.

4.4.1 Ohmic Plasma

At the beginning of each AUG discharge, prior to auxiliary heating of the plasma, the induced toroidal plasma current not only generates the confining poloidal magnetic field, it also resistively heats the plasma with an ohmic power of $(I_p^2 R)$. As the Spitzer resistivity $\eta \propto T_e^{-3/2}$, the ohmic heating of the plasma is limited to relatively low temperatures [35].

4.4.2 L-mode Plasma

Auxiliary heating of AUG plasmas can be either by neutral beam injection NBI or radio frequency waves both of which increase the plasma energy content. The L-mode describes the "low" confinement mode of operation. It was found that although the plasma energy

content is increased by auxiliary heating, the confinement time τ_E was found to degrade with increased heating power. The degradation of τ_E is due to higher levels of turbulence which leads to enhanced radial transport perpendicular to the magnetic field lines. Analysis of a database of results from several tokamaks yielded a confinement scaling law ITER89-P [36], where along with many other factors τ_E depends on $P^{-0.5}$ where P is the applied heating power. Although the AUG experiment is designed to operate in H-mode, it is possible to operate in L-mode and although the L-mode by definition suffer from low confinement there is much reactor relevant physics associated with the L-mode; specifically internal transport barrier ITB physics.

4.4.3 H-mode

The H-mode [37] was discovered in the early eighties in ASDEX (the predecessor experiment to AUG), where τ_E was improved by a factor of 2 from previous L-mode operation. It was found that when sufficient power was applied to a divertor discharge an abrupt transition took place where the edge confinement was improved dramatically. This led to an edge pedestal in the temperature and density profile. The H-mode edge transport barrier is not fully understood, but it is generally accepted that the increased $E \times B$ shear suppresses the edge turbulence and decreases radial transport [38].

The appearance of edge localised modes ELMs is important to a fusion reactor. ELMs are a periodic instabilities associated with the H-mode where each burst of instability leads to reduction in density and temperature in the outer zone of the plasma. These bursts of energetic particles released from the plasma strike the experiment wall and over time can be detrimental to the integrality of the divertor.

A characteristic feature of the H-mode is the fall in the D_α signal. The D_α signal comes from the neutral deuterium entering the plasma and is a measure of the recycling of deuterium between the plasma and it immediate surroundings. The D_α signal shows characteristics spike-like bursts coinciding with ELM crashes.

4.4.4 Advanced Scenarios

An advanced scenario [39] can be defined as a scenario with improved confinement, measured by the H-factor, relative to the energy confinement scaling laws and good MHD

stability properties measured by the normalised beta β_N.

$$H = \frac{\tau_E}{\tau_{E,scaling}} \qquad \beta_N = \langle\beta\rangle \frac{aB}{I_p} \tag{4.22}$$

where $\langle\beta\rangle$ is the volume average of $2\mu_0 p/B^2$, a is the minor radius, B is the magnetic field, I_p is the plasma current and p is the plasma pressure.

For a scenario to be advanced, the product of $\beta_N H$ must be greater than that of the standard H-mode. Using the ITER89-P scaling [40] this would mean $\beta_N H \geq 6 - 7$. An advantage of a advanced scenario is the possibility of operation at reduced current by replacing a substantial fraction of the plasma current by the bootstrap current [41], which is necessary for long pulsed operation. The record steady state $\beta_N H$ value for ASDEX Upgrade is 7.2 while the record transient $\beta_N H$ value for ASDEX Upgrade is 11.5 [42].

Internal transport barrier: Internal transport barriers ITB scenarios are candidates for advanced scenarios. ITB scenarios are characterised by high confinement in the plasma core, where transport is reduced to almost neoclassical levels. The generally accepted model describing improved ITB confinement is that the associated low or negative magnetic shear associated with ITBs acts as a facilitator for $E \times B$ shear which suppresses turbulence in the plasma core. This regime requires low or negative magnetic shear $s =$ (r/q)(dq/dr). The associated off-axis peaking of the current profile allows stabilisation of high n MHD modes and q> 1 everywhere stabilises the sawtooth instabilities. With the addition of strong heating power and absence of these instabilities steep pressure profile are formed and central ion transport is reduced down to almost neoclassical levels.

Initially in AUG this regime was developed with an L-mode edge, either in limiter configuration or in single null upper divertor configuration where the unfavourable drift direction with respect to the X-point in single null upper divertor configuration allows a higher H-mode threshold. In AUG, strong auxiliary heating (usually NBI) takes place during the current ramp phase of the discharge and this results in low or negative s.

For AUG $H^{ITER89-P} = 3.3$ have been obtained in L-mode and β_N value of 4.0 [43].. Also the relationship between the ITB structure and the q-profile is being investigated in order to ascertain the influence the q-profile has on the ITB formation and sustainment [44]. A detailed description of ITBs is given in the review article [45]

Improved H-mode: In AUG a stationary advanced H-mode scenario with good confinement properties has been found and is referred to as an improved H-mode [46]. Initially the plasma is heated with neutral beams in the current ramp phase which slows down the current diffusion. Sometimes ITBs have been found in this L-mode prior to the transition to the H-mode, these ITBs are transiently found in the proceeding H-mode mode but maintaining these conditions in steady state have been unsuccessful. One conjecture for the disappearance of these ITBs is attributed to the ELM activity and density increase associated with the improved H-mode. With the retarded current diffusion the q = 1 surface appears later in the discharge compared to the standard H-mode and one of the features of an improved H-mode is the presence of fishbones instead of sawteeth activity. It has been found, with the exception of high beta poloidal discharges [47] which have a modest barrier, that in steady state improved H-mode AUG scenarios there are no ITB [48]. Here it was shown that the ion temperature profiles were found to be stiff and the improved H-mode follows the same scaling as the standard H-mode. The improvement of confinement was associated partly with the scaling of the line average density and partly obtained through density peaking appearing at low densities.

Results for AUG improved H-mode discharges are presented in [49] Typical results for an AUG discharge with triangularity δ of $0.17, q_{95} = 3.3, I_p = 1, B_\phi = 2.1$ are $n_e/n_{GW} = 0.4, \beta_{pol} = 1.4, \beta_N = 2.8, \beta_N H^{ITER89-P} = 6.5$, and $H_{98y2} = 1.4$. It should be noted that these are not record results for AUG, presently it is possible to increase δ of discharges from 0.17 to 0.42, which leads to improved confinement. These cases are not applicable to this work because, as previously stated, the MSE diagnostics is not working satisfactorily.

4.5 AUG q-Profile Recovery Results

4.5.1 Introduction

In this section AUG CLISTE and FPJ recovered q-profiles are presented. A sampling of AUG q-profile recoveries at various AUG discharge time-points will be presented to illustrate the FPJ and CLISTE recoverability of q-profiles in distinct discharge scenarios, at different times during a discharge and with variable,from discharge to discharge, I_p and $\mathbf{B}_\phi$.

The error bars associated an FPJ recovered AUG q-profile are tested to ascertain how many simulated experimental AUG equilibrium database q-profiles fit within the error bar limits. The various current density profiles associated with these database q-profiles are then presented to illustrate the different types of current density profiles that could be possible within FPJ recovery limits.

4.5.2 Selection of AUG q-Profile Recoveries

The general layout for all the AUG q-profile recovery representations is identical. The first figure illustrates the AUG q-profile recovery by the various methods. The FPJ recovery and 95% confidence bands are represented by three solid blue lines. The CLISTE recovery is indicated by the solid black line. q_{exp} at each of the 10 MSE channels is indicated by the green triangle, while the q_{exp} error bars are indicated by the vertical solid red lines.

The second figure associated with each individual AUG q-profile recovery shows the magnetic flux surfaces associated with the AUG plasma, where the green line signifies the last closed flux surface, and various plasma parameters.

As shown in section 4.2 the calculation of q_{exp} and the associated error bars are based on CLISTE estimated AUG equilibrium. It is important to note that while the error bars associated with q_{exp} take into account the CLISTE uncertainty associated with the geometric position of the flux surfaces, q_{exp} treats the CLISTE flux surface geometric as exact and thus q_{exp} is unavoidably biased toward the CLISTE recovery of the q-profile.

A notable trend evident in AUG q-profile recovery is that errors associated with each type of q-profile recovery, FPJ and CLISTE, balloon towards the centre of the plasma. The main reason for this is that $\mathbf{B}_\theta$ goes to zero towards the centre of the plasma, thus $tan(\gamma_{exp})$ goes to zero towards the centre and in this region the magnitude of

$\triangle$ $tan(\gamma_{exp})$ is comparable, and is possible to be greater than, the magnitude of $tan(\gamma_{exp})$ itself.

Another reason for this increase in the q-profile errors towards the centre of the plasma is due to the fixed geometry of the MSE channels. Depending on the position and shape of the plasma it is possible, and illustrated in some of the proceeding AUG discharge examples, that the centre of the plasma is distant from the MSE channels, thus little is known of the central q-profile and so the errors increase. This problem is indeed detrimental to the FPJ recovery as the FPJ recovery is based on a set of ι regressions over normalised plasma co ordinates. Thus for the part of the ι-profile towards the centre of the plasma the recoverability of ι by the FPJ regression suffers due to the equilibria in the simulated AUG FPJ database where the MSE channels do not span the central region of the plasma. This is appropriate for the AUG discharges where the MSE channels are distant from the centre of the plasma, but this leads to an exaggerated error in the FPJ recovery for the AUG discharges where the MSE channels are close to the centre of the plasma.

H-mode recoveries The first seven AUG discharges are H-mode discharges.

Fig. 4.1 shows the recovery of the q-profile for discharge 12055 after 2.1s with a I_p of 1.0 MA and $\mathbf{B}_\phi$ of 2.6T. At this time the discharges is in flattop, where I_p is fully ramped up. These values of I_p and $\mathbf{B}_\phi$ are typical values for AUG. The centre of the plasma is between the MSE channels 8 and 9 (where channel 1 is the outer most MSE channel). Fig. 4.1 indicates that q_{exp} errors are greatest for the channels 8-10 which are closest to the centre of the plasma. The FPJ confidence bands are widest in this region. The FPJ and CLISTE recoveries agree within FPJ confidence limits and for the most part are within q_{exp} error bars. From Fig. 4.1 it is also demonstrated that the FPJ and CLISTE recoveries of q_{95} agree and that the FPJ confidence bands are much tighter towards the edge of the plasma. As already stated the outer q-profile is readily recoverable by the magnetics only and is a well defined quantity. Fig. 4.2 is a cross section of AUG indicating the flux surface geometry for this discharge at this timepoint and lists some of the more important plasma parameters.

Fig. 4.3 shows the recovery of the q-profile of discharge 12077 after 1.5s with a I_p of 1.0 MA and $\mathbf{B}_\phi$ of 2.1T. The q-profiles for discharge 12055 and 12077 are very similar as both are in flattop. Again for discharge 12077 the FPJ, CLISTE are generally within q_{exp}

error bars. The only major discrepancy is that value of q_{exp} at MSE channel 9.

This is due to the problems with the MSE channels closest to the centre of the plasma, generally channels 9 and 10 but sometime channel 8 as well. The MSE channels measure $tan(\gamma_{exp})$ which is dependent on $\mathbf{B}_\theta$, when $\mathbf{B}_\theta$ becomes small towards the centre of the plasma then $tan(\gamma_{exp})$ measured by the MSE channels is small and the relative error between $tan(\gamma_{exp})$ and $\triangle\ tan(\gamma_{exp})$ becomes large. It has been noted that there is a systematic calibration error with these inner MSE channel [53]. This systematic error is most prevalent for small MSE angles which correspond to high q-values, as in this case. Also during high density discharges when the NBI suffers from beam attenuation and this effects the accuracy of the innermost MSE channels. For these reasons the channels MSE closest to the centre of the plasma can lead to suspect values of q_{exp}, and in turn can lead to unrealistic and non-monotonic q_{exp}-profiles in the central region of the plasma.

Fig. 4.5 shows the recovery of the q-profile for discharge 13012 after 3.0s with a I_p of 0.8 MA and $\mathbf{B}_\phi$ of 2.0T. The centre of the plasma is between channels 8 and 9. The error bars associated with q_{exp} at channels 9 and 10 are very large and thus q_{exp} is inaccurate and can be discarded from the analysis. The FPJ and CLISTE recoveries fall within experimental error for all other 8 MSE channels.

Fig. 4.7 shows the recovery of the q-profile for discharge 13049 after 1.7s with a I_p of 0.8 MA and $\mathbf{B}_\phi$ of 2.0T. The FPJ and CLISTE q-profiles agree more or less within the first nine q_{exP} error bars for this discharge. The most striking feature of this figure is the significant offset of channel 10 due to calibration error.

Fig. 4.9 shows the recovery of the q-profile for discharge 13169 after 5.3s with a I_p of 1.0 MA and $\mathbf{B}_\phi$ of 2.5T. For the first 7 MSE channels the CLISTE and FPJ q-profile adhere closely to q_{exp}q values but deviate dramatically for the innermost 3 channels. For channels 8-10 the experimental q-values seem to predict a reversed shear discharge, albeit with extremely large error bars, which is highly unlikely for a simple H-mode discharge. In this case the FPJ and CLISTE predictions seem more plausible.

Fig. 4.11 shows the recovery of the q-profile for discharge 12952 after 2.2s with a I_p of 1.0 MA and $\mathbf{B}_\phi$ of 2.5T. This discharge is similar to discharge 13049 in that the FPJ and CLISTE recoveries closely follow q_{exp}q value for the first 9 channels but there is a huge calibration offset in channel 10.

Fig. 4.13 shows the recovery of the q-profile for discharge 12036 after 2.0s with a I_p

of 0.8 MA and $\mathbf{B}_\phi$ of 2.1T. Unlike the previous H-mode discharges this is a single null upper divertor discharge. In this discharge the FPJ and CLISTE recoveries are within error bars for all MSE channels, though channel 8 has very large error bars.

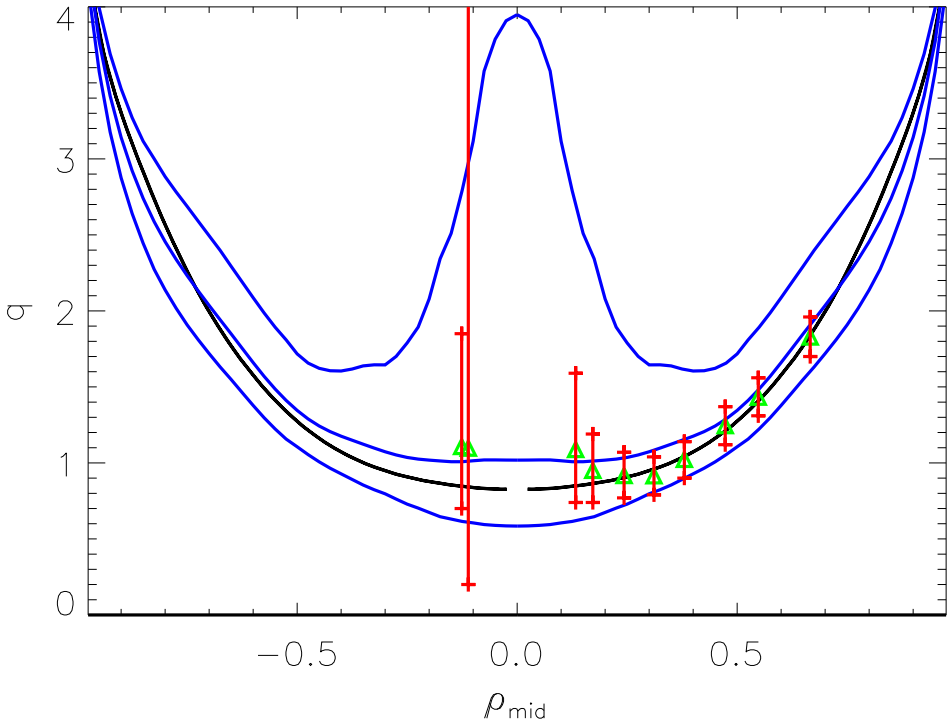

Figure 4.1: *CLISTE and FPJ recovery of q-profile for AUG discharge 12055 at a time of 2.1s, with I_p of 1.0MA and $\mathbf{B}_\phi$ of -2.6T*

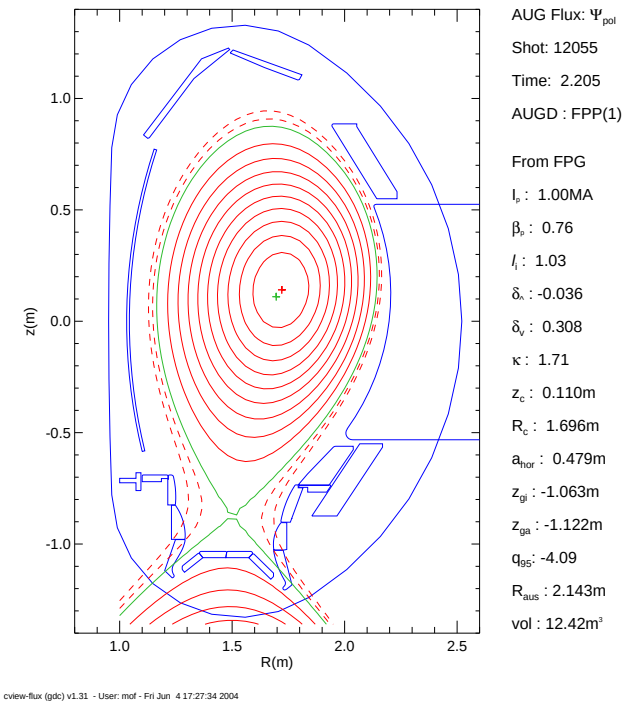

Figure 4.2: *Cross-section of AUG illustrating the magnetic flux and basic plasma parameters for AUG discharge 12055 at 2.1s*

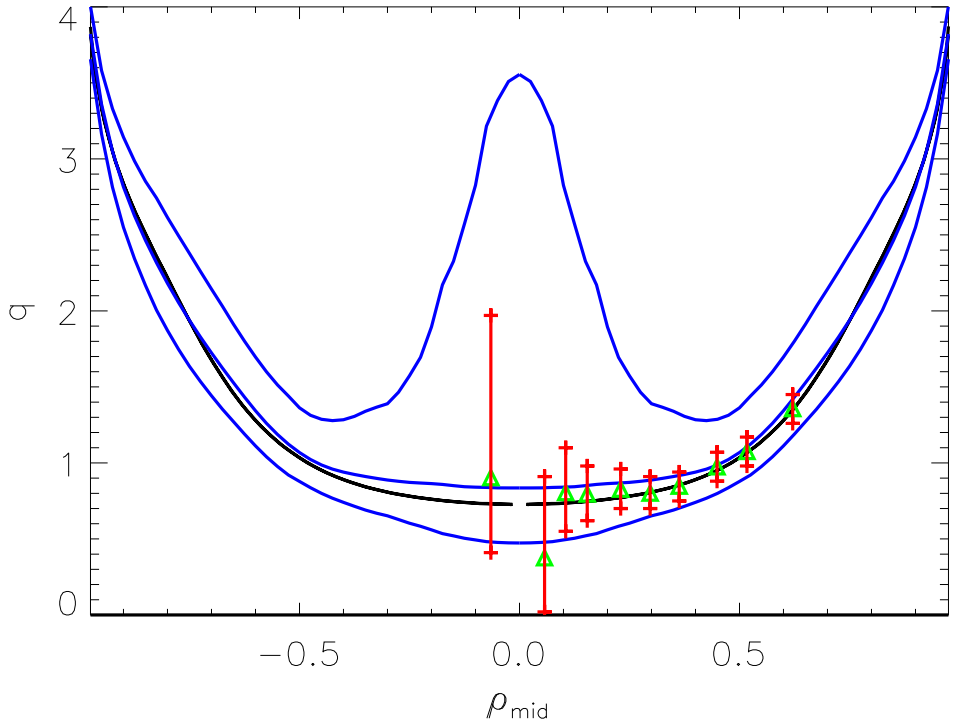

Figure 4.3: *CLISTE and FPJ recovery of q-profile for AUG discharge 12077 at a time of 1.5s, with I_p of 1.0MA and $\mathbf{B}_\phi$ of -2.1T*

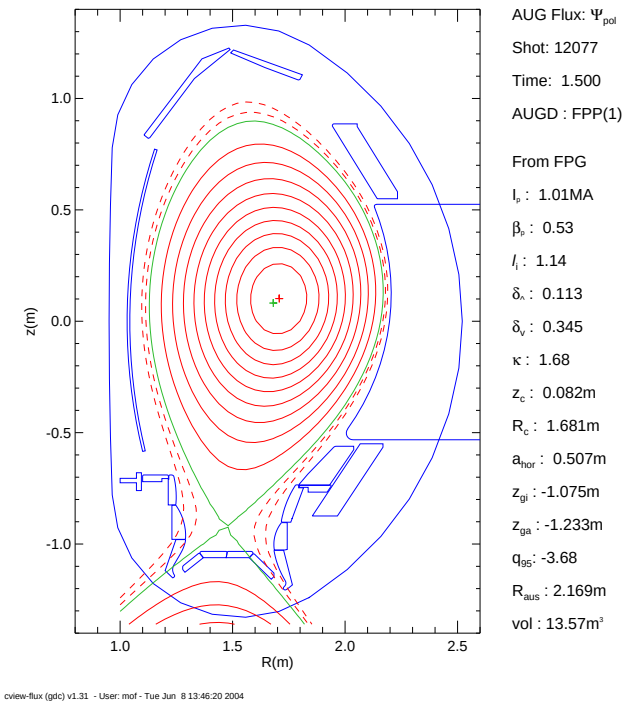

Figure 4.4: *Cross-section of AUG illustrating the magnetic flux and basic plasma parameters for AUG discharge 12077 at 1.5s*

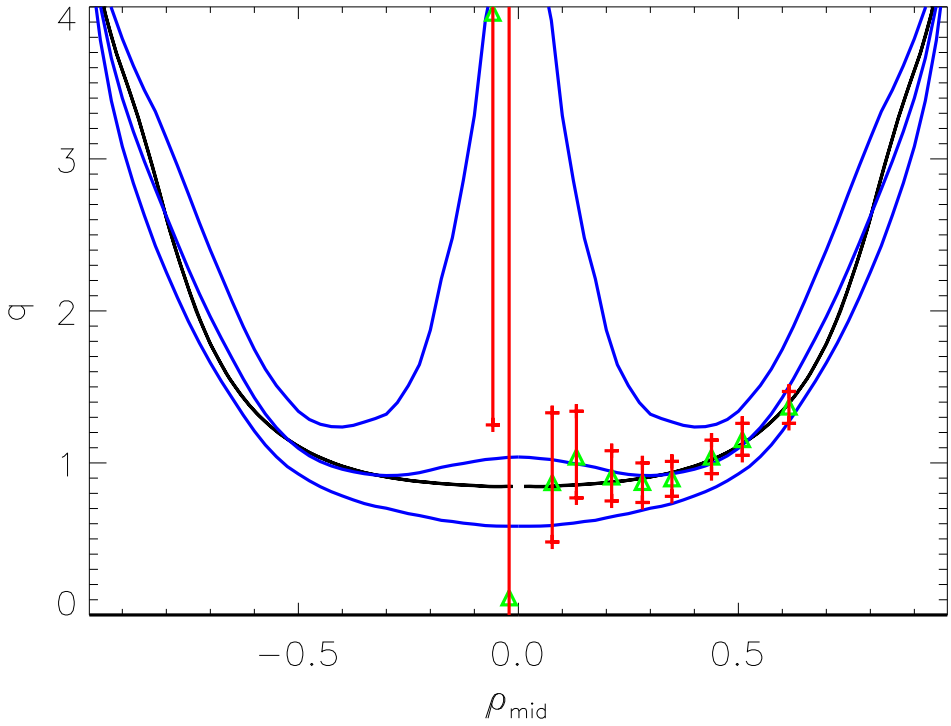

Figure 4.5: *CLISTE and FPJ recovery of q-profile for AUG discharge 13012 at a time of 3.0s, with I_p of 0.8MA and $\mathbf{B}_\phi$ of -2.0T*

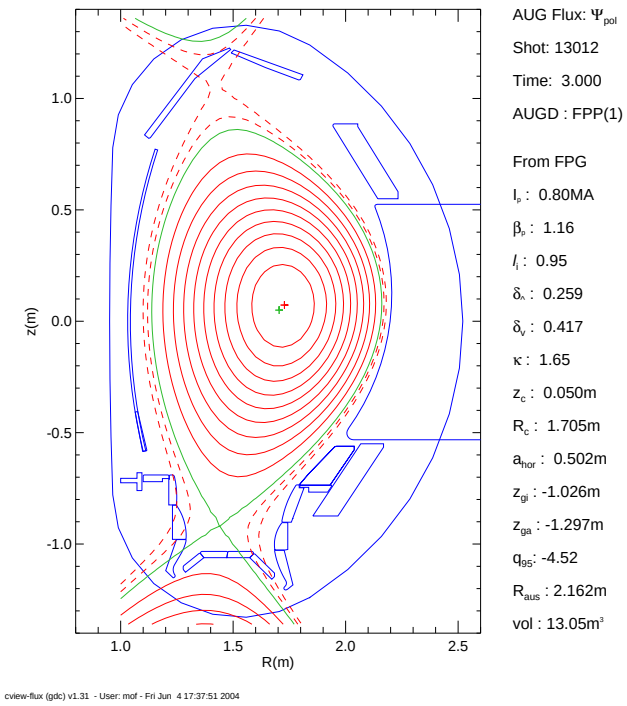

Figure 4.6: *Cross-section of AUG illustrating the magnetic flux and basic plasma parameters for AUG discharge 13012 at 3.0s*

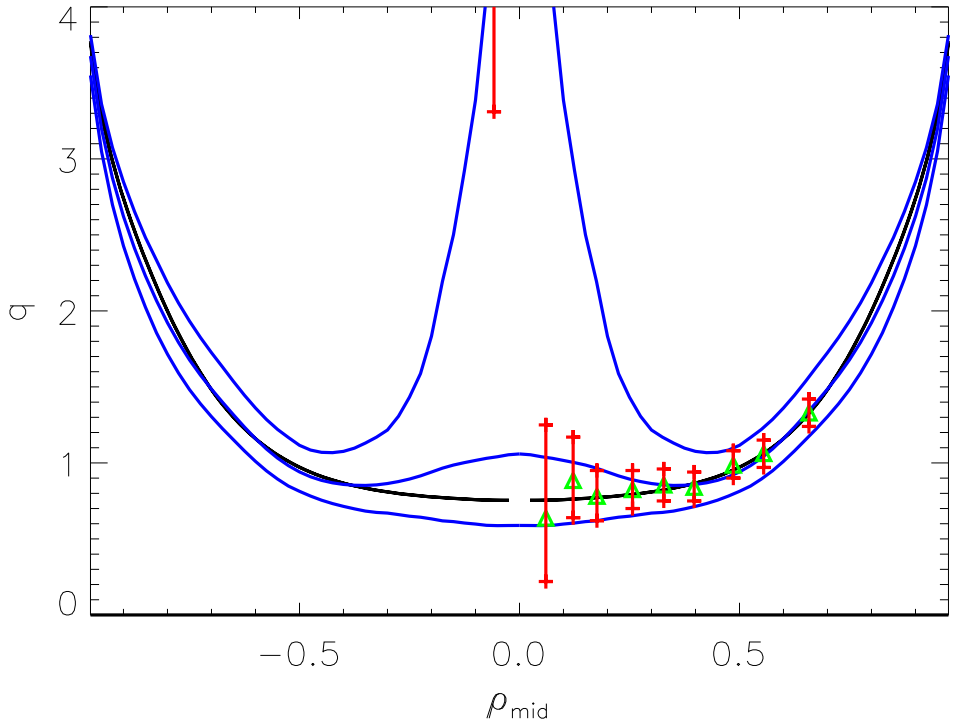

Figure 4.7: *CLISTE and FPJ recovery of q-profile for AUG discharge 13049 at a time of 1.7s, with I_p of 0.8MA and $\mathbf{B}_\phi$ of -2.0T*

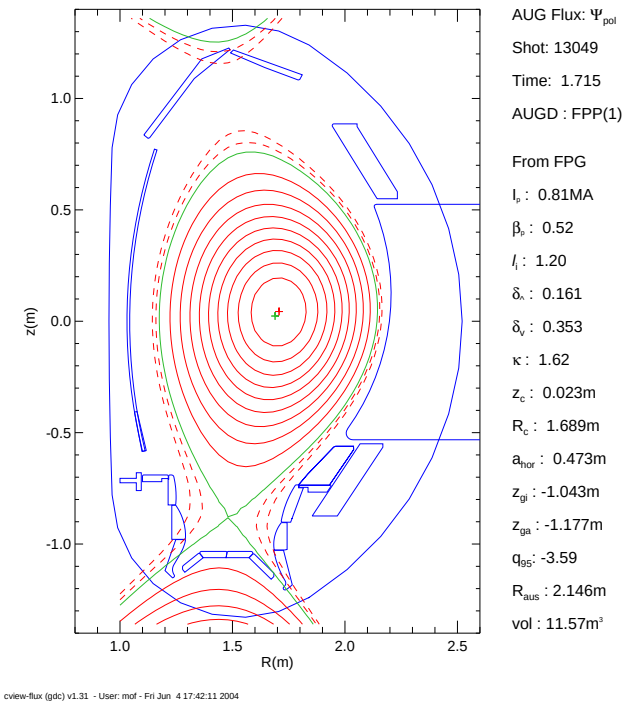

Figure 4.8: *Cross-section of AUG illustrating the magnetic flux and basic plasma parameters for AUG discharge 13049 at 1.7s*

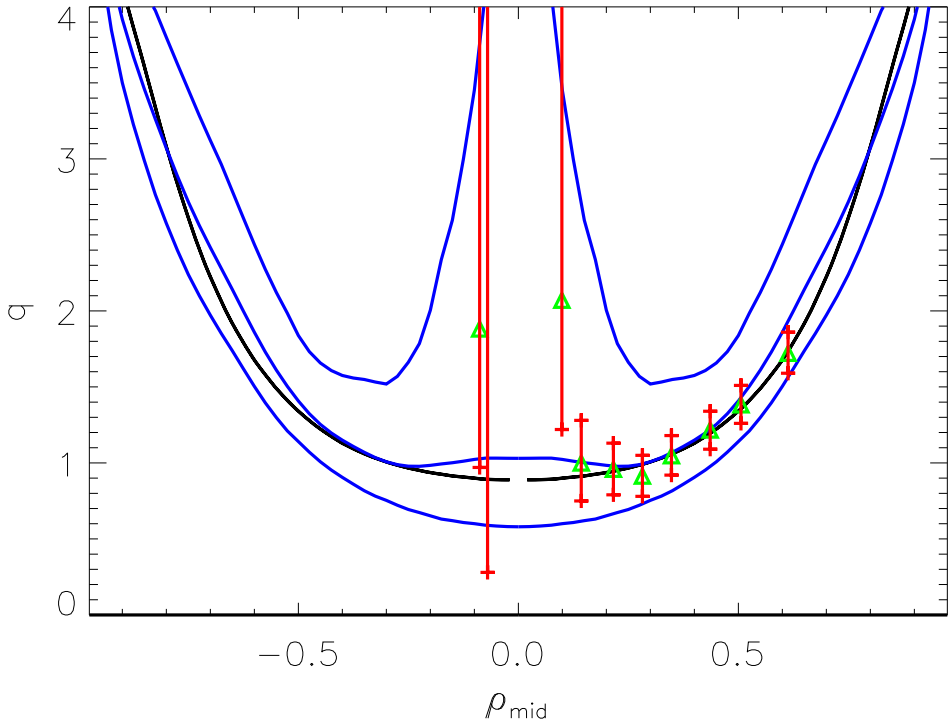

Figure 4.9: *CLISTE and FPJ recovery of q-profile for AUG discharge 13169 at a time of 5.3s, with I_p of 1.0MA and $\mathbf{B}_\phi$ of -2.5T*

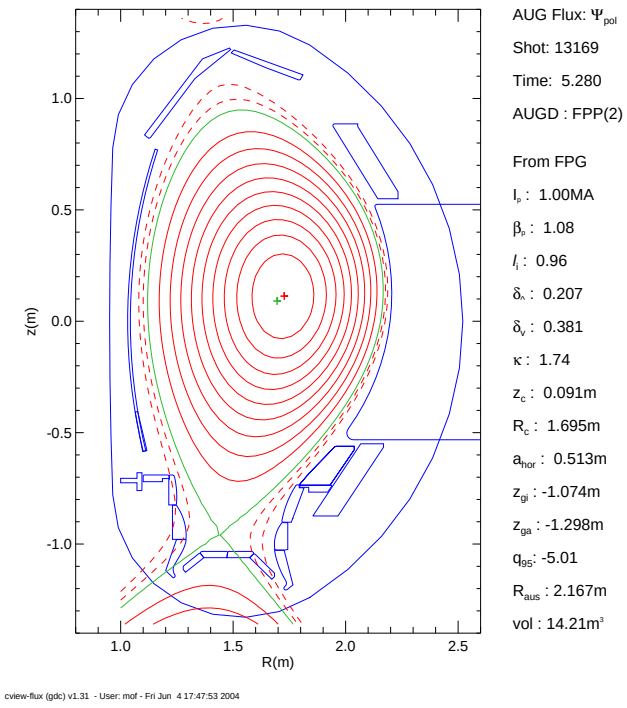

Figure 4.10: *Cross-section of AUG illustrating the magnetic flux and basic plasma parameters for AUG discharge 13169 at 5.3s*

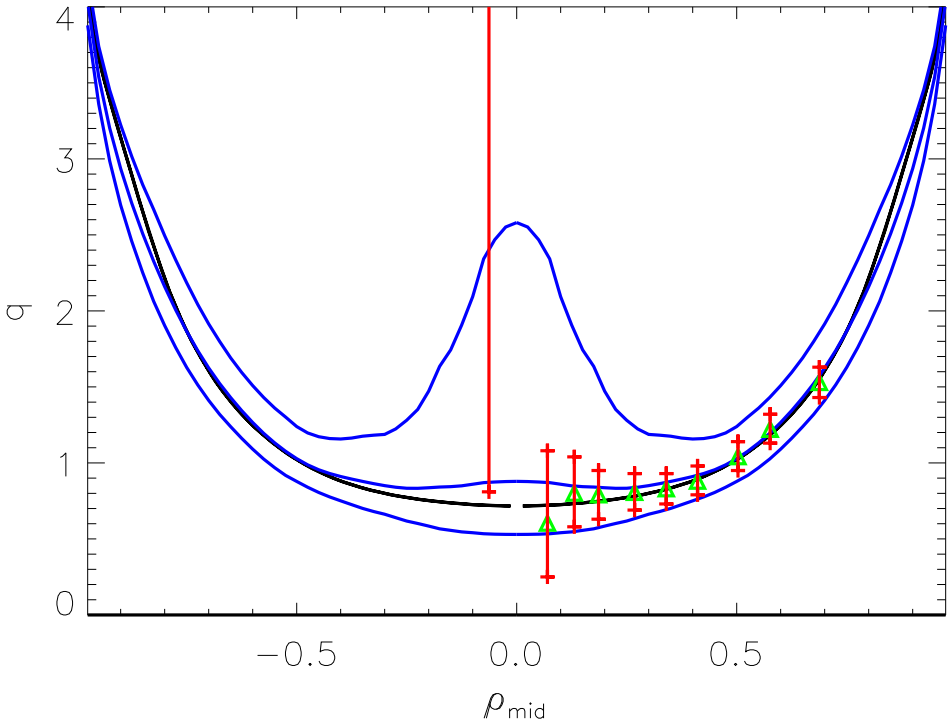

Figure 4.11: *CLISTE and FPJ recovery of q-profile for AUG discharge 12952 at a time of 2.2s, with I_p of 1.0MA and $\mathbf{B}_\phi$ of -2.5T*

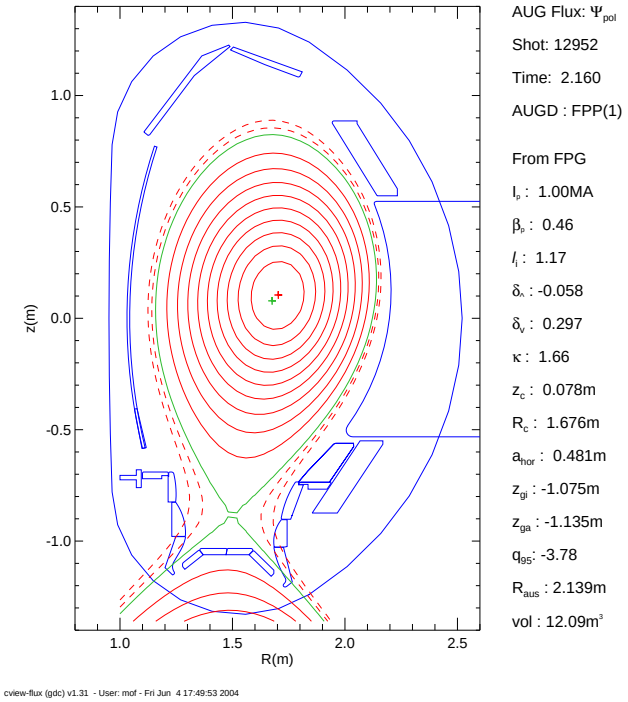

Figure 4.12: *Cross-section of AUG illustrating the magnetic flux and basic plasma parameters for AUG discharge 12952 at 2.2s*

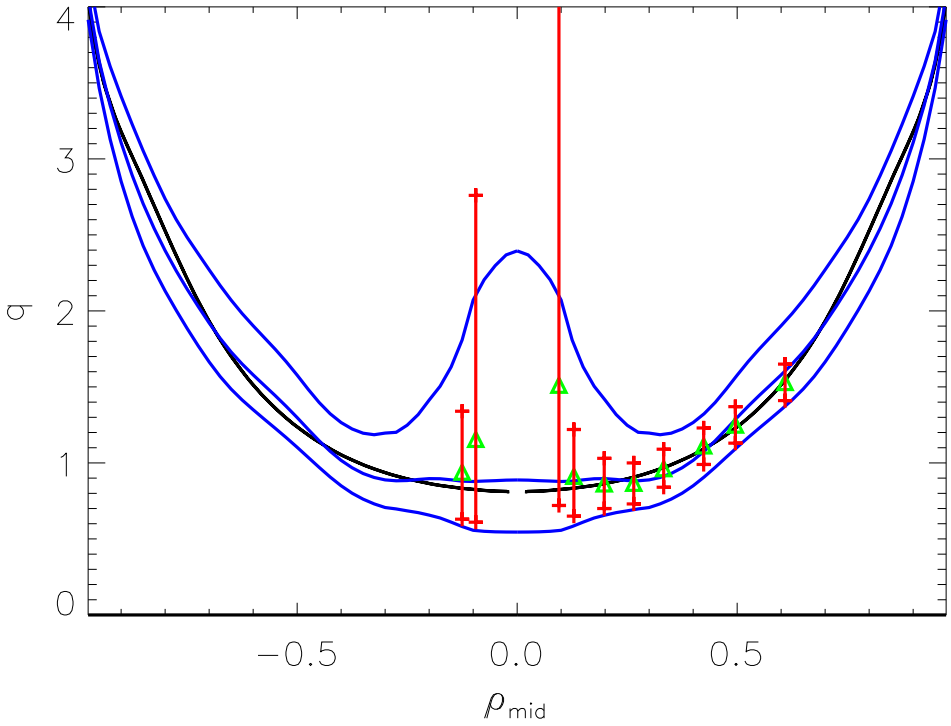

Figure 4.13: *CLISTE and FPJ recovery of q-profile for AUG discharge 12036 at a time of 2.0s, with I_p of 0.8MA and $\mathbf{B}_\phi$ of -2.1T*

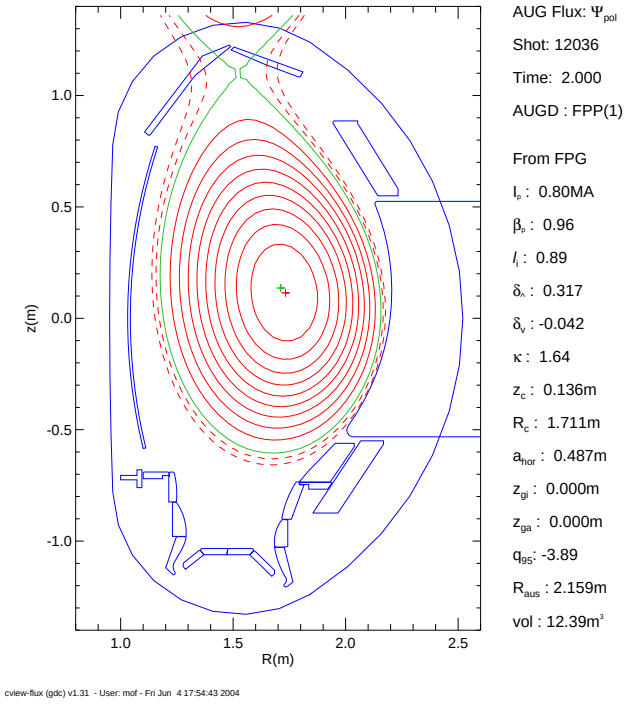

Figure 4.14: *Cross-section of AUG illustrating the magnetic flux and basic plasma parameters for AUG discharge 12036 at 2.0s*

Improved H-mode recoveries The next 4 AUG discharges are improved H-mode discharges. The q-profiles for these discharges are very similar to simple H-mode discharges, the only different is for improved H-mode discharges to have a tendency for a slightly more flat profile towards the centre of the plasma as fishbone instabilities flatten the q-profile due to rapid reconnection events and clamps it close to a q-value of 1 [46], [50].

Fig. 4.15 shows the recovery of the q-profile of discharge 13043 after 3.0s with a I_p of 1.0 MA and $\mathbf{B}_\phi$ of 2.4T. The centre of this plasma discharge is between channels 8 and 9. The q_{exp} error bars at these position are much larger than the q_{exp} error bars at the rest of the channel positions illustrating the lack of information towards the centre of the plasma.

Fig. 4.17 shows the recovery of the q-profile of discharge 13154 after 3.2s with a I_p of 1.0 MA and $\mathbf{B}_\phi$ of 2.5T. Again the FPJ and CLISTE recoveries are within q_{exp} error bars with large error bars for the channels, 9 and 10, towards the centre of the plasma.

Fig. 4.19 shows the recovery of the q-profile of discharge 13044 after 0.6s with a I_p of 0.4 MA and $\mathbf{B}_\phi$ of 2.6T. Although this discharge is by definition an improved H-mode discharge, this timepoint was chosen as it is very early in the discharge and is presented to compare FPJ and CLISTE recoveries of the q-profile during the current ramp-up phase of the discharge. The errors associated with channel 10 are so large it can be ignored. Fig. 4.19 shows that FPJ recovery follows the trend of q_{exp} profile. This is acceptable as I_p and hence $\mathbf{B}_\theta$ is very small, therefore the MSE diagnostic can not be as accurate as during flattop operation.

Fig. 4.21 shows the recovery of the q-profile of discharge 13099 after 3.2s with a I_p of 1.0 MA and $\mathbf{B}_\phi$ of 2.6T. Discharge 13099 is a single null upper divertor discharge. The FPJ and CLISTE recoveries agree with q_{exp} profile within error bars.

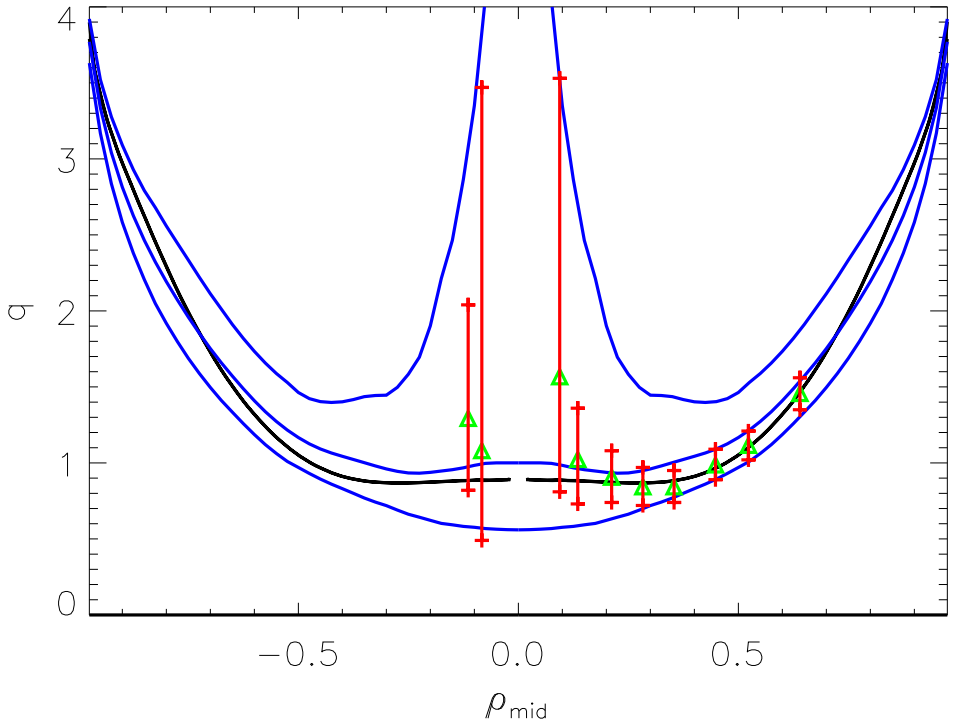

Figure 4.15: *CLISTE and FPJ recovery of q-profile for AUG discharge 13043 at a time of 3.0s, with I_p of 1.0MA and $\mathbf{B}_\phi$ of -2.4T*

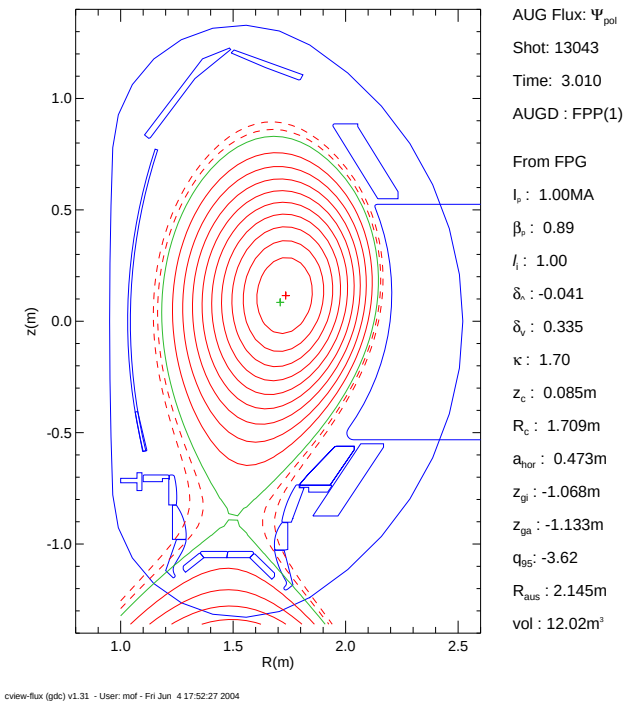

Figure 4.16: *Cross-section of AUG illustrating the magnetic flux and basic plasma parameters for AUG discharge 13043 at 3.0s*

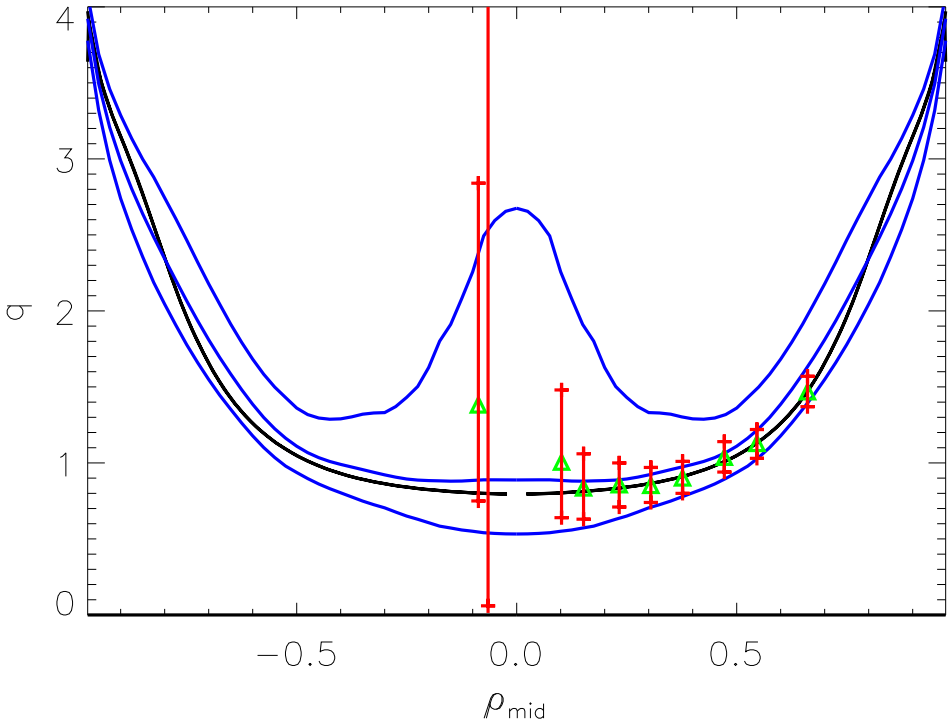

Figure 4.17: *CLISTE and FPJ recovery of q-profile for AUG discharge 13154 at a time of 3.2s, with I_p of 1.0MA and $\mathbf{B}_\phi$ of -2.5T*

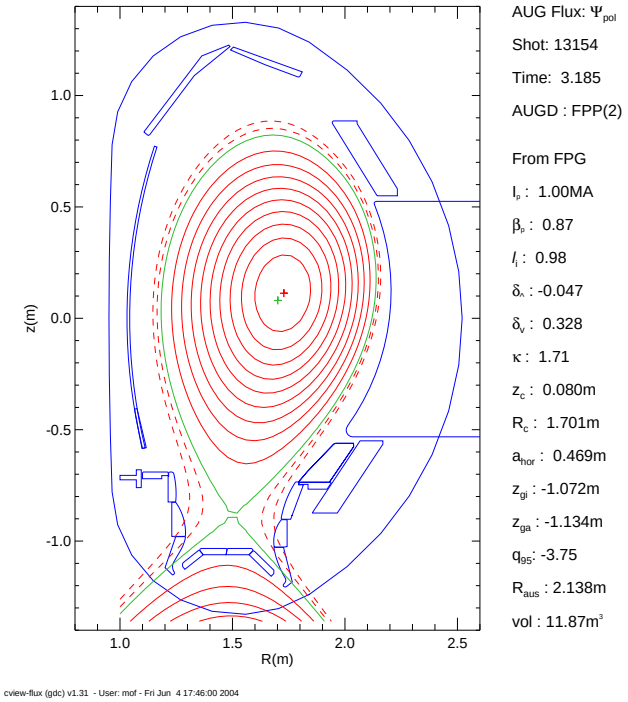

Figure 4.18: *Cross-section of AUG illustrating the magnetic flux and basic plasma parameters for AUG discharge 13154 at 3.2s*

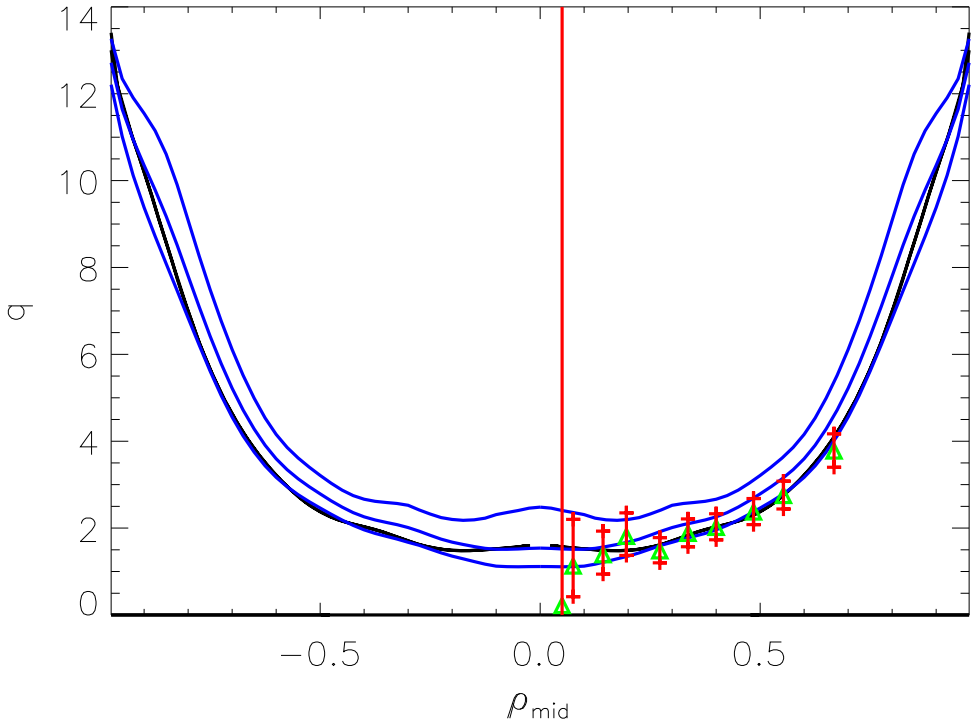

Figure 4.19: *CLISTE and FPJ recovery of q-profile for AUG discharge 13044 at a time of 0.6s, with I_p of 0.4MA and $\mathbf{B}_\phi$ of -2.6T*

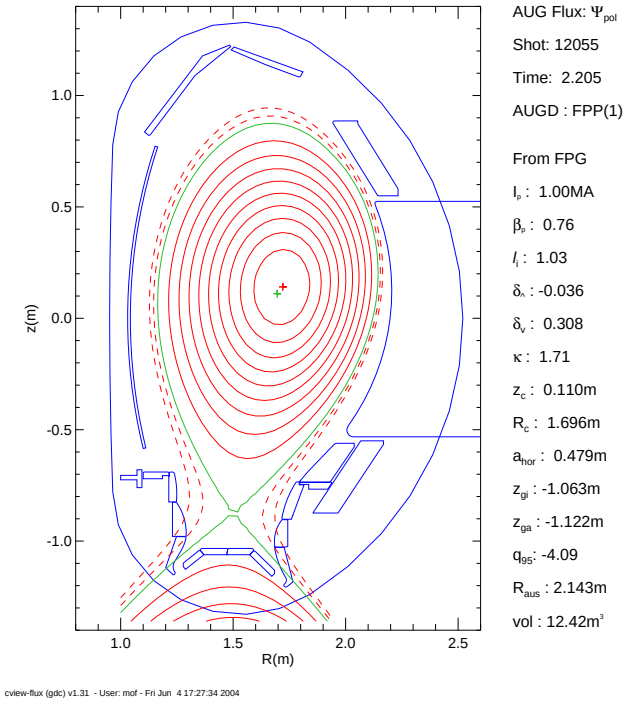

Figure 4.20: *Cross-section of AUG illustrating the magnetic flux and basic plasma parameters for AUG discharge 13044 at 0.6s*

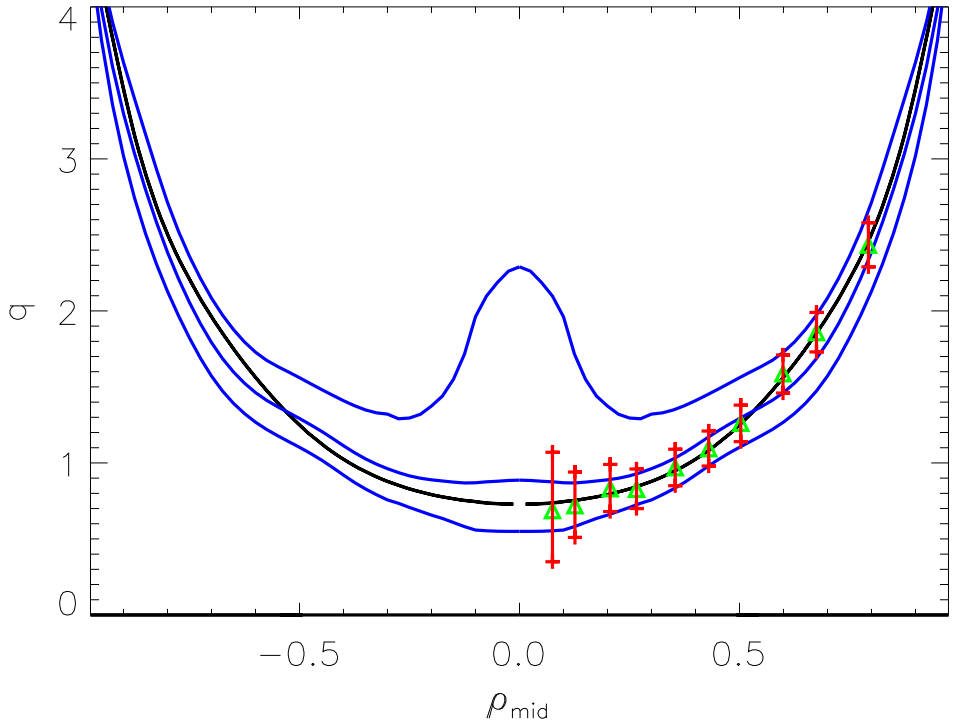

Figure 4.21: *CLISTE and FPJ recovery of q-profile for AUG discharge 13099 at a time of 3.2s, with I_p of 1.0MA and $\mathbf{B}_\phi$ of -2.6T*

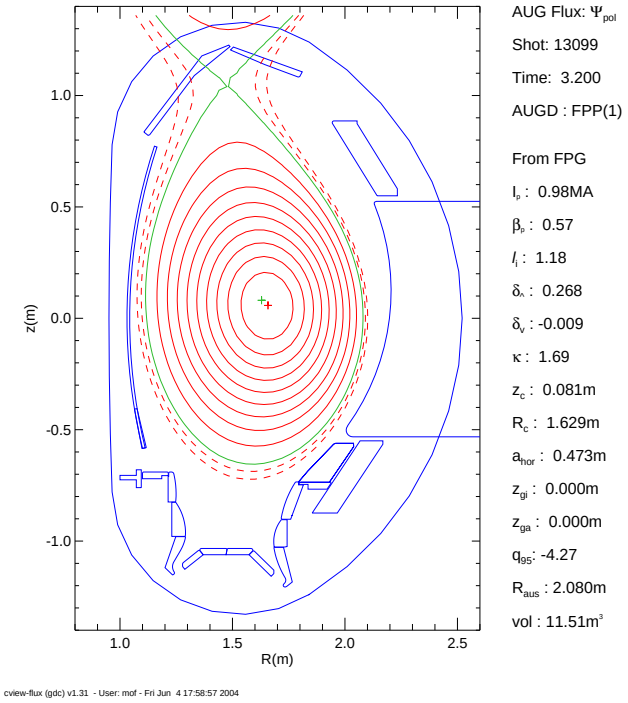

Figure 4.22: *Cross-section of AUG illustrating the magnetic flux and basic plasma parameters for AUG discharge 13099 at 3.2s*

ITB discharges The following 5 discharges are ITB discharges. For AUG ITBs occur transiently during the ramp up stage of specifically designed discharges.

Fig. 4.23 shows the recovery of the q-profile of discharge 13225 after 0.7s with a I_p of 0.7 MA and $\mathbf{B}_\phi$ of 2.6T. As this is the ramp up phase of the discharge and by definition reversed shear discharges have low current density towards the centre of the plasma. Thus $\mathbf{B}_\theta$ is very small towards the centre of the plasma which accounts for the large q_{exp} error bars on channels 8-10. What is important to note is that the minimum value of q q_{min} agrees well within q_{exp} error bars for both FPJ and CLISTE.

Fig. 4.25 shows the recovery of the q-profile of discharge 13130 after 1.3s with a I_p of 1.0 MA and $\mathbf{B}_\phi$ of 2.8T. At this time the discharge has reached flattop and the current diffusion leads to a diminishing and broadening of the central peak in the q-profile, this is apparent in the CLISTE recovery but the FPJ q-profile shows none of this behaviour. The FPJ profile can be explained due to the large error bars associated with the central MSE channels, 9 and 10. Also channel 8 is offset from the rest of the MSE channels. It should be noted that the q_{min} values of FPJ and CLISTE agree within experimental error bars.

Fig. 4.27 shows the recovery of the q-profile of discharge 13148 after 0.8s with a I_p of 0.8 MA and $\mathbf{B}_\phi$ of 2.8T. Fig. 4.29 shows the recovery of the q-profile of discharge 13149 after 0.7s with a I_p of 0.7 MA and $\mathbf{B}_\phi$ of 2.8T. The two discharge will be discussed together as they share many of the same characteristics. As stated reversed shear discharges indicate low current density towards the centre of the plasma, it has been shown that it is possible to have zero current density at the centre of a plasma [51]. These AUG discharges have been shown to be current hole discharges [52]. It is not possible from Figs. 4.27, 4.29 to prove these discharges are current hole discharges, but it is impossible to discount the possibility as the central q_{exp} error bars are large. Again for both discharges the FPJ and CLISTE q_{min} values agree within q_{exp} error bars.

Fig. 4.31 shows the recovery of the q-profile of discharge 13108 after 1.0s with a I_p of 0.8 MA and $\mathbf{B}_\phi$ of 2.8T. For this discharge the CLISTE and FPJ recoveries disagree dramatically towards the centre of the plasma. FPJ shows a reversed shear discharge while CLISTE indicates a simple monotonically increasing q-profile.Both profile agree within q_{exp} error bars for the first 8 MSE channels. The downward trend of q_{exp} from channel 8 to 10 calls the integrity of channels 8-10 into question. From studying the time evolution

of the plasma position and li of the plasma, it was seen that li of the plasma increased due to adiabatic compression as the plasma volume decreased dramatically around this time-point these special circumstances lead to a large error and thus the inner MSE channels are inaccurate [53].

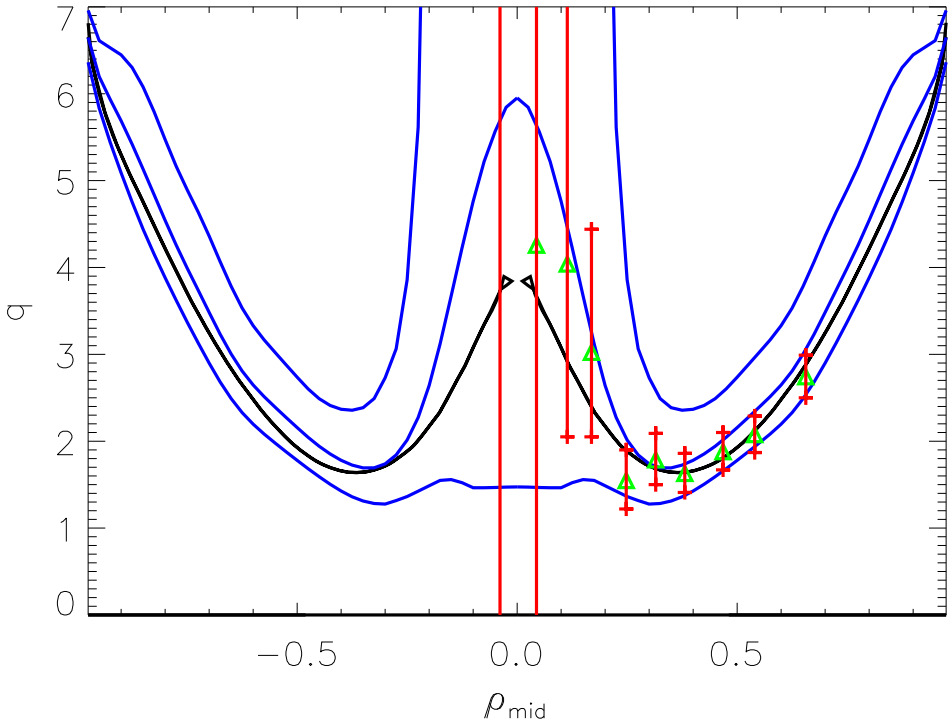

Figure 4.23: *CLISTE and FPJ recovery of q-profile for AUG discharge 13225 at a time of 07.s, with I_p of 0.7MA and $\mathbf{B}_\phi$ of -2.5T*

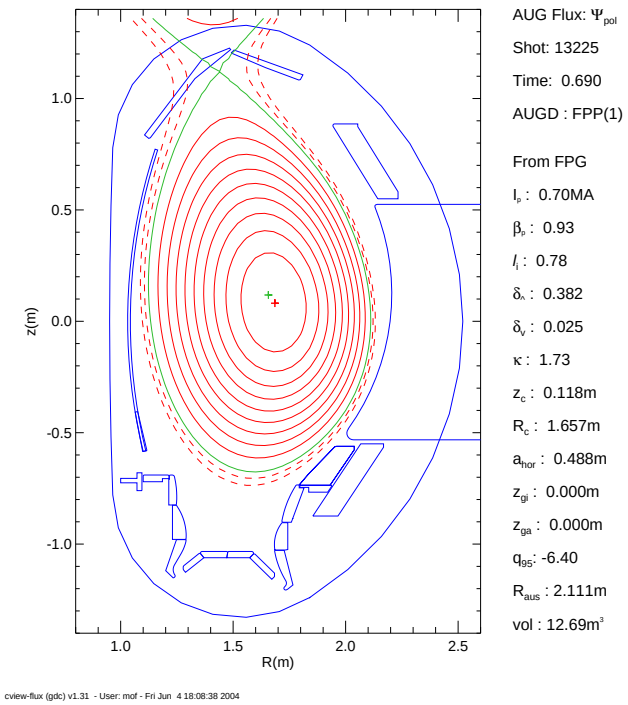

Figure 4.24: *Cross-section of AUG illustrating the magnetic flux and basic plasma parameters for AUG discharge 13225 at 0.7s*

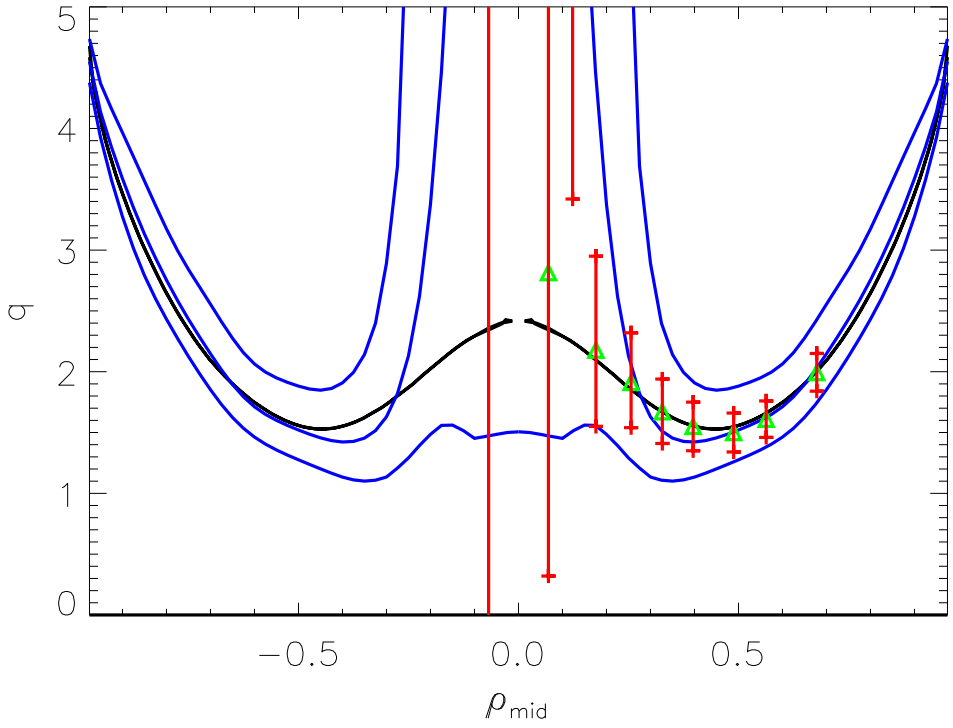

Figure 4.25: *CLISTE and FPJ recovery of q-profile for AUG discharge 13130 at a time of 1.3s, with I_p of 1.0MA and $\mathbf{B}_\phi$ of -2.8T*

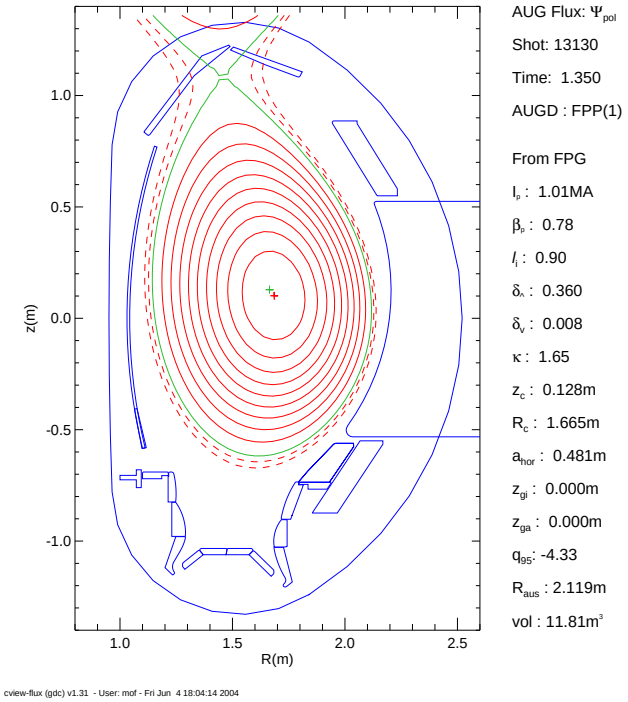

Figure 4.26: *Cross-section of AUG illustrating the magnetic flux and basic plasma parameters for AUG discharge 13130 at 1.3s*

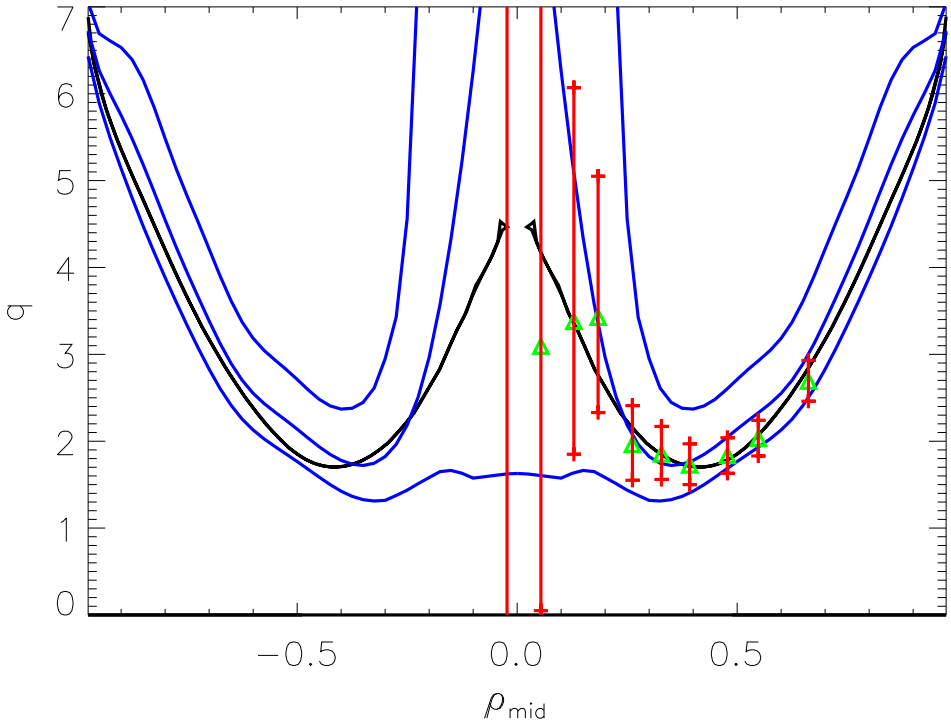

Figure 4.27: *CLISTE and FPJ recovery of q-profile for AUG discharge 13148 at a time of 0.8s, with I_p of 0.8MA and $\mathbf{B}_\phi$ of -2.8T*

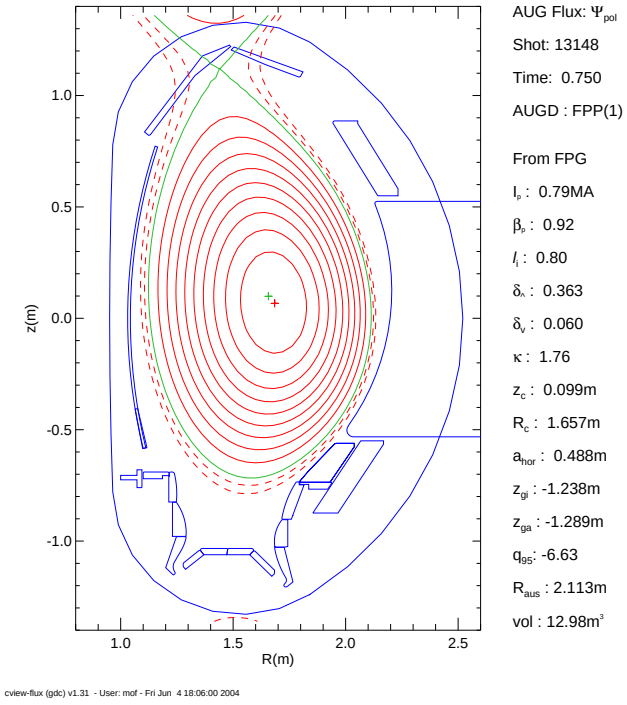

Figure 4.28: *Cross-section of AUG illustrating the magnetic flux and basic plasma parameters for AUG discharge 13148 at 0.8s*

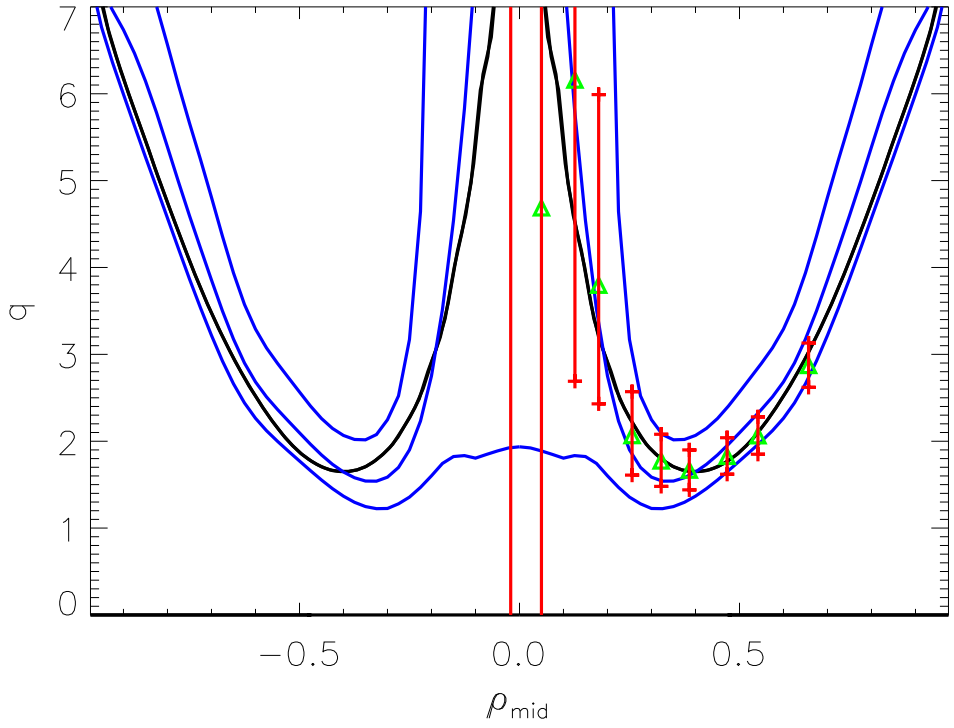

Figure 4.29: *CLISTE and FPJ recovery of q-profile for AUG discharge 13149 at a time of 0.7s, with I_p of 0.7MA and $\mathbf{B}_\phi$ of -2.8T*

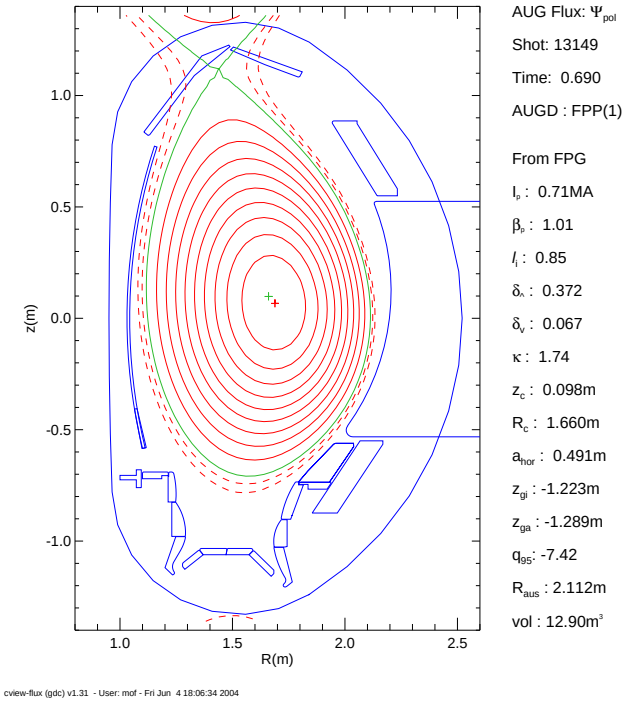

Figure 4.30: *Cross-section of AUG illustrating the magnetic flux and basic plasma parameters for AUG discharge 13149 at 0.7s*

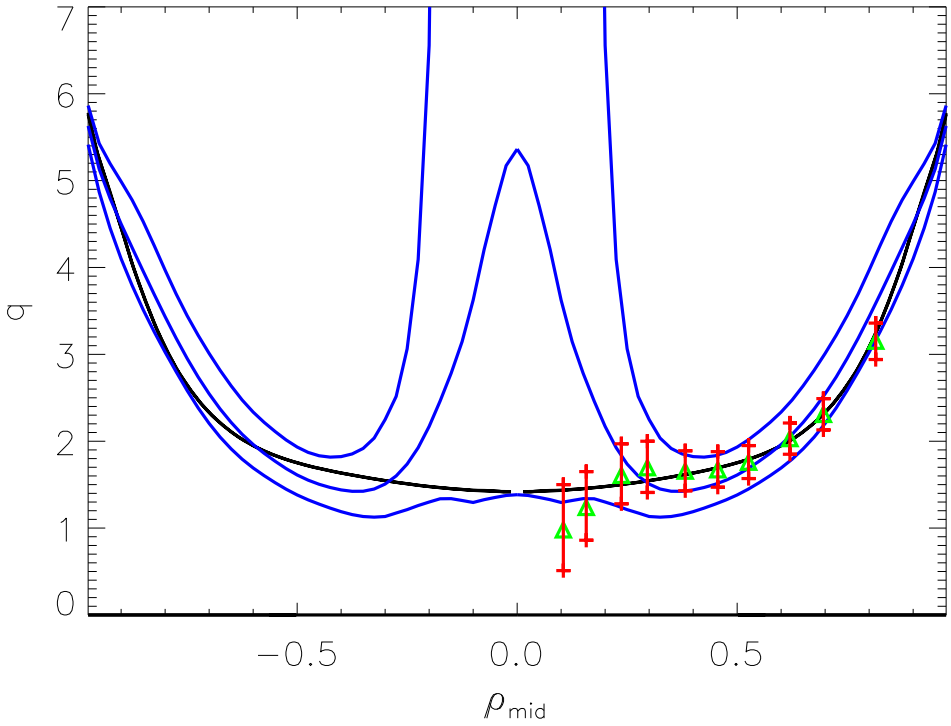

Figure 4.31: *CLISTE and FPJ recovery of q-profile for AUG discharge 13108 at a time of 1s, with I_p of 0.8MA and $\mathbf{B}_\phi$ of -2.8T*

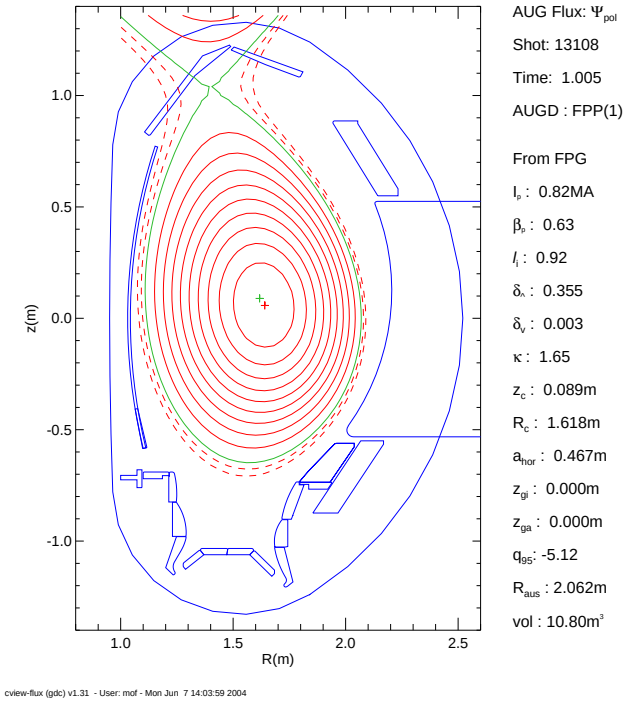

Figure 4.32: *Cross-section of AUG illustrating the magnetic flux and basic plasma parameters for AUG discharge 13108 at 1s*

Summary of FPJ and CLISTE q-profile Recoveries It was decided not to present summary statistic of the AUG recoveries. This was deemed pointless due to the large variation of q-profiles for the various discharge scenarios. In particular the tendency of the q-profile recoveries and error bands to have very large values towards the centre of the plasma would drown out any useful statistical information present.

The general trends present included:

- The various scenarios, with variable I_p and $\mathbf{B}_\phi$, were well recovered.
- The outer q_{exp} error bars were much smaller than the inner q_{exp} error bars, which shows that the inner q-profile is not well recovered.
- The FPJ and CLISTE q-values towards the edge of the plasmas agreed and thus it can be stated that they were well recovered by the magnetic measurements.
- In general for reversed shear discharges the FPJ and CLISTE recoveries of q_{min} agreed within q_{exp} error bars.

4.5.3 Extended FPJ Confidence Limits Analysis

In this subsection a simple test is presented to demonstrate what current density profiles are possible within FPJ confidence limits. The FPJ confident bands for discharge 13154 are used. It is assumed that the FPJ simulated equilibrium database span all physically possible current density profiles. Discharge 13154 FPJ confidence bands are tested to see which of the database q-profiles fall within its limits. Fig. 4.33 shows these results, with the applicable database profiles and CLISTE recovery of discharge 13154 shown within the FPJ error bands. Fig. 4.34 presents a selection of the various associated database current density profiles which fit within the FPJ error bands. It is possible for many different current density profiles to fit within the FPJ recovery. Although some of the more physically adventurous current density profiles will drop out when the FPJ database is narrowed to select only experimentally relevant profiles.

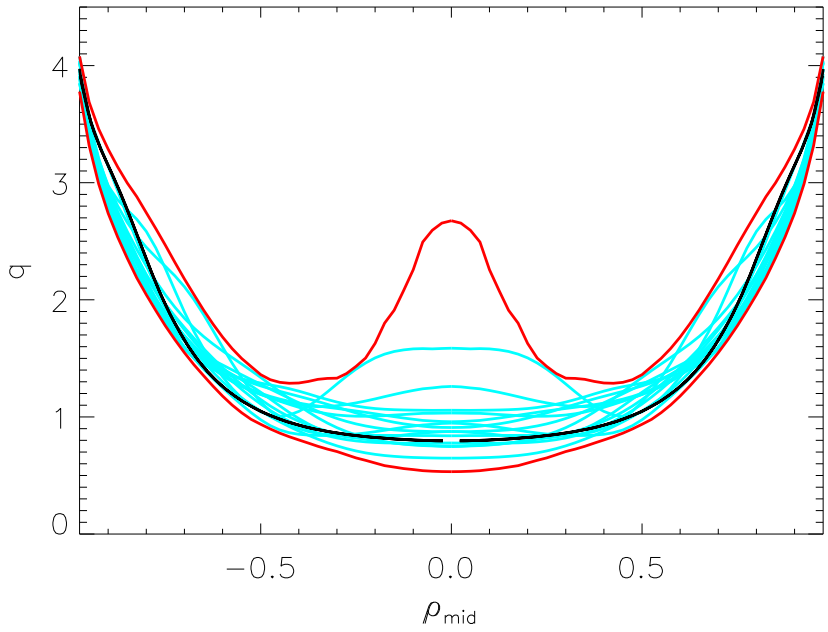

Figure 4.33: *CLISTE recovery (black line) and FPJ confidence limits (red line) of the q-profile for AUG discharge 13154. Also indicated are the simulated AUG equilibrium database q-profiles(cyan lines) which fit the profile within FPJ error limits.*

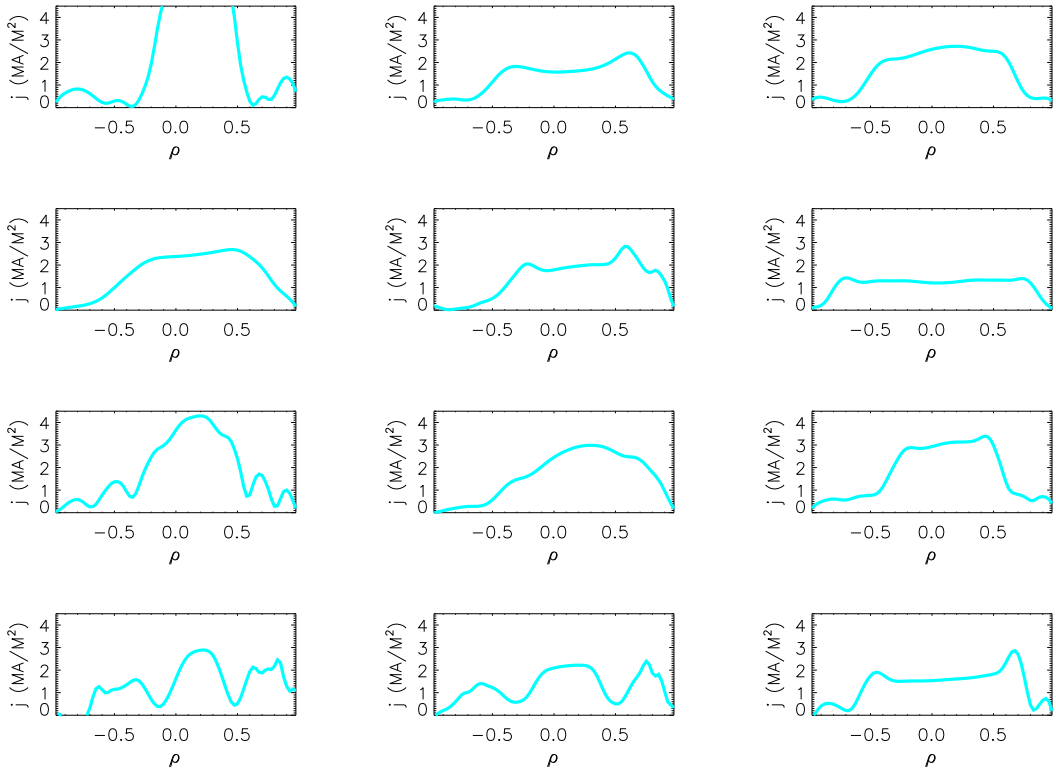

Figure 4.34: *Selection of the associated simulated AUG equilibrium database current density profile which fit within FPJ confidence limits for 13154*

Chapter 5

Just Another Nonlinear Optimisation Suite JANOS:

5.1 Introduction

In this section an alternative method of building the FPJ model is presented.

The original FP model presented by Wind [25] addressed the problem of over coming the inherent multicollinearity of the measurements by making a reduced set of orthogonal linear combinations (LC) of measurements by PCA. These LCs are then utilised as the basis for the FP regression model. As already stated this FP method was applied to ASDEX by Braams [10] and AUG by McCarthy [8] for the recovery of geometric parameters via magnetic diagnostic signals.

Another conventional statistical method used for the recovery of physical parameters from fusion experiments is the use of neural networks (NN) mappings. A good overview of NN is given in [32]. Lister first introduced this technique for the extraction of equilibrium parameters in the D111-D tokamak [54]. NN have also been used to extract plasma parameters on COMPASS-D [55], PBX-M [56], AUG [57], JT-60 [58]and ITER [59].

Various hybrid statistical methods were developed by Na [60] for recovering equilibrium plasma parameters on KSTAR.. These hybrids are based on NN methods with FP influences, the optimal recovery method presented in that work was based on a double NN. This double NN method was also used to recover equilibrium parameters in SST-1 [61].

In this chapter the method of equilibrium parameter recovery is based on FP methods with the utilisation of a nonlinear optimisation (NLO) function in place of the standard

PCA. The method is called **J**ust **A**nother **N**onlinear **O**ptimisation **S**uite (JANOS) [63] [**?**]. PCA chooses orthogonal LCs to maximise the variance of the leading LCs. This method is totally independent of the equilibrium parameters under investigation. It was hypothesised that if different LCs were chosen, not necessarily orthogonal, to optimise the weighting of the diagnostic measurements which contain most information on the parameters under investigation in the leading LCs then a more compact model with fewer LCs could be built. A more compact model would lead to shorter computational times. It is also planned to include the 10 half energy MSE channels into the FPJ analysis. If these measurements were included into the standard FP model, it would increase the FP model. The JANOS code will keep the increase of the FPJ model size to a minimum. JANOS was created with this in mind. A complete description of the JANOS algorithm is given in section 5.2. Database results are presented in section 5.3 and finally JANOS recoveries of AUG q-profiles are presented in section 5.4

5.2 Description of the JANOS Algorithm

The essence of JANOS is the selection of a small set of iteratively optimised linear combinations NLC of the data with the objective of a successful recovery of $t\,(\rho_{mid})$ using a more compact quadratic model than that of the standard FP approach. Thus we expect NLC $<$ NP where NP is the number of PCs of the input signals needed to give a good FP fit. The justification for reducing the number of linear combinations below NP lies in the observation that not all the variance of the magnetic measurements is due solely to the variation in the current density profile or equivalently the t profile and hence we expect that it will be possible to recover $t\,(\rho_{mid})$ using fewer than the NP transformed measurements which describe all measurement variance. This compact FP model is given by:

$$y_{i,r} = \sum_{l=0,j=l}^{NLC} \beta_{l,j,r} \left(\sum_{t=1}^{NP} w_{t,l} P_{i,t} \right) \left(\sum_{u=1}^{NP} w_{u,j} P_{i,u} \right) + \epsilon_{i,r} \tag{5.1}$$

where $y_{i,r}$ is the value of the r^{th} of NR recovered parameters for the i^{th} of NC cases in the database, $P_{i,t}$ is the t^{th} PC score for the i^{th} case, $(w_{1,l}, w_{2,l}, ..., w_{NP,l})$ is the vector of measurement weights for the l^{th} of LC optimised linear combinations and $((\beta_{l,j,r}, l = 0, LC), j = l, LC)$ is the set of (LC+1)(LC+2)/2 co efficients which recover the r^{th} output parameter (l = 0corresponds to the intercept where $\mathbf{w_o}.\mathbf{p_i} \equiv 1$)).

Starting with the NP PCs, JANOS is structured as follows: Choose the matrix of weights $\mathbf{W}_(NP \times LC)$ which minimises the cost function defined as

$$Cost = \sum_{i=1}^{NC} \sum_{r=1}^{NR} (y_{i.r} - \hat{y}_{i.r})^2 + \alpha \sum_{l=1}^{NLC} \left(1 - (\sum_{t=1}^{NP} w_{t,l}^2)^2 \right)^2 \tag{5.2}$$

where $\hat{y}_{i,r} = y_{i,r} - \epsilon_{i,r}$ is the predicted value of $y_{i,r}$, in this circumstance ϵ refers to the error associated with the recovery of $\hat{y}$ rather than the inverse aspect ratio of the tokamak, and the rightmost term, tuned by the regularisation parameter α, favours weights vectors of unit norm: $w_l.w_l = 1$. This avoids indeterminacies in the magnitude of W and the set of β's since essentially only the product $||W||||\beta||$ is unique where $||W||$ and $||\beta||$ represent the norms of the weight vectors and the linear regression coefficients, respectively.

The NAG routine E04FCF preforms the nonlinear optimisation of the NP×LC weight coefficients. In a conventional neural network algorithm the β's would be varied along with the W matrix. A special feature of JANOS is that the β's are not explicitly part of the nonlinear optimisation, but rather are determined by a linear regression lapack routine called within the user-supplied subroutine which is in turn called by E04FCF to determine the set of NC×NR residuals $\{\epsilon_{i,r}\}$. For the present case where the set of parameters to be recovered consists of an array of discrete values of ι along the ρ_{mid} axis, the residuals will be highly correlated. We have improved the convergence of the algorithm by using instead the Mahalanobis transformed, see Appendix D, residuals:

$$\mathbf{z} = \mathbf{S^{-1/2}r} \tag{5.3}$$

where $\mathbf{r} = (\epsilon_{1,i}, ..., \epsilon_{NR,i})$ is the vector of NR residuals for each case in the database and $\mathbf{S_{NR \times NR}}$ is the covariance matrix of the recovery errors which is determined at the outset by "best possible" regression for each parameter using all NP linear combinations. The "best possible" regression is the case is regression with maximum number PCs used to build the full quadratic set of predictors which will not over-fit the data. The advantage of using the Mahalanobis transformation is that this transform is used to eliminate the correlation between residuals and standardise the variance of each residual.

5.3 JANOS Database Results

In this section results from the JANOS and PCA based FPJ recoveries of the AUG equilibrium database ι profile over ρ_{mid} co ordinates are presented. Results from category

3 and category 4 plasmas are presented in Figs. 5.1, 5.2 respectively.

Figs. 5.1 5.2(i) shows the ι RMSE over ρ_{mid} co ordinates for JANOS and PCA FPJ recoveries with regression models based on 16 LCs for simulated AUG database plasmas . It should be noted that the RMSEs in this chapter, both JANOS and PCA, are based on one test dataset of simulated AUG equilibria. It was decided to used models based on 16 LCs as this is presently the number of LCs that the FP based AUG online control system uses. It should be noted that the 16 JANOS LCs are chosen by the code to be the 16 LCs most applicable to recovering the ι profile from an original set of 20 magnetic and 5 MSE PCs. Figs. 5.1 5.2(i) demonstrate that the JANOS based FPJ recovery is more accurate from $0.0 - 0.8\rho_{\text{mid}}$. From $0.8\rho_{\text{mid}}$ to the edge of the plasma the PCA based FPJ recovery is slightly more accurate. The improvement of the JANOS based regression is most obvious in the region $0.3 - 0.7\rho_{\text{mid}}$. The JANOS code is based on minimising a cost function vector Eqn. 5.1 where each vector component is based primarily on the sum over the entire ρ_{mid} profile of the SSE of each individual ι error. The contribution to each cost function component from the individual SSE in the region from $0.8\rho_{\text{mid}}$ towards the edge of the plasma is quite alot less that that in the inner region of the plasma. Originally it was hypothesised that this was the reason why the PCA based FPJ ι regressions are more accurate in this region than the JANOS based ι regressions. To overcome this problem each individual ι SSE was normalised by the RMSE of its best possible regression to ensure that magnitude of each contribution from each individual ι error to its cost function component was comparable. It was found that this did not reduce the JANOS ι RMSE to a level better than that of the PCA RMSE.

The PCA ι RMSE is better than that of the JANOS ι RMSE in the outer region of the plasma where the recoverability of the ι profile depends on the magnetic measurements . The JANOS ι RMSE is better for the recovery of the inner region of the profile which in the radial position spanned by the MSE diagnostic channels. It is now hypothesised that the JANOS code concentrate on optimising the LCs for maximum weighting of the MSE diagnostic measurements, thus the code has difficulty in accurately recovering the q-profile in the outer region of the plasma.

Figs. 5.1, 5.2(ii)-(iv) are presented to show the trend of JANOS and PCA based ι recoveries for simulated equilibrium database plasmas with increasing LCs in the regression at the $0.0\rho_{\text{mid}}$, $0.25\rho_{\text{mid}}$, $0.50\rho_{\text{mid}}$, $0.75\rho_{\text{mid}}$ and $0.95\rho_{\text{mid}}$ positions respectively. As

expected the accuracy of each regression generally increases with the addition of LCs to the regression. In a small number of cases, i.e. in Fig. 5.1(iii) from 14LCs to 18 LCs, the t RMSE increases with the addition of LCs. While the addition of LCs into the regression model does add diagnostic information to the model, it is possible that this information is irrelevant to some of the individual regression and thus for specific cases this addition diagnostic information will act as noise, as in the example stated. Also in the JANOS cases it is possible that the JANOS code has not reached a global minimum and thus the diagnostic information is not fully utilised and the JANOS based regression model is not fully optimised. It is obvious from Figs. 5.1, 5.2(ii)-(iv) that the general trend for the various regression models that for the inner part of the profile the JANOS based regression is more accurate, while for the outer region of the plasma the PCA based regression is marginally more accurate

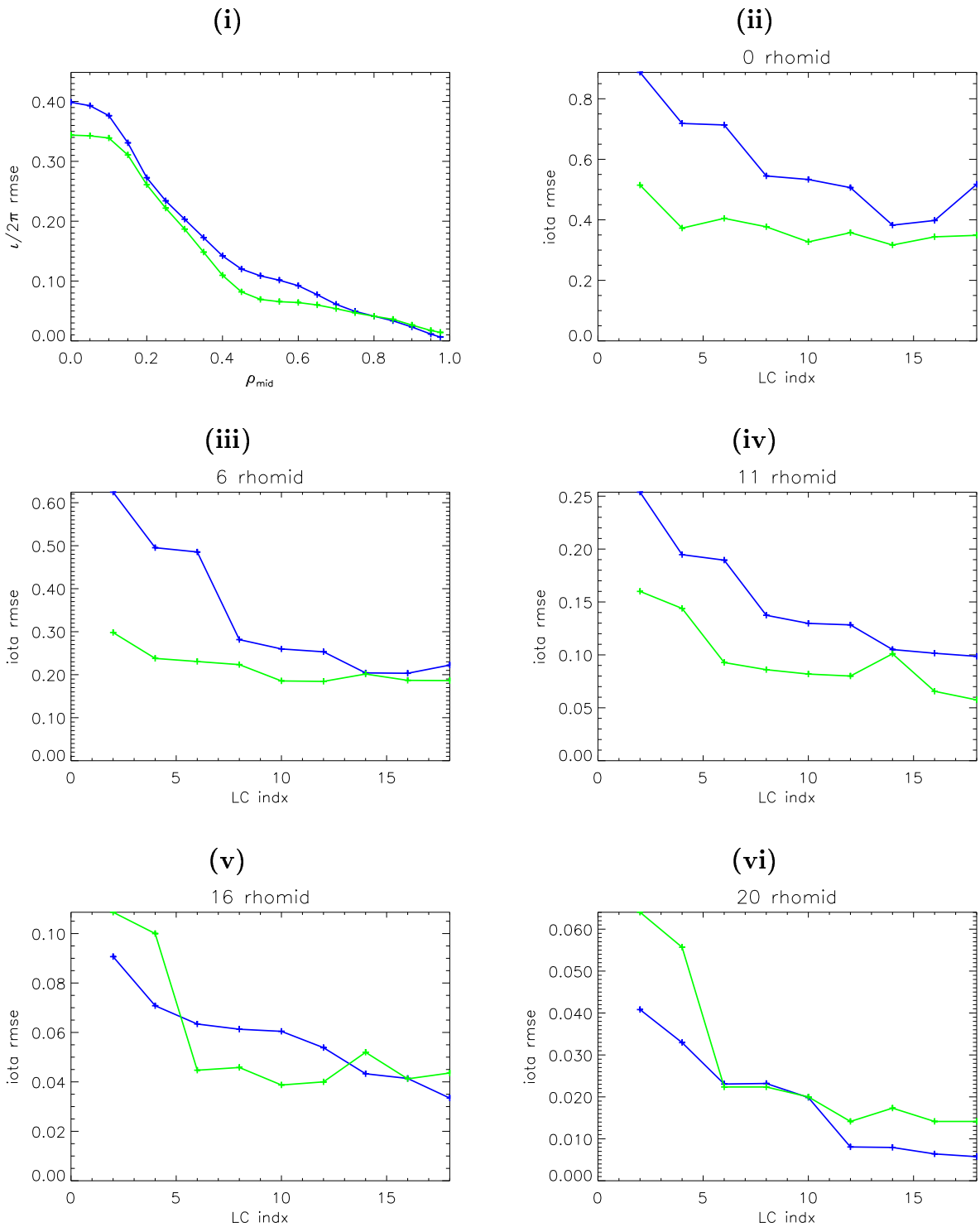

Figure 5.1: *AUG category 3 plasma equilibrium database analysis comparing PCA and JANOS FPJ results; (i) presents the RMSE for both JANOS and PCA FPJ recovery of the database* ρ_{mid} ι *profile with a regression model based on 16 LCs, illustrating the reduction in* ι *RMSE due to the JANOS method;(ii)-(vi) presents the improvement, at various fixed* ρ_{mid} *positions, of* ι *recovery for both JANOS and PCA FPJ recovery with the addition of more LCs.(ii)-(iv) represent* $0.0\rho_{\text{mid}}$, $0.25\rho_{\text{mid}}$, $0.50\rho_{\text{mid}}$, $0.75\rho_{\text{mid}}$ *and* $0.95\rho_{\text{mid}}$ *positions respectively.*

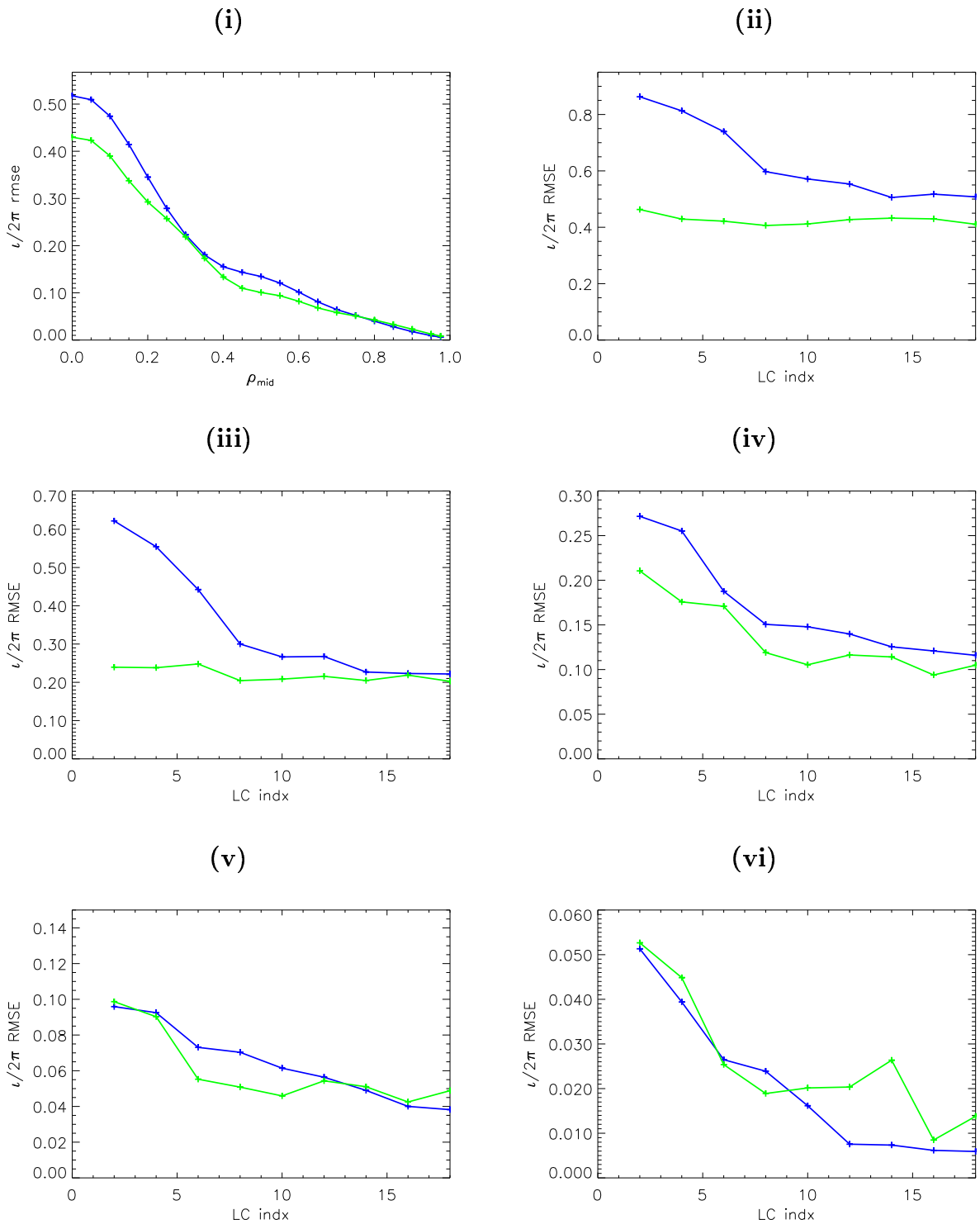

Figure 5.2: *AUG category 4 plasma equilibrium database analysis comparing PCA and JANOS FPJ results; (i) presents the RMSE for both JANOS and PCA FPJ recovery of the database* ρ_{mid} ι *profile with a regression model bases on 16 LCs, illustrating the reduction in* ι *RMSE due to the JANOS method;(ii)-(vi) presents the improvement, at various fixed* ρ_{mid} *positions, of* ι *recovery for both JANOS and PCA FPJ recovery with the addition of more LCs.(ii)-(iv) represent* $0.0\rho_{\text{mid}}$, $0.25\rho_{\text{mid}}$, $0.50\rho_{\text{mid}}$, $0.75\rho_{\text{mid}}$ *and* $0.95\rho_{\text{mid}}$ *positions respectively.*

5.4 AUG Experimental Results

5.4.1 Introduction

In this section AUG CLISTE and JANOS FPJ recovered q-profiles are presented, in the same format as in Section 4.5. The same AUG discharges at the same time-points are analysed, the only difference is the inclusion of the JANOS FPJ recoveries.

The error bars associated an JANOS FPJ recovered AUG q-profile are tested to ascertain how many simulated experimental AUG equilibrium database q-profiles fit within the error bar limits. The various current density profiles associated with these database q-profiles are then presented to illustrate the different types of current density profiles that could be possible within FPJ recovery limits.

5.4.2 Selection of AUG q-Profile Recoveries

The general layout for all the AUG q-profile recovery representations is identical to those in Section 4.5.2. The FPJ recovery and 95% confidence bands are represented by three solid blue lines. The CLISTE recovery is indicated by the solid black line. q_{exp} at each of the 10 MSE channels is indicated by the green triangle, while the q_{exp} error bars are indicated by the vertical solid red lines.

H-mode recoveries As the CLISTE q-profile recovery and q_{exp} are identical for all discharge time-points as in Section 4.5.2 all the points made for these in that section hold for this discussion. It should be noted that as the JANOS based FPJ model is based on only 16 LCs, where the best possible PCA based regression model was based on 25LCs.

The first 6 H-mode JANOS FPJ recoveries in Figs 5.3- 5.8 are single null lower divertor, category 4, plasmas. The JANOS FPJ recoveries in these cases are close to, if not within q_{exp} error bars. In each case, the H-mode profile has slight reversed shear, due to Eqn. 4.21 this leads to JANOS FPJ error bars to be very large. This slight reversed shear could be due an FPJ database bias. With only 16 LCs of a possible total of 56 diagnostic measurements available to the regression model and as the ι profile is poorly recovered in the region towards the centre of the plasma, it is difficult for the JANOS FPJ model to recovery the central q-profile. In this circumstance the estimated JANOS FPJ AUG q-profile recovery will tend toward the simulated database mean. As shown in Fig. 3.5(iv)

the database mean is a reversed q-profile.

Fig. 5.5 shows that in the region between the outermost MSE channel and the edge of the plasma the CLISTE recovered q-profile is outside the JANOS FPJ error bars for discharge 13012.

Whilst the JANOS FPJ q-profile is again slightly reversed the associated error bars for discharge 12036 in Fig. 5.9 is a single null upper divertor category 3 plasma are much narrower than for the category 4 plasma. These narrower error bars are due to the lower absolute ι RMSE in the database recovery for category 3 plasmas relative to category 4 plasmas as presented in in Figs. 5.1(i) and 5.2(i).

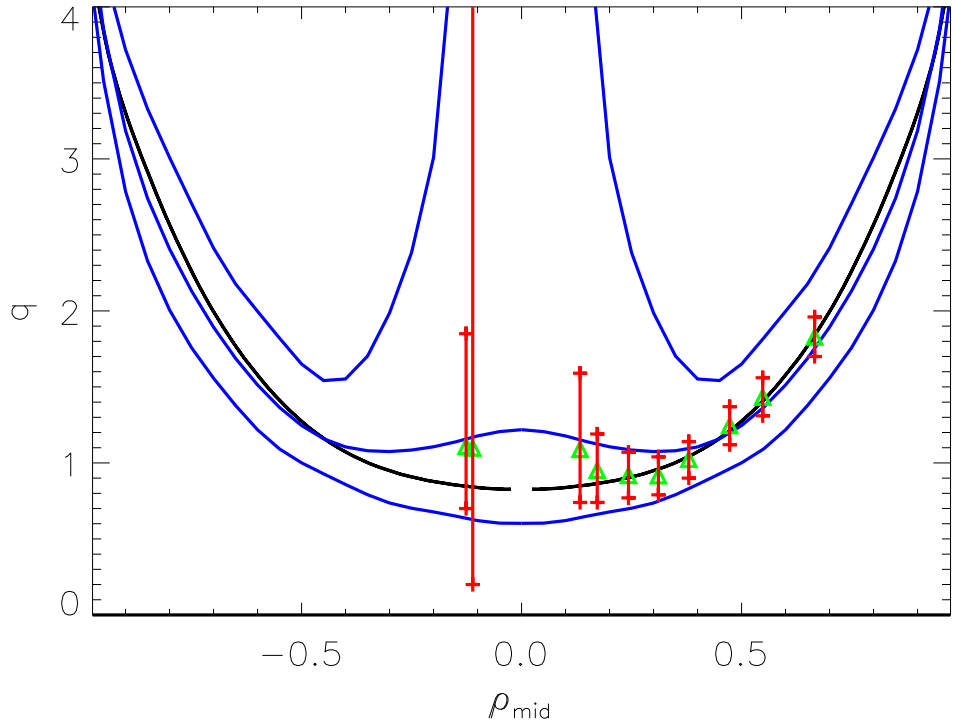

Figure 5.3: *Recovery of AUG q-profile for discharge 12055*

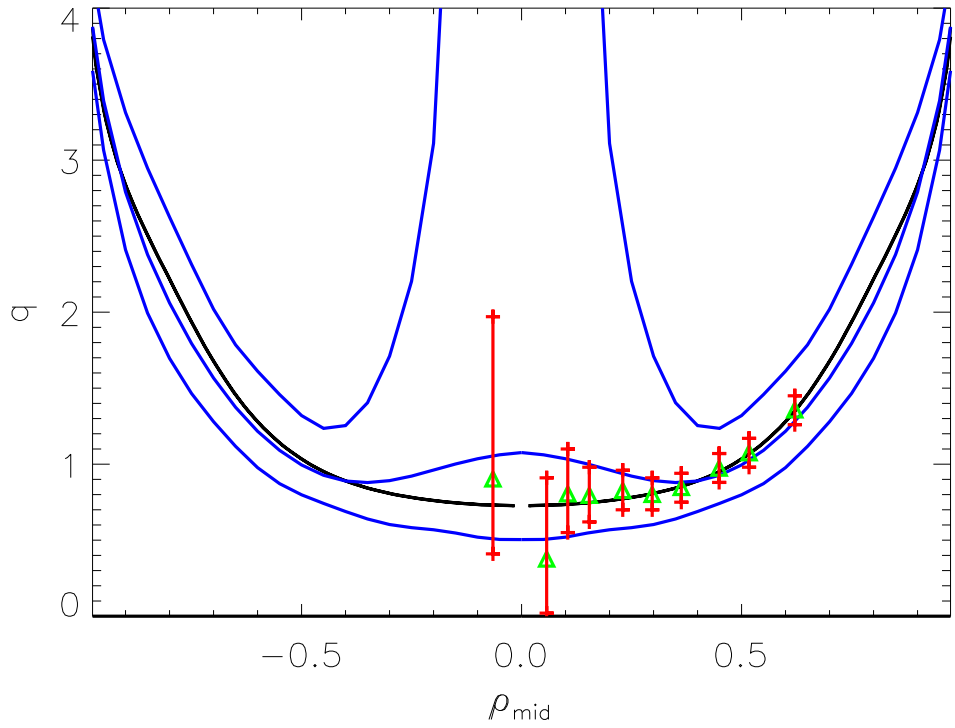

Figure 5.4: *Recovery of AUG q-profile for discharge 12077*

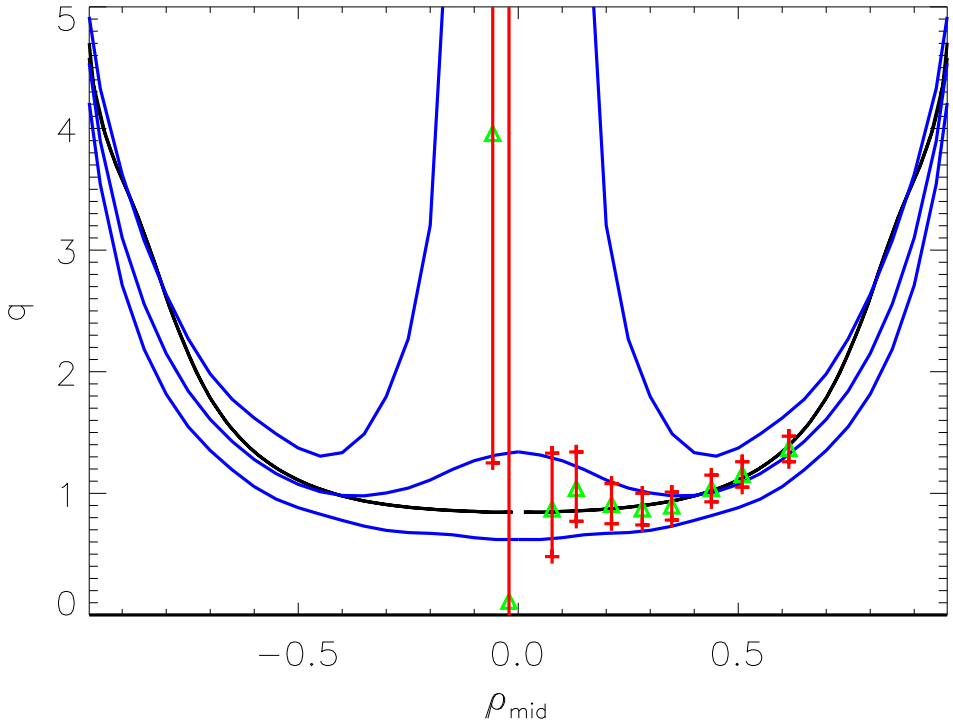

Figure 5.5: *Recovery of AUG q-profile for discharge 13012*

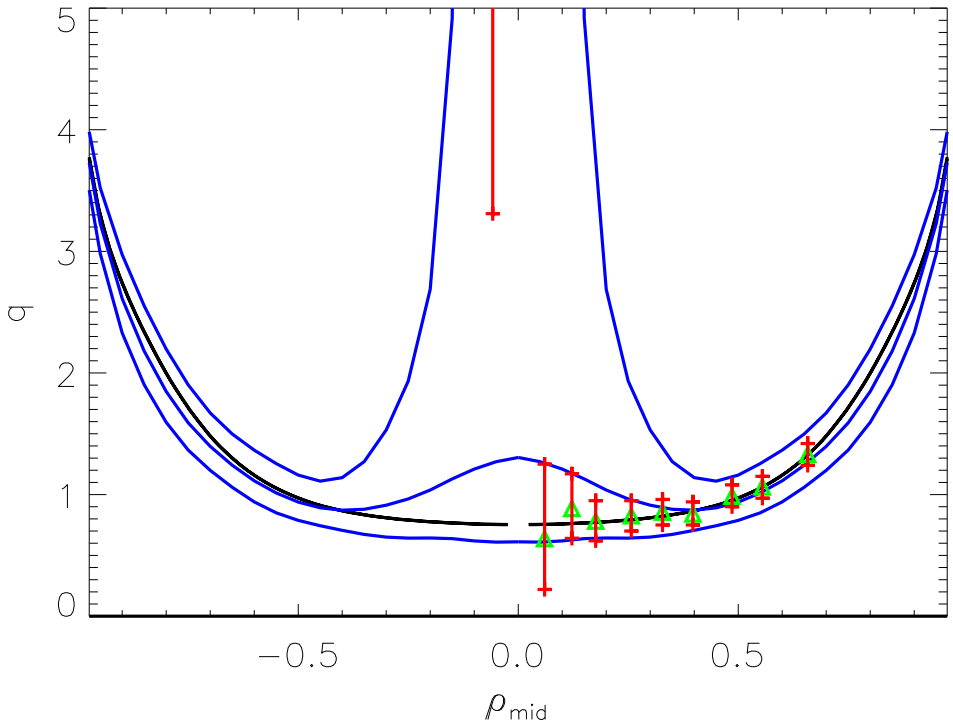

Figure 5.6: *Recovery of AUG q-profile for discharge 13049*

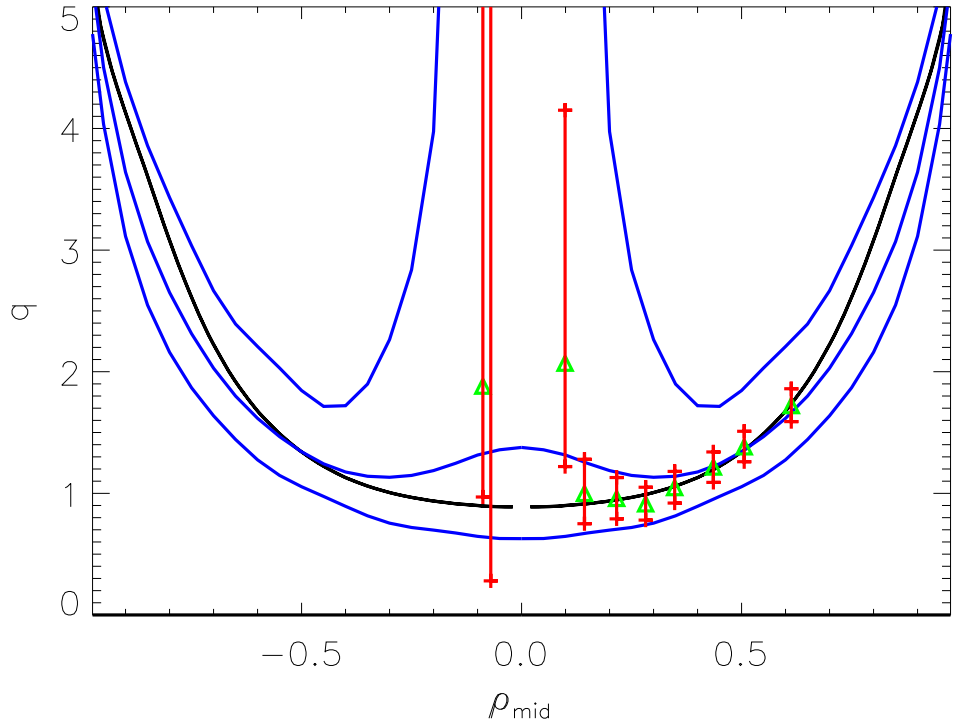

Figure 5.7: *Recovery of AUG q-profile for discharge 13169*

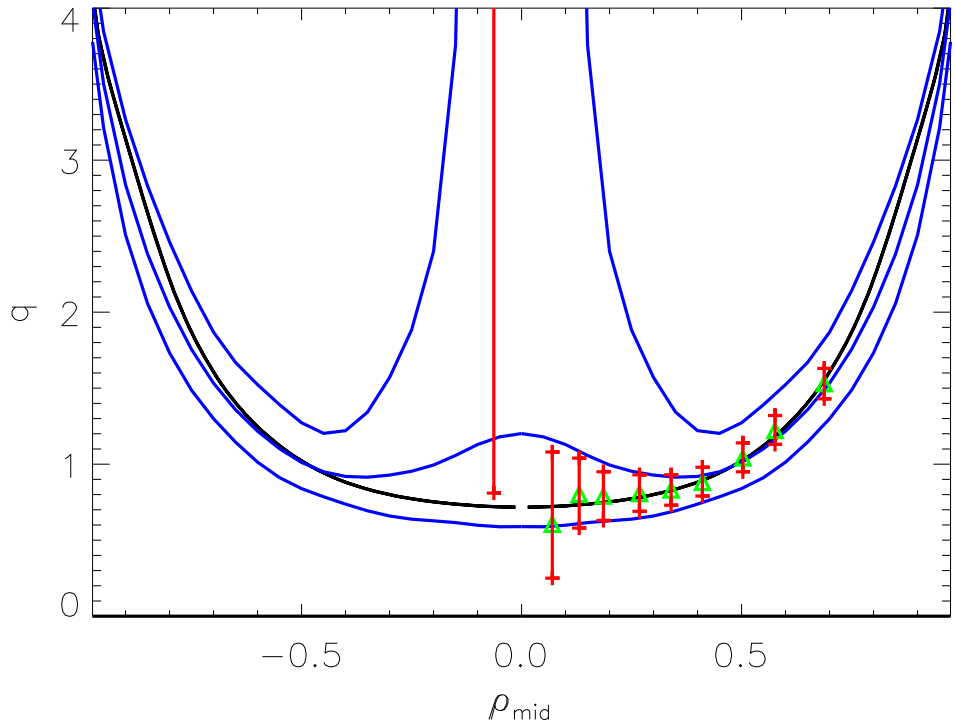

Figure 5.8: *Recovery of AUG q-profile for discharge 12952*

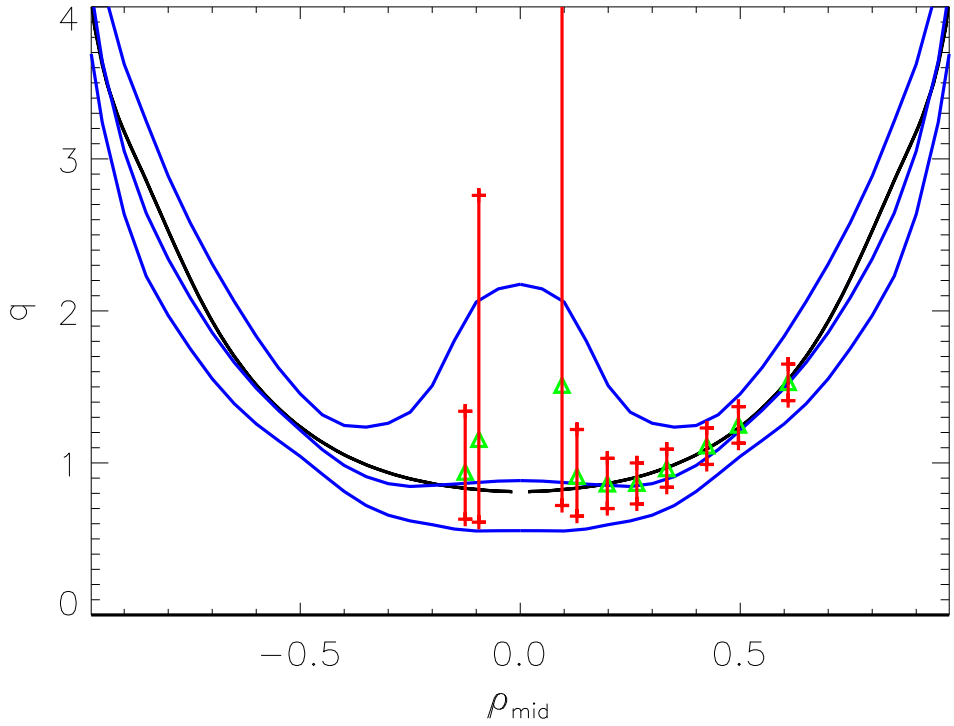

Figure 5.9: *Recovery of AUG q-profile for discharge 12036*

Improved H-mode recoveries Similar to the H-mode recoveries the single null lower divertor discharges improved H-mode discharges, discharges 13043 and discharge 13154, JANOS FPJ q-profile agrees with q_{exp} within the q_{exp} error bars. They also have slight reversed shear and the central JANOS FPJ error bars are off the scale of the figure. Discharge 13044 in Fig. 5.12 is a single null upper divertor discharge but as it a very early timepoint and in the current ramp up phase of the shot the q-profile has extremely large values when compared to improved H-mode discharges in flattop. In this case although the JANOS recovery agrees almost within q_{exp} error bars, there is a significant portion of the CLISTE q-profile between MSE channel 1 and the edge of the plasma which lies outside the JANOS FPJ error bars. Discharge 13099 in Fig. 5.13 is again a single null upper divertor plasma and as with similar plasmas in ordinary H-mode mode, the profile is slightly reversed agrees within q_{exp} error bars and the JANOS FPJ error bars are smaller than the equivalent category 4 JANOS FPJ error bars.

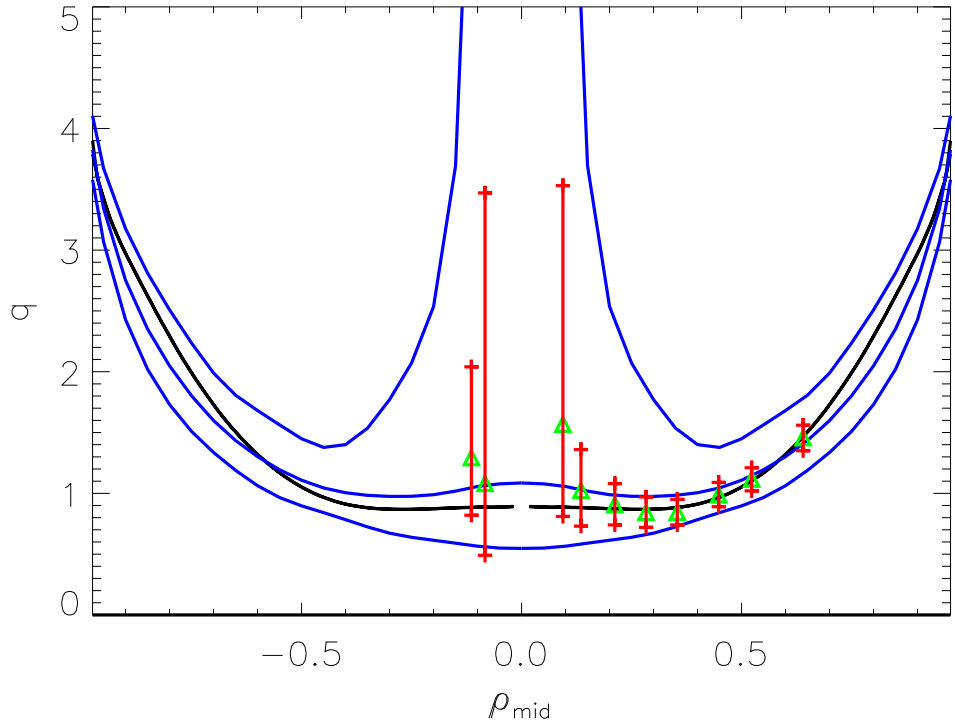

Figure 5.10: *Recovery of AUG q-profile for discharge 13043*

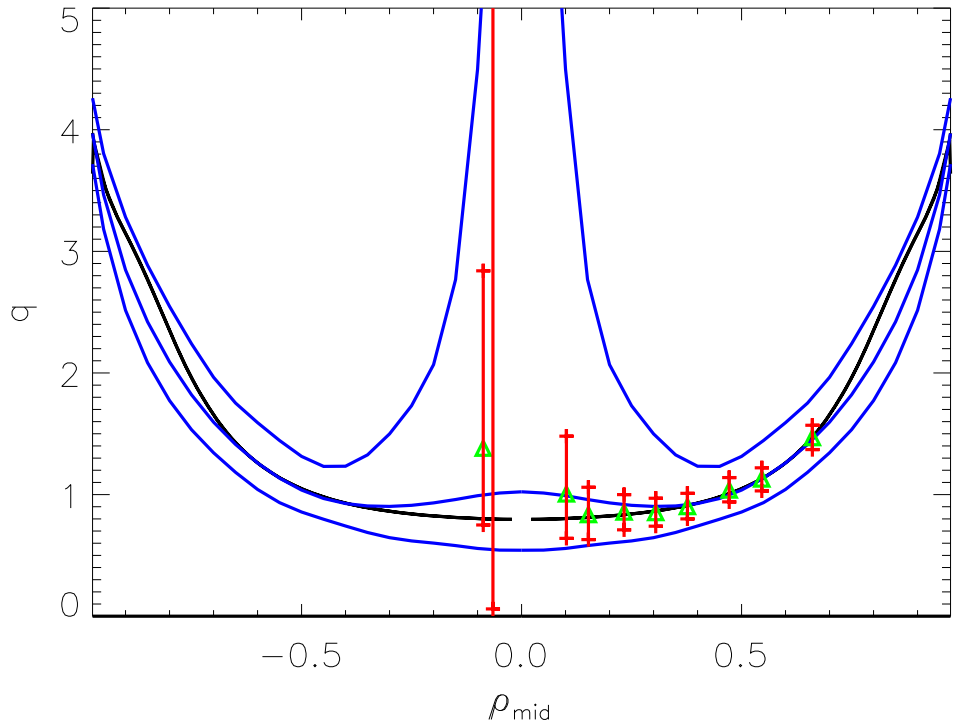

Figure 5.11: *Recovery of AUG q-profile for discharge 13154*

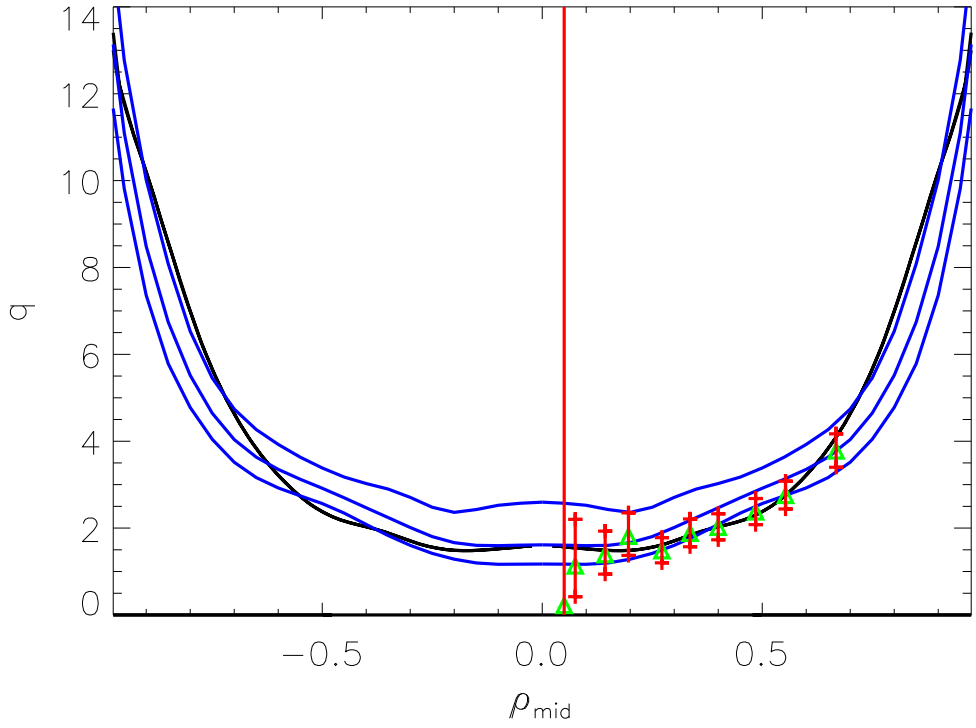

Figure 5.12: *Recovery of AUG q-profile for discharge 13044*

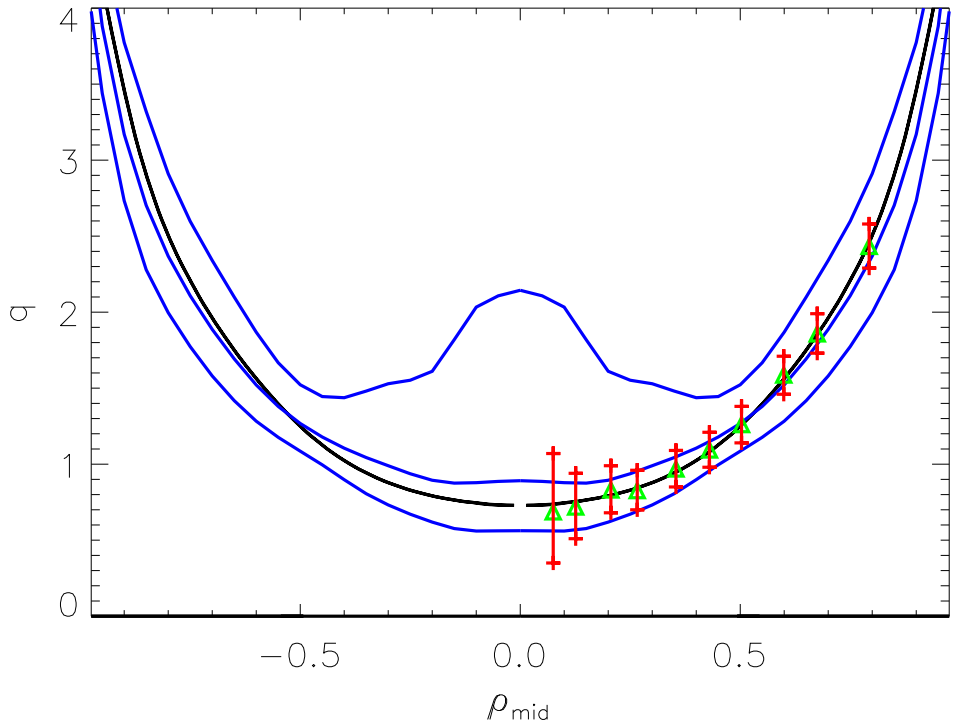

Figure 5.13: *Recovery of AUG q-profile for discharge 13099*

ITB recoveries The JANOS FPJ recovery of the first 4, Figs. 5.14- 5.17, ITB discharge's q-profiles agree, in general, within q_{exp} error bars. The exception being channel 8 in discharge 13130 in Fig. 5.15 which was already discussed in chapter 4. In each of these 4 recoveries, as in the JANOS FPJ recovery in discharge 13012, the CLISTE q-profile is either outside or close to the JANOS FPJ error bars in the plasma region between the outermost MSE channel and the region of the plasma when the magnetic diagnostic are able to recover the q-profile. Discharge 13130 in Fig. 5.15 shows the CLISTE q-profile outside the JANOS FPJ errors at the edge of the plasma where the accurate recovery of q_{95} depends on the magnetics measurements. Discharge 13108 in Fig 5.18 had unreliable MSE measurements in channels 8-10, these aside for the rest of the profile the JANOS q-profile and q_{exp} agree within error bars. For the first 4 ITB discharge there is good agreement between CLISTE and JANOS FPJ for the value of q_{min}. For All the ITB discharges there is good agreement between q_{exp} and JANOS FPJ and there is poor agreement between CLISTE and JANOS FPJ outside the last MSE channel. The database results in Figs. 5.1(i) show the database ι recovery is poorer for JANOS FPJ than PCA FPJ towards the edge the plasma. This indicates that the JANOS code is optimised to recover the q-profile which is spanned by of the MSE channels.

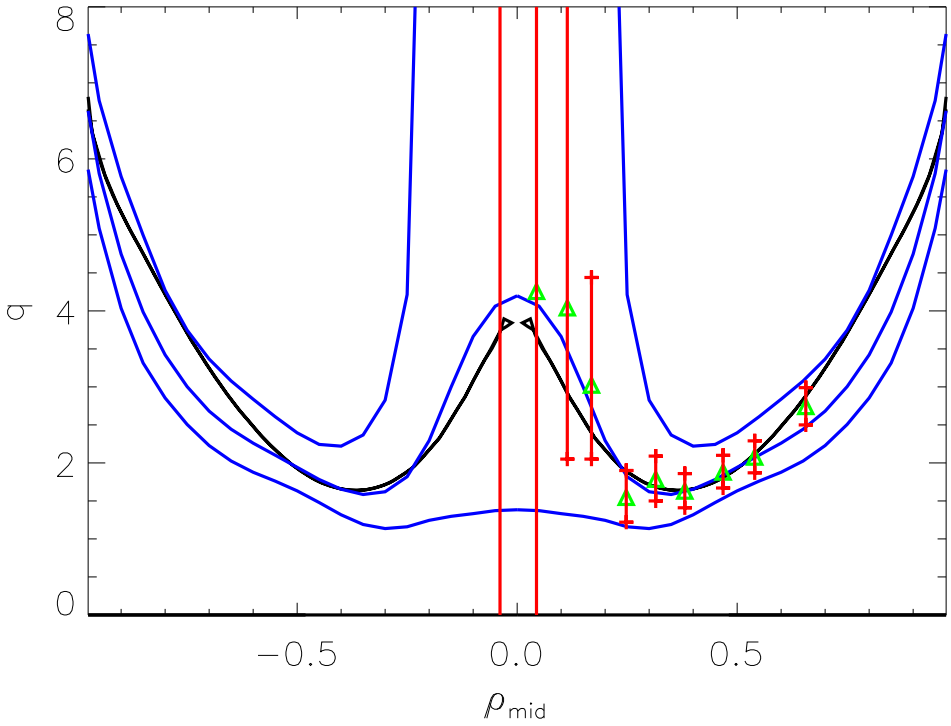

Figure 5.14: *Recovery of AUG q-profile for discharge 13225*

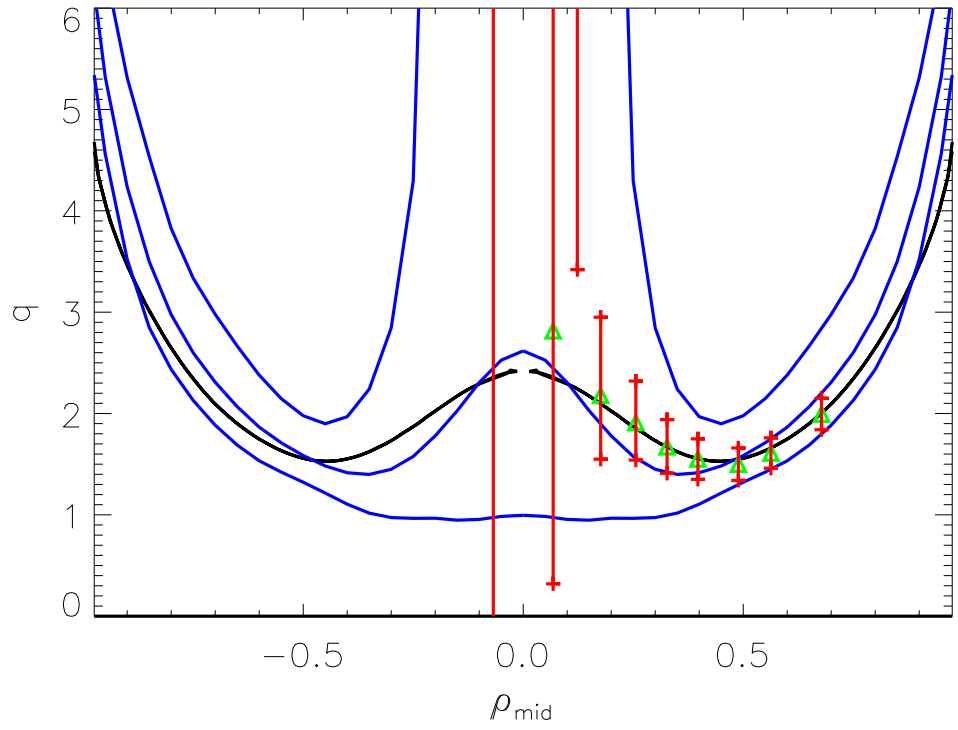

Figure 5.15: *Recovery of AUG q-profile for discharge 13130*

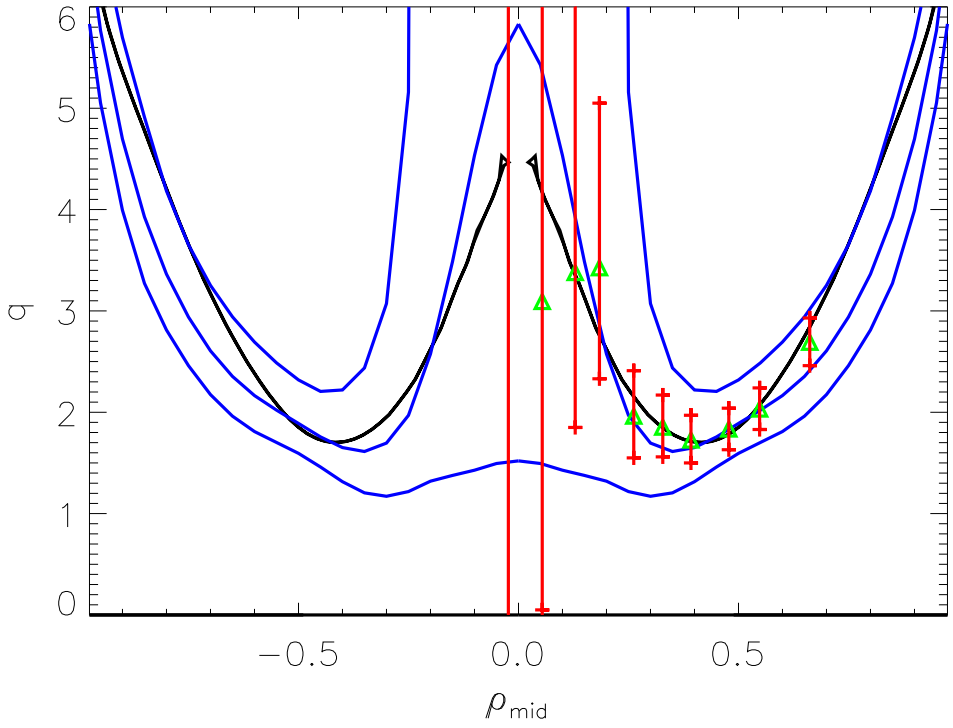

Figure 5.16: *Recovery of AUG q-profile for discharge 13148*

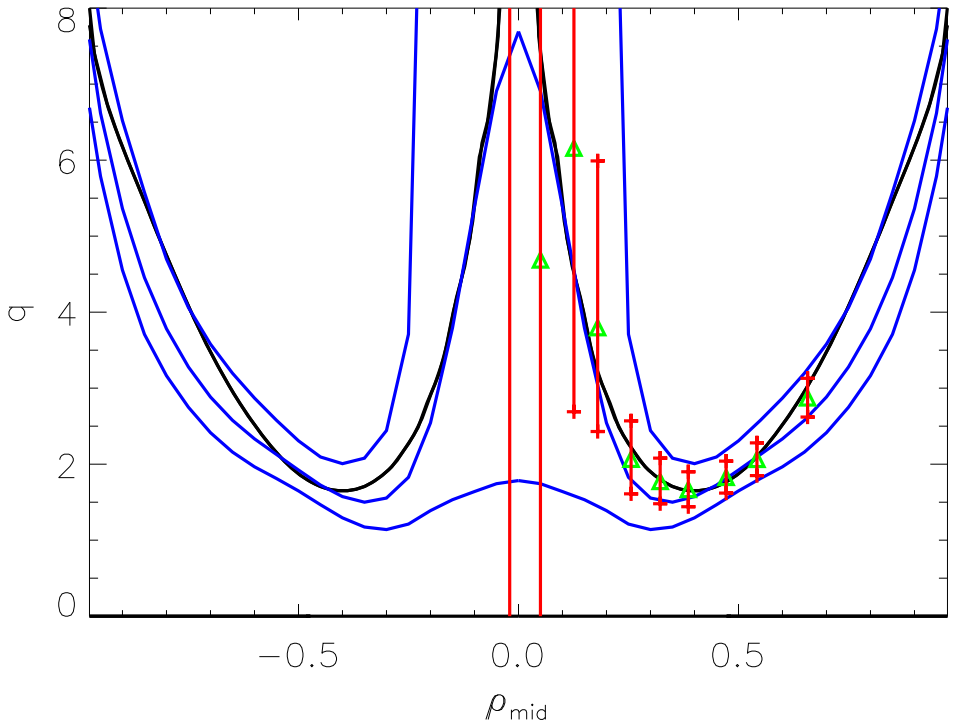

Figure 5.17: *Recovery of AUG q-profile for discharge 13149*

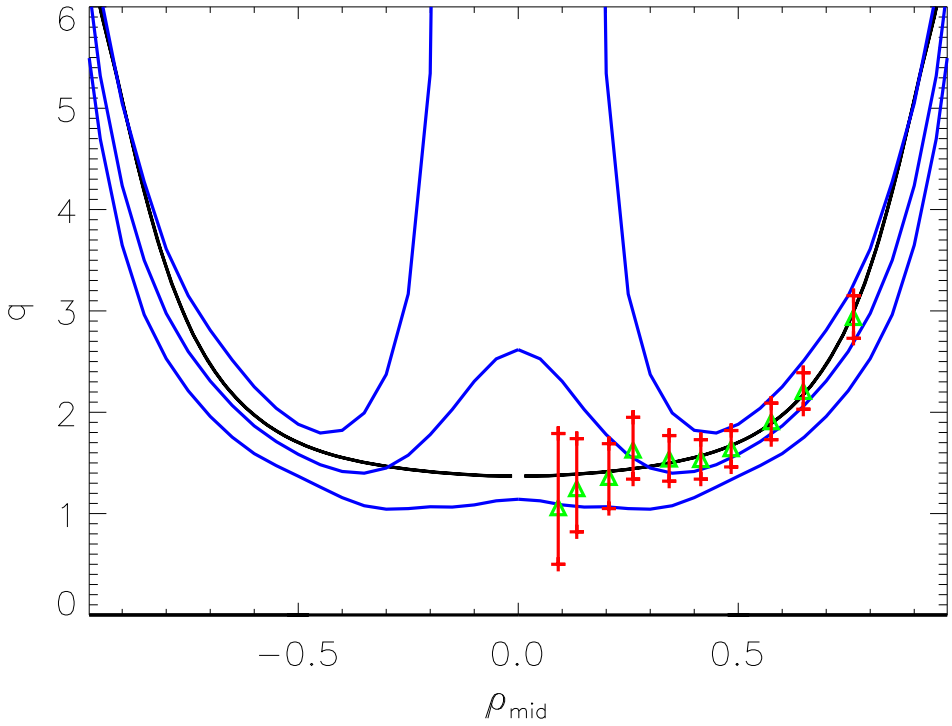

Figure 5.18: *Recovery of AUG q-profile for discharge 13108*

5.4.3 Summary of the JANOS FPJ and CLISTE q-profile Recoveries

As in section 4.5.2 it was decided not to present summary statistic of the AUG recoveries.

The general trends present included:

- As before the various scenarios, with variable I_p and $\mathbf{B}_\phi$, were well recovered.
- As before in general for reversed shear discharges the FPJ and CLISTE recoveries of q_{min} agreed within q_{exp} error bars.
- JANOS FPJ and the best possible PCA FPJ accurately recover AUG q-profiles in the region of the plasma spanned by the MSE channels, within experimental error.
- JANOS FPJ is seen to have difficulty in recovering the q-profile outside the region of the plasma spanned by the MSE channels.

5.4.4 Extended JANOS FPJ Confidence Limits Analysis

In this subsection the same test as in Section 4.5.3 is used to demonstrate what current density profiles are possible within FPJ confidence limits. Discharge 13154 is again used and the results are presented in Figs. 5.19 and Fig. 5.20. The JANOS FPJ error bar are wider than the best possible PCA FPJ recovery in the previous analysis so more database profiles fit within the JANOS FPJ error bars in Fig. 5.19 and the extra current density profiles are presented in Fig. 5.20.

In the central region of the plasma it is striking that although the JANOS FPJ error bars are very large but no database q-profile with large reversed shear fits within the profile. There are two possible reasons for this; it is possible that there are no reversed shear profiles in the database. The other possibility is that the very reversed shear cases fit within the JANOS error bars in the central region but these profile do not fit within the narrower JANOS FPJ error bars towards the edge of the plasma. This implies that if it were possible to take into account this lack of fit of reversed shear profiles towards the edge of the plasma it would be possible to narrow the central FPJ error bars.

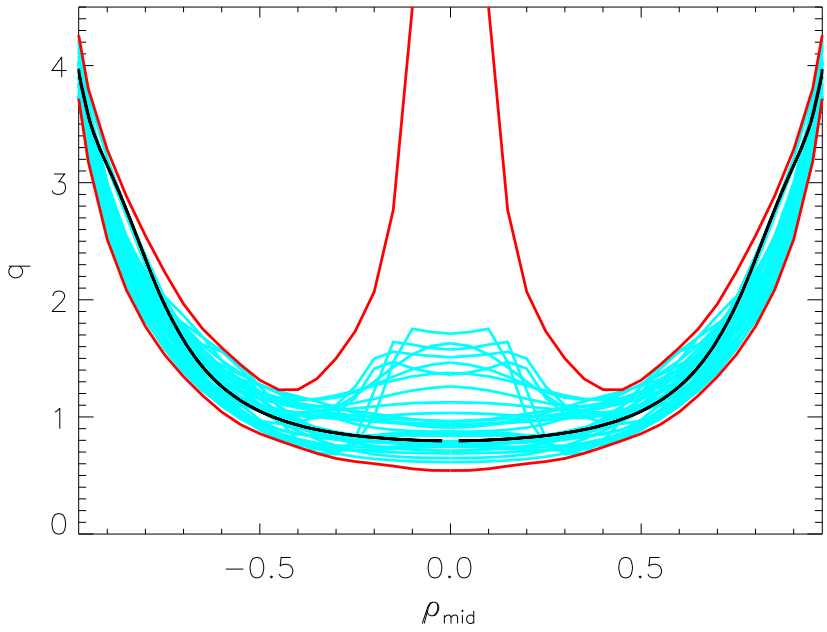

Figure 5.19: *CLISTE recovery (black line) and JANOS FPJ confidence limits (red line) of the q-profile for AUG discharge 13154. Also indicated are the simulated AUG equilibrium database q-profiles(cyan lines) which fit the profile within JANOS FPJ error limits.*

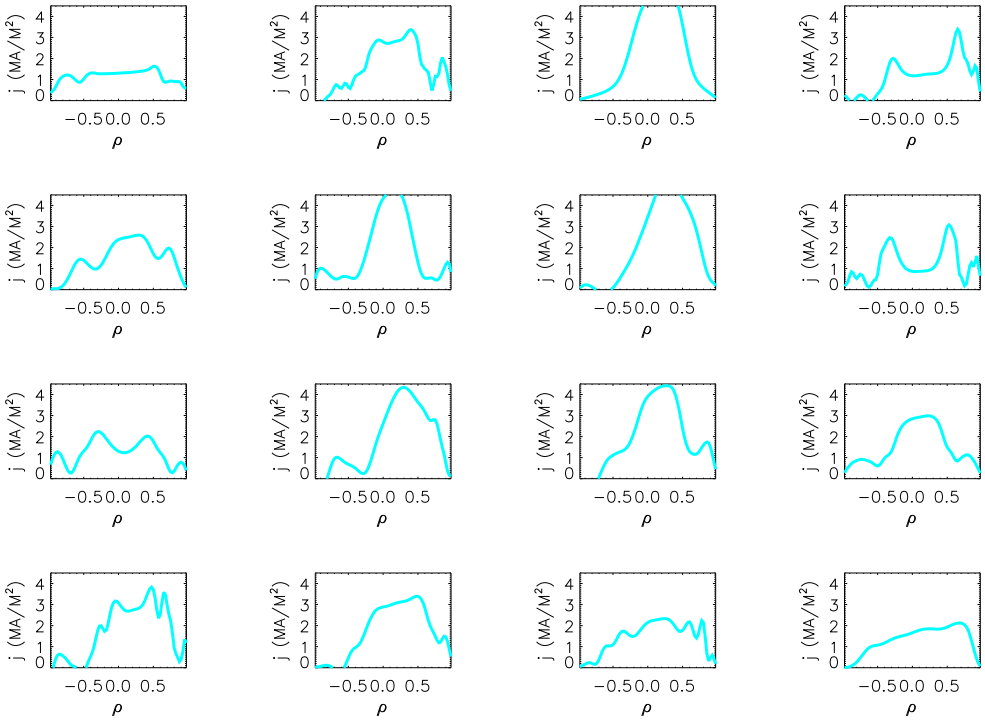

Figure 5.20: *Selection of the associated simulated AUG equilibrium database current density profile which fit within JANOS FPJ confidence limits for 13154*

Chapter 6

Conclusion

The principal theme of this work has being the integration of MSE diagnostic measurements into an FP model with the aim of accurate recovery of AUG's q-profile. A general description of the MSE diagnostic is given in chapter 1 along with an outline of the MSE diagnostic setup on AUG. A description of the FPJ model along with an outline of the database of simulated AUG equilibria on which it is based is given in chapter 3. Database q-profile recoveries are presented in this chapter. In chapter 4 a sample of AUG q-profiles recovered using a standard FPJ model is presented. In chapter 5 a novel FPJ approach, which optimises the model regressors to maximise the recovery of the ι profile, is presented along with a sample of AUG q-profiles are recovered using a this JANOS FPJ model.

It was shown that it is more correct to recover the ι-profile, the inverse of the q-profile, when using the MSE diagnostic measurements as the primary diagnostic in FPJ q-profile recovery. The q-profile is then found by inverting the ι-profile. The MSE diagnostic measurements are proportional to $\mathbf{B}_\theta$, as are local ι values for fixed flux surface topology. The q-profile is proportional to $1/\mathbf{B}_\theta$ and this relationship leads to heterscedastic error propagation when the recovery is dependent on the MSE diagnostic and is detrimental to the FPJ regression model.

Another difficulty encountered is that the MSE channels are fixed in space while the plasma's geometric position is variable, thus the position of the ι profile is variable. For this reason it was decided to recover the ι profile over ρ_{mid} co ordinates which are determined by by the flux surface topology, and are already reasonably determined by the magnetic measurements and thus the geometric position of each local ι value is known.

The MSE diagnostic measurements is proportional to $\mathbf{B}_\theta$ and $\mathbf{B}_\theta$ goes towards zero in the central region of the plasma. Thus there is a large error associated with the central MSE channels, and it is possible that if some of the MSE channels are close enough to the centre of the plasma the finite error in these measurements will give rise to infinite uncertainty. This phenomenom is demonstrated by the extremely large q_{exp} error bars in the AUG q-profile recoveries in chapter 4. As the MSE channels only span about 3cms in the vertical direction and as the position of the plasma is variable it is possible for the MSE channels to be distant from the centre of the plasma in which case it is not possible to accurately recover the central region of the q-profile due to the lack of MSE information.

From both the standard PCA and JANOS FPJ database recoveries of the ι profile it was demonstrated that the RMSE of the recoveries is worse towards the centre and more accurate towards the edge of the plasma. The very large errors in recovering ι in the central region of the plasma are dependent in part on the position of the plasma, i.e. whether the MSE channels are present in this region or not. By definition the FPJ RMSE is a database averaged error value. The FPJ confidence bands which were presented are based on this RMSE and thus for discharges with central MSE channels RMSE based FPJ confidence bands can be overly large. In future work this fact could be used to make more conservative FPJ confidence limits. Also work has been done, Appendix E, to try to take into account the vertical position of the magnetic axis in relation to the MSE channels. The results seem to suggest that a relationship is present but were not conclusive enough to include it the bulk of this thesis. The accuracy of q_{exp} in the AUG q-profile recoveries indicate that periodically, depending on the discharge, there is no useful information gained from the central MSE channels. This is a reason why the inclusion of such channels into the FPJ model must be questioned.

The JANOS 16 LCs based FPJ model compared well with the PCA 25 LCs based FPJ model when comparing the accuracy of the recovery of AUG q-profiles in the region spanned by the MSE channels. This bodes well for the JANOS model. A negative aspect of JANOS was the apparent difficulty this model had in recovering the edge q-profile. It should be noted that the AUG FPG (magnetic only recovery of plasma parameters) had difficulty in recovering q_{95} with only 16 LCs for this database, which differed from previous databases in that it has a much greater number of free parameters in the two

source profiles for the Grad-Shafranov equation. This ,along with the fact that the JANOS FPJ LCs also include MSE measurements, implies that more than 16 LCs are needed to accurately recover the outer q-profile.

Appendix A

Derivation of the Grad-Shafranov Equation

Derivations of the Grad-Sarfanov equation can be found in any fusion orientated plasma physics textbooks. This derivation can be found in [62].

The basic strategy of the derivation is first to exploit the axisymmetry in order to deduce the general structure of the magnetic field via the equation $\nabla \cdot \mathbf{B} = 0$. This enables the field to be expressed in terms of a gradient of a scalar flux function. This representation of the field is then substituted into the equilibrium equation $\mathbf{J} \times \mathbf{B} = \nabla p$. The two prescribed arbitrary functions correspond to the pressure gradient and a function which is a measure of the total plasma current in cylindrical coordinates (r, ϕ, z).

This gives

$$\nabla \cdot \mathbf{B} = \frac{1}{r}\frac{\partial (r\mathbf{B}_r)}{\partial r} + \frac{\partial \mathbf{B}_z}{\partial z} + \frac{1}{r}\frac{\partial \mathbf{B}_\phi}{\partial \phi} = 0.$$

By the assumption of axisymmetry, we have $\frac{\partial}{\partial \phi} = 0$, and so $\mathbf{B} = \mathbf{B}(r, z)$ only. This allows us to introduce a flux function to represent the field components in the poloidal plane,

$$r\mathbf{B}_r = \frac{\partial \psi}{\partial z} \qquad and \qquad \mathbf{B}_z = -\frac{\partial \psi}{\partial r}$$

or, more succinctly,

$$\mathbf{B} = \frac{1}{r}\nabla\psi \times \hat{e}_\phi + \mathbf{B}_\phi \hat{e}_\phi \tag{A.1}$$

Having obtained the field, the plasma current can now be calculated using Ampere's law. The components of the current are

$$\mu_0 \mathbf{J}_r = \frac{\partial \mathbf{B}_\phi}{\partial z}, \quad \mu_0 \mathbf{J}_z = -\frac{1}{r}\frac{\partial (r\mathbf{B}_\phi)}{\partial r}, \quad \mu_0 \mathbf{J}_\phi = \frac{\partial}{\partial r}\left(\frac{1}{r}\frac{\partial \psi}{\partial r}\right) - \frac{1}{r}\frac{\partial^2 \psi}{\partial z^2}, \tag{A.2}$$

On grouping the poloidal and toroidal components of the current, this may be written more compactly as

$$\mu_0 \mathbf{J} = \frac{1}{r}\nabla(r\mathbf{B}_\phi) \times \hat{e}_\phi - \frac{1}{r}\triangle^* \psi \hat{e}_\phi \tag{A.3}$$

with $\triangle^*$ representing the differential operator in this coordinate system.

$$\triangle^* \equiv r^2 \nabla \cdot \{\frac{1}{r^2}\nabla\} \equiv r\frac{\partial}{\partial r}\{\frac{1}{r}\frac{\partial}{\partial r}\} + \frac{\partial^2}{\partial z^2} \tag{A.4}$$

Now the expression for the magnetic field given in Eqn. A.1 and the current Eqn. A.3 are substituted into the equilibrium Eqn. 1.20 $\mathbf{J} \times \mathbf{B} = \nabla p$. Specifically, if we examine the ϕ-component of the equilibrium equation, and once more appeal to axisymmetry,

$$(\mathbf{J} \times \mathbf{B}) \cdot \hat{e}_\phi = \nabla p \cdot \hat{e}_\phi = 0 \tag{A.5}$$

or

$$\{\frac{1}{\mu_0 r}\frac{\partial (r\mathbf{B}_\phi)}{\partial r}\}\{\frac{1}{r}\frac{\partial \psi}{\partial z}\} - \{\frac{1}{\mu_0 r}\frac{\partial (r\mathbf{B}_\phi)}{\partial z}\}\{\frac{1}{r}\frac{\partial \psi}{\partial r}\} = 0 \tag{A.6}$$

This states that the Jacobian of the function $r\mathbf{B}_\phi/\mu_0$ and ψ is zero. The vanishing of the Jacobian implies that $r\mathbf{B}_\phi/\mu_0 = F(\psi)$. Now use the fact that the field lines lie in isobaric surfaces:

$$\mathbf{B} \cdot \nabla p = \frac{1}{r}\nabla\psi \times \hat{e}_\phi \cdot (\nabla p)_{pol} = \frac{1}{r}\frac{\partial \phi}{\partial r}\frac{\partial p}{\partial z} - \frac{1}{r}\frac{\partial \phi}{\partial z}\frac{\partial \phi}{\partial r} = 0 \tag{A.7}$$

which is the Jacobian of ϕ and p, hence $p = p(\psi)$. If we now write down the r-component of the equilibrium equation:

$$(\mathbf{J} \times \mathbf{B}) \cdot \hat{e}_r = \frac{\partial p}{\partial r} = -\{\frac{1}{\mu_0 r}\frac{\partial (r\mathbf{B}_\phi)}{\partial r}\}\mathbf{B}_\phi - \frac{1}{\mu_0 r}\triangle^* \psi \{\frac{1}{r}\frac{\partial \psi}{\partial r}\} \tag{A.8}$$

Using the fact that both p and $r\mathbf{B}_\phi$ are function of ψ we get the Grad-Shafranov equation

$$\frac{dp(\psi)}{d\psi}\frac{\partial \psi}{\partial r} = -\frac{1}{r}\frac{dF(\psi)}{d\psi}\frac{\partial \psi}{\partial r}\left(\frac{\mu_0 F(\psi)}{r}\right) - \frac{1}{\mu_0 r}\triangle^* \psi \frac{1}{r}\frac{\partial \psi}{\partial r}, \tag{A.9}$$

which can be presented in the more familiar terms of Eqn.1.27

$$-\triangle^* \psi = \mu_0 r^2 p'(\psi) + f f'(\psi)$$

Appendix B

$\mathbf{B}_\phi$ and the Grad-Shafranov equation:

The purpose of this appendix is to demonstrate that the Grad-Shafranov G-S equation is independent of $\mathbf{B}_{\phi_{\mathbf{vac}}}$ [33]. From the scaled G-S Eqn., where $\psi \to \alpha\psi$,

$$-\alpha\triangle\psi = \mu_0 R^2 \frac{1}{\alpha}\frac{d}{d\psi}p(\alpha\psi) + \frac{1}{2\alpha}\frac{d}{d\psi}F^2(\alpha\psi) \tag{B.1}$$

is seems obvious that to preserve the equilibrium $p(\alpha\psi) = \alpha^2 p(\psi)$ and $F^2(\alpha\psi) = \alpha^2 F^2(\psi)$ thus $F(\alpha\psi) = \alpha F(\psi)$. This is indeed true for $p(\psi)$ which does scale with the square of the plasma current when the profile shape is unaltered and $\mathbf{B}_\theta$ is conserved. However $F^2(\psi)$ is an affine function and thus scales differently. $F^2(\psi)$ can be written

$$F^2(\psi) = F_0^2 + \delta F^2_{plasma}(\psi) \tag{B.2}$$

where $F_0 = R\ \mathbf{B}_{\phi_{\mathbf{vac}}}$ is the constant value of F and the plasma contribution $\delta F^2_{plasma}(\psi)$ is given by

$$\delta F^2_{plasma}(\psi) = 2\int_0^\psi ff'(\psi)d\psi \tag{B.3}$$

where ff' is one of the G-S's source profiles. Like $p(\psi)$, the plasma contribution $\delta F^2(\psi)$ scales with α^2. The vacuum contribution F_0^2 scales with the square of $\mathbf{B}_{\phi_{\mathbf{vac}}}$. Let $\psi \to \alpha\psi$ and $\mathbf{B}_{\phi_{\mathbf{vac}}} \to \beta\ \mathbf{B}_{\phi_{\mathbf{vac}}}$, now

$$F(\alpha\psi, \beta\mathbf{B}_{\phi_{\mathbf{vac}}}) = \sqrt{\beta^2 F_0^2 + \alpha^2 \delta F^2(\psi)} \tag{B.4}$$

Differentiating w.r.t. ψ yields

$$F'(\alpha\psi, \beta\mathbf{B}_{\phi_{\mathbf{vac}}}) = \frac{\alpha^2 ff'(\psi)}{\sqrt{\beta^2 F_0^2 + \alpha^2 \delta F^2(\psi)}} \tag{B.5}$$

Multiplying Eqn. B.4 by Eqn. B.5 gives

$$\frac{1}{2\alpha}\frac{d}{d\psi}F^2(\alpha\psi,\beta\mathbf{B}_{\phi_{\mathbf{vac}}}) \equiv \frac{1}{\alpha}F(\alpha\psi,\beta\mathbf{B}_{\phi_{\mathbf{vac}}})F'(\alpha\psi,\beta\mathbf{B}_{\phi_{\mathbf{vac}}}) = \alpha f f'(\psi) \qquad \text{(B.6)}$$

as required to preserve the equilibrium under the scaling in Eqn. B.1. Thus the product $F(\alpha\psi,\beta\mathbf{B}_{\phi_{\mathbf{vac}}})F'(\alpha\psi,\beta\mathbf{B}_{\phi_{\mathbf{vac}}})$ is identical with $\mathbf{B}_{\phi_{\mathbf{vac}}}$ independent source function $ff'(\psi)$ and hence the Grad Shafranov equation is independent of $\mathbf{B}_{\phi_{\mathbf{vac}}}$.

Appendix C

CLISTE Interpretive Equilibrium Code

Overview The following appendix is reproduced from [27] and is meant to serve as a brief introduction to the CLISTE code. CLISTE is an acronym for CompLete Interpretive Suite for Tokamak Equilibria. The CLISTE code finds a numerical solution to the Grad-Shafranov equation 1.27 for a given set of poloidal field coil currents and limiter structures by varying the free parameters in the parameterization of the $p'(\psi)$ and $FF'(\psi)$ source profiles which define the toroidal current density profile j_ϕ so as to obtain a best fit in the least squares sense to a set of experimental measurements. These measurements can include external magnetic data, MSE data, kinetic data, SXR measurements, etc..., and the free parameters are varied such that the cost function, i.e. the squared modulus of the vector of (weighted) differences between the set of experimental measurements and those predicted by the equilibrium solution, is minimised.

CLISTE Algorithm: During each iteration cycle, a linear optimisation of the free parameters in the $p'(\psi)$ and $FF'(\psi)$ profiles is carried out. The linear parameterization of the source profiles is given by

$$p'(\psi) = \sum_{i=1}^{m_p} c_i \pi_i(\psi) \tag{C.1}$$

$$FF'(\psi) = \sum_{j=1}^{m_{FF}} d_j \varphi_j(\psi) \tag{C.2}$$

where $\pi_i(\psi)$ and $\varphi_j(\psi)$ are arbitrary functions of ψ with fixed coefficients and c_i, d_j are the free parameters in the problem. Thus $\pi_i(\psi)$ and $\varphi_j(\psi)$ constitute the basis functions of the plasma current distribution where ψ is the full equilibrium flux function from the previous iteration cycle. New poloidal flux functions $\psi_{p,i}^{new}$ and $\psi_{FF,i}^{new}$ are found from the updated equilibrium flux function after solving the 'Poisson problem'

$$-\left(\frac{\delta^2\psi_{p,i}^{new}}{\delta R^2} - \frac{1}{R}\frac{\delta\psi_{p,i}^{new}}{\delta R} + \frac{\delta^2\psi_{p,i}^{new}}{\delta Z^2}\right) = \mu_0 R^2 \pi_i(\psi)$$

$$-\left(\frac{\delta^2\psi_{FF,j}^{new}}{\delta R^2} - \frac{1}{R}\frac{\delta\psi_{FF,j}^{new}}{\delta R} + \frac{\delta^2\psi_{FF,j}^{new}}{\delta Z^2}\right) = \varphi_j(\psi) \qquad \text{(C.3)}$$

separately for each $\psi_{p,i}^{new}$ and $\psi_{FF,j}^{new}$. Note that Eqn.C.3 takes care only of that part of the updated equilibrium flux generated by th plasma current distribution. The full equilibrium flux also includes the contribution from the external measured currents, which are held constant. In terms of the as yet undetermined coefficients c_i and d_j, the updated full equilibrium flux is given by

$$\psi^{new} = \sum_{i=1}^{m_p} c_i \psi_{p,i}^{new} + \sum_{j=1}^{m_{FF}} d_j \psi_{FF,j}^{new} + \psi^{ext} \qquad \text{(C.4)}$$

The solution grids for $\psi_{p,i}^{new}$ and $\psi_{FF,j}^{new}$ yielded by Eqn. C.3 are passed individually to the routine which calculates the predicted measurements from the flux function. In this way, a matrix of $m_p + m_{FF}$ columns of 'basis values' $b_{n,k}, ((n = 1, ..., N_m), k = 1, ..., m_p + m_{FF})$ is constructed for N_m measurements. The values of $b_{n,k}$ is the contribution to the nth measurement prediction per until strength of the kth basis function. An extra column catering for the vertical shift parameter is added to the matrix by calculating the change in each measurement when its Z position is shifted by -1cm. This gives the sensitivity per +1cm shift in the plasma vertical position. An additional row is added to the matrix for each regularisation condition on the free parameters. If $\mathbf{B}$ is the data matrix and $\mathbf{y}$ is the vector of measurements less all the contributions from the measured external currents, then the optimisation problem reduces to solving the linear regression

$$\mathbf{y} = \mathbf{B}.\alpha \qquad \text{(C.5)}$$

where α is the solution vector of optimised free parameters for the present iteration cycle. The equation for y_n in the overdetermined system of linear equations which constitutes the linear regression problem is thus

$$y_n = \sum_{k=1}^{m_p+m_{FF}+1} \alpha_k b_{n,k} \tag{C.6}$$

Once α is determined, the full equilibrium flux grid is constructed. The plasma flux function ψ_{plas} is computed by once more solving Eqn. C.3 where the right-hand side now is the full $\mu_0 j_\phi$ profile constructed from the first $m_p + m_{FF}$ elements of the newly obtained α vector:

$$-\left(\frac{\delta^2\psi_{plas}}{\delta R^2} - \frac{1}{R}\frac{\delta\psi_{plas}}{\delta R} + \frac{\delta^2\psi_{plas}}{\delta Z^2}\right) = \mu_0 R^2 \sum_{i=1}^{m_p} c_i \pi_i(\psi) + \sum_{j=1}^{m_{FF}} d_j \varphi_j(\psi) \tag{C.7}$$

Finally the external flux contribution ψ_{ext} is restored to yield $\psi_{new} = \psi_{plas} + \psi_{ext}$. The entire procedure is iterated until a user-specified convergence criterion is satisfied. For a more detail description, refer to [27].

Appendix D

Mahalanobis Transformation:

From Eqn. 2.3 it follows that the covariance matrix for the $n \times p$ $\mathbf{X}$ matrix can be defined as

$$\mathbf{S_x} = \frac{1}{n}\sum_{i=1}^{n}(x_i - \bar{\mathbf{x}})(x_i - \bar{\mathbf{x}})'. \tag{D.1}$$

Note that this matrix can be equivalently defined as

$$\mathbf{S_x} = n^{-1}\mathbf{X'X} - \bar{\mathbf{x}}\bar{\mathbf{x}}' = n^{-1}(\mathbf{X'X} - n^{-1}\mathbf{X'II'X}). \tag{D.2}$$

Eqn. D.3 can be rewritten as

$$\mathbf{S_x} = n^{-1}\mathbf{X'HX} \tag{D.3}$$

where

$$\mathbf{H} = \mathbf{I} - n^{-1}\mathbf{II'}. \tag{D.4}$$

$\mathbf{H}$ is called the centring matrix and is symmetric and idempotent ($\mathbf{H^2} = \mathbf{H}$) this implies that $\mathbf{S}$ is positive semi-definite ($\mathbf{S} \geq 0$).

Consider the linear transformation

$$\mathbf{Y} = \mathbf{XA'} \tag{D.5}$$

where $\mathbf{A}$ is a $q \times p$ transformation matrix. The covariance matrix $\mathbf{S_y}$ is given by

$$\mathbf{S_y} = \frac{1}{n}\mathbf{Y'HY} = \frac{1}{n}\mathbf{AX'HXA'} = \mathbf{AS_xA'}. \tag{D.6}$$

The Mahalanobis transformation is a linear transformation where

$$\mathbf{A} = \mathbf{S_x}^{-\frac{1}{2}}. \tag{D.7}$$

The covariance matrix of the Mahalanobis transformation is

$$\mathbf{S_y} = \mathbf{S_x}^{-\frac{1}{2}}\mathbf{S_x}\mathbf{S_x}^{-\frac{1}{2}} = \mathbf{I}. \tag{D.8}$$

So the Mahalanobis transformation eliminates the correlation between the variables and standardises the variance of each variable.

Appendix E

Variation of $\triangle \iota$ w.r.t. position of Z_{mag}

As the MSE channels are fixed in space the accuracy of the FPJ recovery of the ι profile, and hence the q profile, depends on the position of these channels relative to the plasma position. The MSE channels span 31.9 cm in the horizontal direction which, for an average tokamak plasma equates to $\rho_{mid} = 0 \rightarrow .7$. But the MSE channels only span 3.2 cm in the vertical direction and a vertical displacement of the magnetic axis away from the MSE channels leads to a large added uncertainty in the recovery of the inner ι or q profiles.

The large database variation in the vertical position of the magnetic axis Z_{mag}, see Figs. E.1, E.2 , leads to an increase in the regression RMSE of each fixed ρ_{mid} ι regression. This problem was explored by segregating analysis of the regression residuals using Z_{mag}. For each ι regression the residuals are sorted into groups by Z_{mag} and the 'local' RMSE found. For category 3 plasmas, although the $\triangle \iota$ are not monotonically increasing, there is a definite trend of increasing $\triangle \iota$ away from the position of the MSE channels (Z $\approx$0cm) in Fig. E.1. For category 4 plasma the trend is more pronounced with a definite global minimum of $\triangle \iota$ situated at position of the MSE channels in Fig. E.2. The author acknowledges that the analysis of the variation of $\triangle \iota$ w.r.t. Z_{mag} is not complete but the aim of this appendix is to outline that more accurate error analysis is possible with the inclusion of the variation of $\triangle \iota$ w.r.t. Z_{mag}.

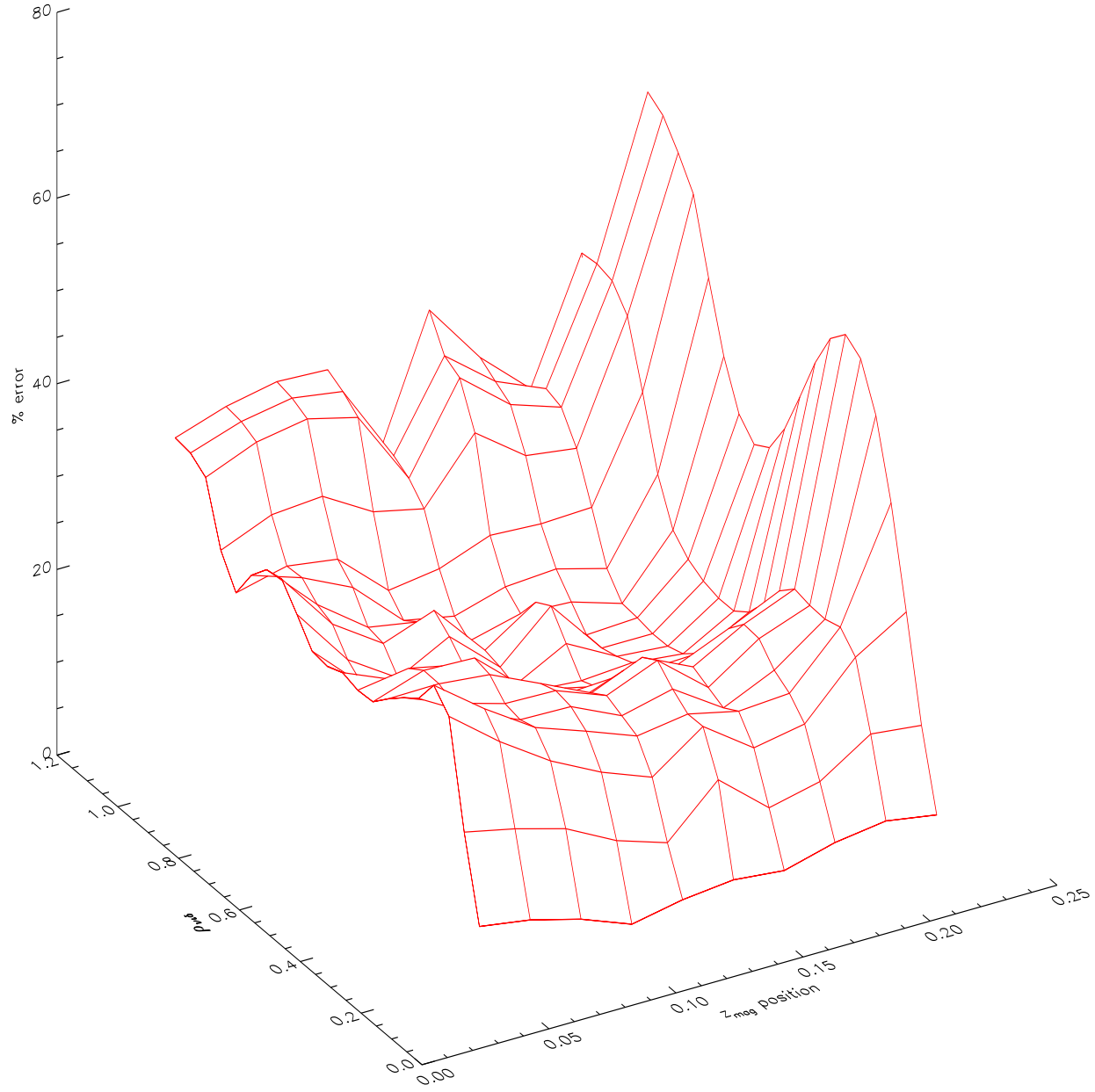

Figure E.1: *3-D illustration of the variation of* $\triangle t$ *w.r.t. the position of* Z_{mag} *along* ρ_{mid} *for category 3 database plasmas*

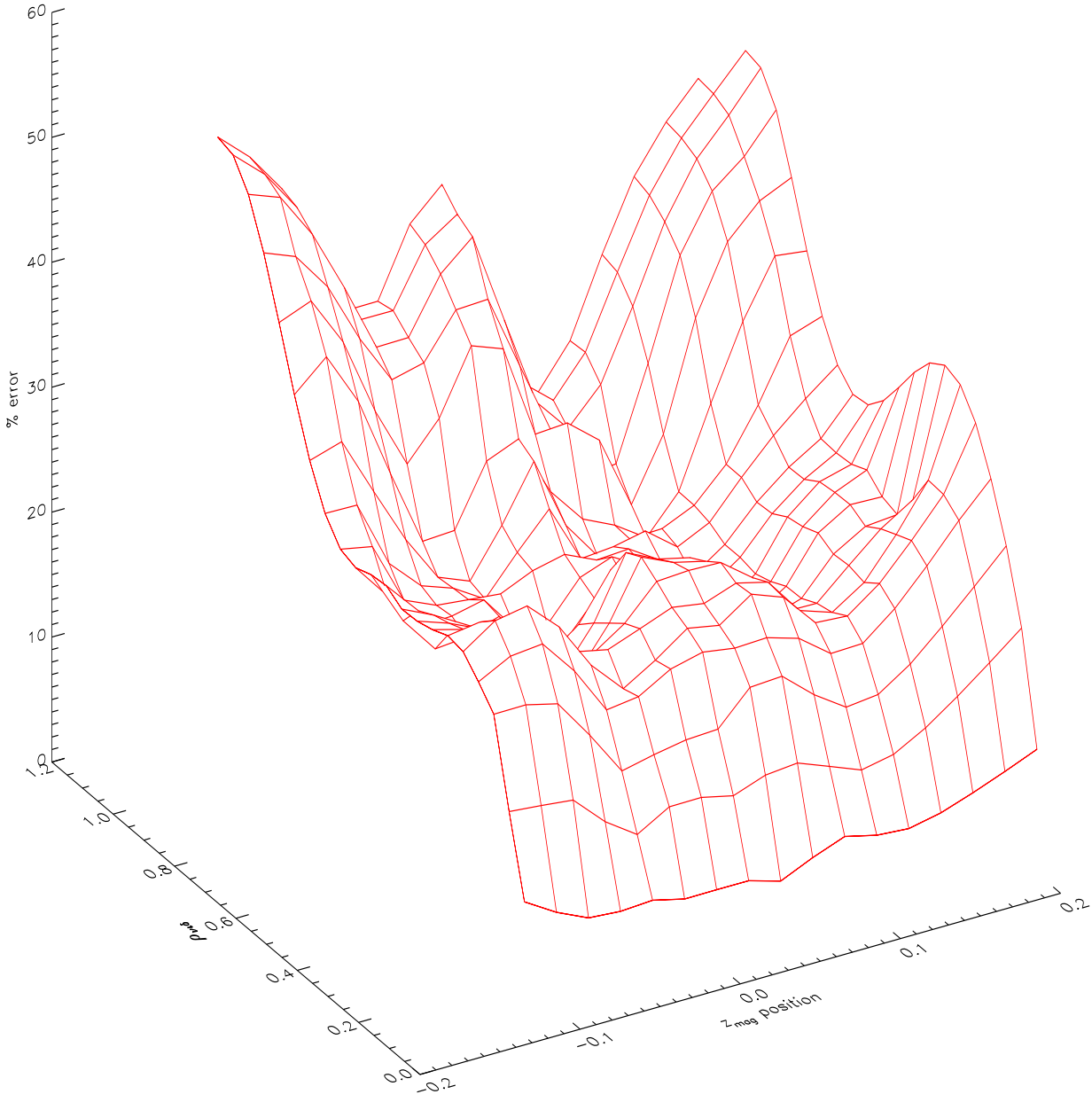

Figure E.2: *3-D illustration of the variation of* $\triangle t$ *w.r.t. the position of* Z_{mag} *along* ρ_{mid} *for category 4 database plasmas*

Bibliography

[1] Joos F. "The Atmospheric Carbon Dioxide Perturbation", Europhysics News, **27**, 6, 213-218, 1996

[2] Ongena J. "Energy for Future Centuries; Will Fusion be an Inexhaustible Safe and Clean Energy Source ", Transactions of Fusion Technology, **37**, 3, 2000

[3] U.S. department of energy, energy information administration "International Energy Annual 2002", 2002
website: http://www.eia.doe.gov/emeu/iea/

[4] Mac Kenzie J., "Estimated Ultimately Recoverable (EUR) oil", website: http://www.wri.org, World Resources Institute, 2000

[5] Woodward D., "2020 Vision, a Look at the Oil Industry in the 21^{st} Century", Middle east well evaluation review, 1993

[6] Population division of the department of economic and social affairs of the United Nations Secretariat
"World Population Prospects: The 2000 Revision", 2000
"World Urbanisation Prospects: The 2001 Revision", 2001
website: http://www.esa.un.org/unpp

[7] Wesson J., "Tokamaks" second edition, Clarendon Press, Oxford, 1997

[8] McCarthy P.J. "An Integrated Data Interpretation System for Tokamak Discharges", PhD thesis, University College Cork, Cork, 1992

[9] Callaghan H., "Stellarator Equilibrium Reconstruction by Function Parameterization", PhD thesis, University College Cork, Cork, 1999

[10] Braams B.J., "Computational Studies in Tokamak Equilibrium and Transport", PhD thesis, Utrecht, 1986

[11] Wolf R., "Measurement of Local Magnetic Field Inside a Tokamak Plasma (JET) by Means of the Motional Stark Effect and Analysis of the Internal Magnetic Field Structure and Dynamics",PhD thesis, Universitaet Duesseldorf, Duesseldorf, 1993

[12] Hendricks C.D., "Laser Driven Inertial Confinement Fusion: Principles and Implementation", Graduate seminar, Dept. electrical and computer engineering, University of Illinois, 1998

[13] website: http://www.iter.org'

[14] Treuterer W., "Plasma Shape Control Design in ASDEX Upgrade", Proc. of 19^{th} Sypm. on Fusion Technol., Lisbon, 1996

[15] Levinton F.M., "Magnetic Field Pitch-Angle Measurements in the PBX-M Tokamak using the Motional Stark Effect", Phys. Rev. Lett., 2060-2063 **63**, 19, 1989.

[16] Wroblewski D., "Motional Stark Effect Polarimetry for a Current Profile Diagnostic in DIII-D" , Rev. Sci. Instrum., **61**, 3552, 1990

[17] website: http://www.aug.ipp.mpg.de

[18] Stark R., Sitzber. preuss.Akad. Wiss. Berlin, 932(1913), Ann. Physik **43**, 965 (1914)

[19] Mandl W., "Beam Emission Spectroscopy as a Comprehensive Plasma Diagnostic Tool", Plasma Phys. Control. Fusion **35** 1373-1394, 1993

[20] Pearson K. , "On Lines and Planes of Closest Fit to Systems of Points in Space", Phil. Mag. (6), **2**, 559-572, 1901

[21] Hotelling H., "Analysis of a Complex of Statistical Variables into Principal Components", Journal of Educational Psychology, **24**, 417-441, 489-520, 1933

[22] Mardia K.V., Kent J.T., Bibbly J.M., "Multivariate Analysis", Academic Press, London, 1979

[23] Draper N.R., Smith H., "Applied Linear Regression" second edition, Wiley, New York, 1981

[24] Kardaun O.J.W.F., "Basic Probability Theory and Statistics for Experimental Plasma Physics", IPP report 5/68, Garching, 1996

[25] Wind H., "Function Parameterization", Proceedings of the 1972 CERN Computing and Data Processing School, CERN 72-21, 1972

[26] Wind H., (a) "Principal Component Analysis and its Application to Track Finding", (b) "Interpolation and Function Representation", in " Formulae and Methods in Experimental Data Evaluation", Vol. 3, European Physical Society, Geneva, 1984

[27] McCarthy P.J., "The CLISTE Interpretive Equilibrium Code", IPP 5/85, Garching, 1999

[28] Foley M., "Disruption prediction on AUG using Functional parameterization", 4^{th} year project, Cork, 1999

[29] Belsley D.A., "Conditioning Diagnostics: Collinearity and Weak Data in Regression", Wiley, New York, 1991

[30] Hobrick J. , "Measurements of the Poloidal Magnetic and Radial Electric Field Profiles in ASDEX Upgrade and JET", , Proc. Advanced Diagnostic for Magnetic and Inertial Fusion, Kluwer Academic/Plenum Publishers, New York, 2001

[31] Jobson J.D., "Applied Multivariate Data Analysis. Volume I: Regression and Experimental Design", Springer, New York, 1991

[32] Bishop C.M.,"Neural Networks and their Applications" , Rev. Sci. Instrum., **65** 1803, 1994

[33] Private communication with Dr. Patrick McCarthy.

[34] Wolfram S., "Mathematica", Addison Wesley, Bonn, 1992

[35] Bessenrodt-Weberpals , "The multiple facets of ohmic confinemant in ASDEX", Nuclear Fusion, **31**, 155, 1991

[36] Yushmanov P.N. ,"Scalings for Tokamak Energy Confinement", , Nuclear Fusion, **30** 1999, 1990

[37] Wagner F ,"Regime of Improved Confinement and High Beta in Neutral Beam Heated Divertor Discharges of the ASDEX Tokamak", Phys. Rev. Lett. **49** 1408, 1982

[38] Biglari H., "Influence of Sheared Poloidal Rotation on Edge Turbulence", Phys. Fluids B **2** 1-4, 1990

[39] Taylor T.S., "Physics of Advanced Tokamaks" , Plasma Phys. Control. Fusion, **39** B47, 1997

[40] ITER Physics Expert Groups on Confinement and Transport and Confinement Modelling, Nuclear Fusion, **39**, 2175, 1999

[41] Peeters A.G. , "The Bootstrap Current and its Consequences" ,Plasma Phys. Control. Fusion, **42**, B231, 2000

[42] Private communication with Dr. Arthur Peeters.

[43] Peeters A.G. , "Internal Transport Barriers in ASDEX Upgrade", Proc. IAEA conf., Sorento, 2002

[44] Quigley E. , "Formation Criterion and Position of Internal Transport Barriers in ASDEX Upgrade", to be published

[45] Wolf R , "Internal Transport Barriers in Tokamak Physics", Plasma Phys. Control. Fusion **45** R1-R91, 2003

[46] Gruber O. , "Stationary H-mode Discharges with Internal Transport Barrier on ASDEX Upgrade", , Phys. rev. Lett., **83** 1787, 1999

[47] Hobirk J. , "Reaching High Poloidal Beta at the Greenwald Density with Internal Transport Barrier Close to Full Noninductive Current Drive" , Phys. Rev. Lett., **87** No.8 5002, 2001

[48] Peeters A.G. , "Confinement Physics of the Advanced Scenario with ELMy H-mode Edge in ASDEX Upgrade", Nuclear Fusion, **42** 1376-1382, 2002

[49] Sips A.C.C. , "Steady State Advanced Scenarios at ASDEX Upgrade", Plasma Phys. Control. Fusion, **44** B69-B83, 2002

[50] Guenter S. , "MHD Phenomena in Reversed Shear Discharges on ASDEX Upgrade", , Nuclear Fusion, **40** 1541, 2000

[51] Hawkes N.C. , "Observation of Zero Current Density in the Core of JET Discharges with Lower Hybrid Heating and Current Drive", Phys. Rev. Lett., **87** No.11, 2001

[52] Merkl,D., "Current Holes and other Structures in Motional Stark Effect Measurements", PhD thesis, TU Munich, IPP Report 1/332, Garching, 2004

[53] Private communication with Dr. Joerg Hobirk

[54] Lister J.B. , "Fast Non-Linear Extraction of Plasma Equilibrium Parameters using a Neural Network Mapping.", Nuclear Fusion, **31** 1291, 1991

[55] Bishop , Proc. 17^{th} Intern. Symp. on Fusion Technol., Rome, 1993

[56] Lagin , Proc. 17^{th} Intern. Symp. on Fusion Technol., Rome, 1993

[57] Coccorese C.,"Identification of Non-circular Plasma Equilibria using a Neural Network Approach", Nuclear Fusion, **34** 1349, 1994

[58] Yoshino R.,"Sensor Algorithm of the Plasma Vertical Position to avoid a Vertical Displacement Event during Plasma Current Quench on JT-60U", Fusion Technol. **30**, 237, 1996

[59] Albanese R. , "Identification of Plasma Equilibria in ITER from Magnetic Measurements via Functional Parameterization and Neural Networks", Fusion Technol., **30** 219, 1996

[60] Na Y-S , "Real-Time Extraction of Plasma Equilibrium Parameters in KSTAR Tokamak using Statistical Methods", Review of scientific instruments, **72** 2, 1400-1405, 2001

[61] Sengupta A.,"Modified Neural Networks for Rapid Recovery of Tokamak Plasma Parameters for Real-Time Control" , Rev. Sci. Instrum., **73** 2566, 2002

[62] Dendy R., "Magnetohydrodynamics" lecture notes by Hopcraft K.I., in "Plasma Physics, an introductory course", Cambridge University Press, Cambridge, 1993

[63] Foley M. , "Expansion of ASDEX Upgrade's Real-Time Parameter Recovery Routine to Include Additional Moments in the Current Profile", Proc. 28^{th} Eur. Comf. on Contr. Fusion Plas. 25A, 357, Funchal, 2001

[64] McCarthy P.J., Foley M. , "Fast Recovery of the q-Profile on ASDEX Upgrade Using a Nonlinearly Optimised Function Parameterization Model" , Proc. 29^{th} Eur. Comf. on Contr. Fusion Plas., Lousanne, 2002